Mass - Resolved Resonant Two - Photon Ionisation Spectroscopy of Jet - Cooled Cu_2 and Ag_2

by

Andrew Michael Butler

A thesis presented for the degree of
Doctor of Philosophy in the
Faculty of Science at the
University of Edinburgh
1989

To Mum and Dad.

Abstract

Clusters of the transition metals were generated by laser vaporisation of a sample of the metal into the throat of a pulsed supersonic expansion. This allowed clusters with internal temperatures as low as 5 K to be routinely prepared. Mass-selective detection was accomplished by multi-photon ionisation of the clusters within the ion source of a time - of - flight mass spectrometer. Use of a tunable laser to carry out electronic excitation, prior to ionisation, allowed mass - resolved resonant two - photon ionisation spectra of the clusters to be recorded.

Real time control of the experiment and automated data logging was achieved using software developed to run on an IBM PC - AT microcomputer. This allowed multiple ion signals to be recorded simultaneously whilst carrying out R2PI or time-resolved studies on the metal cluster species in the beam.

Resonant two - photon ionisation spectroscopic studies were carried out on the (0 - 0) and (1 - 0) bands of the J ← X system of Cu_2 and the A ← X system of Ag_2. The 0.04 cm^{-1} bandwidth of the tunable dye laser used allowed rotationally resolved spectra to be recorded. The spectra recorded for these systems showed them both to be $\Delta\Lambda = 0$ (or $\Delta\Omega = 0$) transitions.

The J state of Cu_2 was assigned to the $^1\Sigma_u^+$ state derived from the $^2P + {}^2S$ atomic limit at $D_e(X) + 45821$ cm^{-1}. Rotational analysis of the spectra yielded the following constants for the $^{63}Cu_2$ isotopomer: $B_e' = 0.1166(1)$ cm^{-1}, $\alpha_e' = 0.0021(1)$ cm^{-1}. This gave $R_e = 2.138(1)$ Å for the J state, shorter than the ground state bond length. Accordingly the transition was assigned to $3d\pi_g \rightarrow$

$4p\pi_u$, to give the above assignment.

The rotational constants obtained, for the $^{107}Ag_2$ isotopomer, from analysis of the spectra of the A ← X system of Ag_2 were: $B_e' = 0.0447(3)$ cm^{-1}, $\alpha_e' = 0.0004(2)$ cm^{-1}, and $B_0'' = 0.0490(18)$ cm^{-1}. These gave bond lengths of $R_e' = 2.649(9)$ Å and $R_0'' = 2.530(46)$ Å. The observed $\Delta\Omega = 0$ transition agreed with the previous assignment of the A state as 0_u^+ arising from the $5s\sigma_g \rightarrow 5s\sigma_u$ promotion.

Acknowledgements

Firstly my thanks must go to my supervisor Dr. Patrick Langridge-Smith for initiating my interest in this field, and for his continuing support and advice during the course of the project.

Many thanks must also go to my collaborators during this work, Mr. Peter Cartwright and Mr. Andrew James with whom the equipment described in chapter 2 was designed and constructed. Their assistance during the experimental work is also gratefully acknowledged. I am indebted to Dr. Kenneth Lawley for many helpful discussions on the interpretation of the results.

Inaddition my thanks go to the staff of the mechanical and electronics workshops of the Department of Chemistry, and Dr. Christopher Adie of the Edinburgh University Computing Service for their assistance and advice at various times throughout the project.

This thesis was produced using the SCRIBE text processor for which I must thank Mr. Roger Hare for allowing access to his database.

I am grateful to the Science and Engineering Research Council for the award of a postgraduate studentship and latterly the University of Edinburgh for a demonstratorship.

Declaration

This thesis was composed by myself and is based on work carried out whilst a member of the laser chemistry group at Edinburgh University.

Signed

Date 14/9/89

Table of Contents

List of Figures

List of Tables

List of Code Examples

Chapter 1
Introduction

Small clusters of the transition metals play a pivotal rôle in many important processes. Their involvement in areas such as nucleation [1], the photographic process [2] - [4], catalysis [5] [6], and indications of their presence in some enzymes [7] has provoked much discussion recently [8] - [13]. The clusters fall in the intermediate region between a single atom and the bulk metal and can be regarded as discrete molecules, microscopic samples of the bulk, or as an entirely separate class of entities. It should be pointed out that the term *cluster* is used in this thesis to describe an aggregate composed solely of metal atoms and not the conventional inorganic metal cluster with ligands attached. Until recently data on these systems has been very scarce. In the past decade however, a sizeable database of information on the clusters has been accumulated. Information gained so far includes:- ionisation potentials, electron affinities, geometrical structures, and, more recently, the change in electronic structure from the discrete levels of a molecule to the band structure of the bulk metal, probed via photoelectron spectroscopy. For the dimers a substantial quantity of spectroscopic data has also been amassed.

The bonding in transition metal clusters is of great interest as it is expected to differ markedly from clusters of the main group elements due to the presence of the d electrons. The d orbitals are heavily contracted with respect to the s orbitals and will therefore be expected to interact only at short internuclear distances [14]. Thus two levels of bonding are expected; '$ns\sigma$' bonding at large internuclear distances and '$(n-1)d\sigma/\pi/\delta$' at shorter internuclear separation. The

group 1B metals occupy a unique position in that the d shell of the atoms is full, and will therefore combine to give an essentially non - bonding set of molecular orbitals in the ground electronic state. These orbitals can therefore be ignored to a first approximation when attempting to calculate molecular constants. For this reason they have been popular systems for theoretical modelling, being regarded as *pseudo* alkali metals, with a single electron in the s - orbital [15]. Correct modelling of clusters of the group 1B metals is seen as a prerequisite to construction of valid models for the rest of the transition series.

Until recently most experimental studies of transition metal 'clusters' have been carried out on inorganic clusters with attached ligands, whereas theoretical calculations have been applied to ligand free clusters. The reason for this anomaly is that historically much of the information on structure and bonding in molecules has been obtained from analysis of the spectra of gas phase samples. The refractory nature of the transition metals has until recently made it difficult, if not impossible, to obtain a high enough concentration of these species in the gas phase to enable conventional spectroscopic techniques (e.g. LIF) to be employed. Conventional sources for species with a low vapour pressure, such as heated ovens [13] [17] and electric discharges [18] have proved only marginally successful when applied to the transition metals. One of the main problems has been due to the high temperatures required to produce an appreciable vapour pressure, giving rise to a large number of thermally populated quantum states. The large number of lines this leads to causes severe congestion in the observed spectra, which can prevent any reliable assignment of the recorded features [13] [16].

An alternative approach has been to trap the metal clusters in cryogenic rare gas matrices to reduce the number of thermally populated quantum states [19]. This is done by co - condensation of the metal vapour with an inert gas such as neon. Clusters can be generated by condensation before becoming frozen into the matrix, or from atoms and smaller clusters trapped in the matrix, by heating or irradiation with the output of a laser [20]. The main drawback of this technique has been interaction between the clusters and the host matrix. These interactions can shift and otherwise perturb the spectrum of a cluster [21] [22], and in some cases invert the order of closely spaced electronic states [23].

The main problem inherent in all the foregoing techniques is the lack of mass selectivity. This is an important consideration when attempting to carry out spectroscopic studies on any species containing transition metal atoms, many of which have significant natural abundances of a number of different isotopes. This gives rise to different isotopic mixtures (isotopomers) of the same cluster size, in addition to the distribution of cluster sizes. The different isotopomers of the same cluster size have qualitatively similar spectra which frequently overlap. Conventional spectroscopic methods are intrinsically non mass - selective, the recorded spectra being the result of overlaying the spectra derived from the different isotopomers. This causes congestion in the spectra, with either lines from all the isotopomers present, or broad lines resulting from blending of lines from the different isotopomers. This congestion is in addition to that caused by the coincidence of spectra arising from different sizes of clusters. The only way to obtain single isotope spectra with conventional spectroscopic methods is to use isotopically enriched samples of the element in question. This does not,

however, remove the problem of the distribution of cluster sizes formed.

These problems have led to the development over the last few years of a powerful new technique for the production of cold, gaseous metal clusters, coupled with mass-selective detection [24]. The technique utilises a pulsed supersonic molecular beam [25] into which metal atoms are seeded by laser vaporisation of a metal target in the throat of the supersonic expansion. Clusters are formed by condensation of these atoms in the supersonic nozzle source, before expansion to form the molecular beam. The high degree of cooling achieved during the supersonic expansion, and the near collisionless environment of the molecular beam provides an almost ideal sample of metal clusters for spectroscopic analysis. Although supersonic expansions do not cool all degrees of freedom equally, rotational and translational temperatures as low as 5 K can routinely be achieved, with vibrational temperatures somewhat higher. The higher vibrational temperature is due to the lower cross - section for vibrational → translational energy transfer in the two - body collisions which cause the cooling during the supersonic expansion to form a free jet [25]. The reduction in the number of quantum states populated as a result of this jet - cooling gives fewer lines in the spectrum. Coupled to this is an increase in intensity of the lines that are present, due to the increased Boltzmann population of those levels that are occupied. These two factors combine to give spectra which are markedly easier to assign than those obtained using conventional sources.

Continuous supersonic beams have been used previously, with oven sources, for studying group 1A metal clusters [26]. Extension of this technique to studies of the transition metals has been hindered due to the high temperatures required.

Problems have been encountered with contamination from the surfaces of the source, and clogging of the nozzle. The use of a laser to accomplish vaporisation results in only very localised heating of the target, with the rest of the apparatus remaining at ambient temperature. Vaporisation of the metal directly into the gas flow through the supersonic nozzle also generates a high concentration of the metal in the beam.

Mass-selective detection is achieved using a time of flight mass spectrometer (TOFMS) to analyse ions generated using multi-photon ionisation (MPI). Photoionisation of the clusters in the molecular beam is carried out by crossing the beam with the output of one or two lasers, as it passes through the ion source region of a TOFMS. Resonant two - photon ionisation can be accomplished using a tunable laser to carry out the initial promotion of the clusters to an excited electronic state. Ionisation out of this excited state is then achieved by absorption of a second photon of either the same or a different wavelength, depending on the magnitude of the ionisation potential. This allows the spectroscopy of the intermediate electronic states to be studied. The mass-selective detection provided by the TOFMS enables the spectra due to the different isotopomers to be recorded separately.

Spectroscopic studies of a number of the transition metal dimers, e.g. V_2 [27], Mo_2 [28], Cu_2 [29] [30], Cr_2 [31] [32], Ni_2 [33], and Ag_2 [34], as well as Cu_3 [35], have been carried out recently using this approach. These studies have provided information on the ground and excited electronic states of these molecules in the gas phase. They have provided clarification and allowed extension of previous studies carried out using conventional methods. Notably, the previous

determination of the ground state bond length in Cr_2^- was confirmed [36]. The bond length of 1.68 Å is much shorter than the nearest neighbour distance of 2.5 Å in the bulk metal. This observation is the most dramatic demonstration to date of the effect that partially filled d - orbitals can have on bonding. Subsequent to this many theoretical and almost all the spectroscopic studies of the transition metal dimers have been aimed at defining the rôle played by the d - electrons in the bonding of these species. Laser-induced fluorescence (LIF) has also been used to study clusters generated with the laser vaporisation / supersonic expansion source [37] [38]. Though not having the advantage of mass selectivity these experiments have nonetheless provided a wealth of information. In particular the information obtained pertaining to the ground electronic states, via dispersed emission studies, has been especially useful as so little is available from R2PI studies due to the low number of ground state levels populated.

Despite the recent advances made possible using this type of cluster source, there are still a significant number of gaps left in our experimental knowledge of the dimers. The dimers of the group 1B metals are amongst the most important, being the testbed for many theoretical models of the transition metals, due to their relatively simple electronic structure. Thus experimental evidence on the electronic structure of the dimers of copper and silver is of great value. This is especially true of silver dimer for which none of the previously observed electronic band systems have been rotationally resolved. As a result there has been no previous direct experimental determination of the bond lengths or electronic state symmetries for the ground or excited electronic states of this molecule.

In addition to spectroscopic studies the laser vaporisation / supersonic expansion cluster source has previously been used for generating clusters to allow measurement of the cluster ionisation potentials [39] [40] and electron affinities [41] [42], as a function of cluster size for a number of metals. Adaptation of the cluster source, by the addition of secondary injector nozzles for introducing other reagents to the gas flow, has enabled some workers to carry out investigations into the reactivity of the naked clusters [43] - [45]. This field will doubtless become of great importance as these studies are extended to commercially important reactions.

The aim of the work described in this thesis was twofold. Firstly, the construction of a suitable molecular beam / time-of-flight mass spectrometer apparatus, and development of the requisite instrumentation. The second aim was to carry out high resolution spectroscopic studies of the dimers of the group 1B metals copper and silver.

Chapter 2 describes the molecular beam apparatus, cluster source, time - of - flight mass spectrometer, and the experimental techniques employed. A major part of the experimental system was the hardware and software used for control, data acquisition, and processing. How this was accomplished is described in chapter 3. The remaining chapters (4 - 6) describe the experimental investigations undertaken and results obtained. Chapter 4 describes observations of mass spectra of transition metal clusters obtained using non - resonant photoionisation. The final two chapters describe resonant two - photon ionisation spectroscopic studies carried out on Cu_2 and Ag_2. High resolution, rotationally resolved, spectra of electronic band systems of both these molecules

were recorded and analysed to obtain the relevant rotational constants, electronic state symmetries, and bond lengths.

References

[1] Wegener P.P., Wu B.J.C., Adv. in Colloid and Interface Science, **7**, p 325, (1977)

[2] Basch H., Faraday Symp., **14**, p 149, (1980)

[3] Baetzold R.C., Mack R.E., J. Chem. Phys., **62**, p 1513, (1975)

[4] Hamilton J.F., J. Vac. Sci. Technol., **13**, p 319, (1976)

[5] Anderson J.F., *Structure of Metallic Catalysts*, Academic Press, London, 1975.

[6] Gole J.L., *Metal Clusters, ed. Moskovits M.*, Wiley Interscience, Toronto, 1985.

[7] Lovenberg W., *Iron - Sulphur Proteins*, Academic Press, New York, 1973.

[8] Faraday Symposia of the Chemical Society, *Diatomic Metals and Metal Clusters*, **14** 1980

[9] McAdon M.H., Goddard W.A., J.Phys.Chem., 91, p2607,(1987)

[10] Ozin G.A., Mitchell S.A., Angew. Chem., **22**, p 674, (1983)

[11] Weltner W., van Zee R.J., Ann. Rev. Phys. Chem., **35**, p 291, (1984)

[12] Moskovits M., *Metal Clusters*, Wiley - Interscience, Toronto, 1985.

[13] Morse M.D., Chem. Rev., **86**, p 1053, (1986)

[14] Walch S.P., Bauschlicher C.W., *Comparison of ab initio Quantum Chemistry with experiment for Small Molecules, ed. Bartlett R.J.*, D. Reidel Publishing Co., Holland (Dordrecht), 1985.

[15] Kontecky J., Kantucci P., Chem. Rev., **86**, p 539, (1986)

[16] Sradnov V.I., Pesic D.S., J. Mol. Spec., **90**, p 27, (1981)

[17] Aslund N., Barrow R.F., Richards W.G., Travis D.N., Ark. Fys., **30**, p 171, (1965)

[18] Shin-Piaw C., Loong-Seng W., Yoke-Seng L., Nature, **209**, p 1300, (1966)

[19] Ozin G.A., Huber H., McIntosh D., Mitchell S., Norman J.G., Noodlemann L., J. Am. Chem. Soc., **101**, p 3504, (1979)

[20] Ozin G.A., Faraday Symp., **14**, p 7, (1980)

[21] Mitchell S.A., Kenny - Wallace G.A., Ozin G.A., J. Am. Chem. Soc., **103**, p 6030, (1981)

[22] Mitchell S.A., Ozin G.A., J. Phys. Chem., **88**, p 1425, (1984)

[23] Walch S.P., Bauschlicher C.W., Langhoff S.R., J. Chem. Phys., **85**, p 5900, (1986)

[24] Dietz T.G., Duncan M.A., Powers D.E., Smalley R.E., J. Chem. Phys., **74**, p 6511, (1981)

[25] Smalley R.E., Wharton L., Levy D.H., Acc. Chem. Res., **10**, p 139, (1977)

[26] Schumacher E., Gerber W.H., Harri H.P., Hoffmann M., Scholl E., A.C.S. Symp., **197**, p 83, (1982)

[27] Langridge-Smith P.R.R., Morse M.D., Hansen G.P. Smalley R.E., J. Chem. Phys., **80**, p 593, (1984)

[28] Hopkins J.B., Langridge-Smith P.R.R., Morse M.D., Smalley R.E., J. Chem. Phys., **78**, p 1627, (1983)

[29] Powers D.E., Hansen S.G., Geusic M.E., Pulu A.C., Hopkins J.B., Dietz T.G., Duncan M.A., Langridge-Smith P.R.R., Smalley R.E., J. Phys. Chem., **86**, p 2556, (1982)

[30] Powers D.E., Hansen S.G., Geusic M.E., Michalopoulos D.L., Smalley R.E., J. Chem. Phys., **78**, p 2866, (1983)

[31] Michalopoulos D.L., Geusic M.E., Hansen S.G., Powers D.E., Smalley R.E., J. Phys. Chem., **86**, p 3914, (1982)
[32] Riley S.J., Parks E.K., Pobo L.G., Wexler S., J. Chem. Phys., **79**, p 2577, (1983)
[33] Morse M.D., Hansen G.P., Langridge-Smith P.R.R., Zheng L.S., Geusic M.E., Michalopoulos D.L., Smalley R.E., J. Chem. Phys., **80**, p 5400, (1984)
[34] Hopkins J.B., Langridge-Smith P.R.R., Morse M.D., Smalley R.E., *unpublished results*,
[35] Morse M.D., Hopkins J.B., Langridge-Smith P.R.R., Smalley R.E., J. Chem. Phys., **79**, p 5316, (1983)
[36] Efremov Y., Samoilova A.N., Gurrich L., Opt. Spect., **36**, p 381, (1974)
[37] Rohlfing E.A., Valentini J.J., J. Chem. Phys., **84**, p 6560, (1986)
[38] Bondybey V.E., Schwartz G.P., English J.H., J. Chem. Phys., **78**, p 11, (1983)
[39] Rohlfing E.A., Cox D.M., Kaldor A., Johnson K.H., J. Chem. Phys., **81**, p 3864, (1984)
[40] Rohlfing E.A., Cox D.M., Kaldor A., J. Phys. Chem., **88**, p 4497, (1984)
[41] Zheng L.S., Brucat P.J., Pettiette C.L., Yang S.H., Smalley R.E., J. Chem. Phys., **83**, p 4273, (1985)
[42] Zheng L.S., Kraner C.M., Brucat P.J., Yang S.H., Pettiette C.L., Craycraft M.J., Smalley R.E., J. Chem. Phys., **85**, p 1681, (1985)
[43] St. Pierre R.J., Chronister E.L., El-Sayed M.A., J. Phys. Chem., **91**, p 5228, (1987)
[44] Zakin M.R., Cox D.M., Kaldor A., J. Phys. Chem., **91**, p 5224, (1987)
[45] Zakin M.R., Cox D.M., Kaldor A., J. Chem. Phys., **87**, p 5046, (1987)

Chapter 2
Experimental Techniques and Apparatus used in the Investigation of Transition Metal Clusters

2.1 Introduction

Central to the investigation of naked transition metal clusters was the construction of a suitable apparatus for generating and detecting them. The technique employed was the pulsed supersonic beam and time-of-flight mass spectrometer (TOFMS) apparatus introduced in the previous chapter. The metal clusters were created by laser vaporisation of a sample of the metal into the helium flow through a supersonic nozzle. Electronic excitation and subsequent photoionisation of the clusters was achieved using multi-photon ionisation with mass-resolved detection provided by the TOFMS. The entire experiment was controlled from an IBM Personal Computer - AT through an integrated system of computer controlled instruments.

This chapter describes the experimental techniques and equipment used to carry out the work presented in this thesis. The following chapter describes the data system which was developed to integrate the control and data acquisition.

2.2 The vacuum system

The vacuum system consisted of 3 differentially pumped chambers (figure 2.1) capable of being isolated from each other and the pumps by pneumatically operated gate valves.

Figure 2.1
Schematic of the experimental apparatus

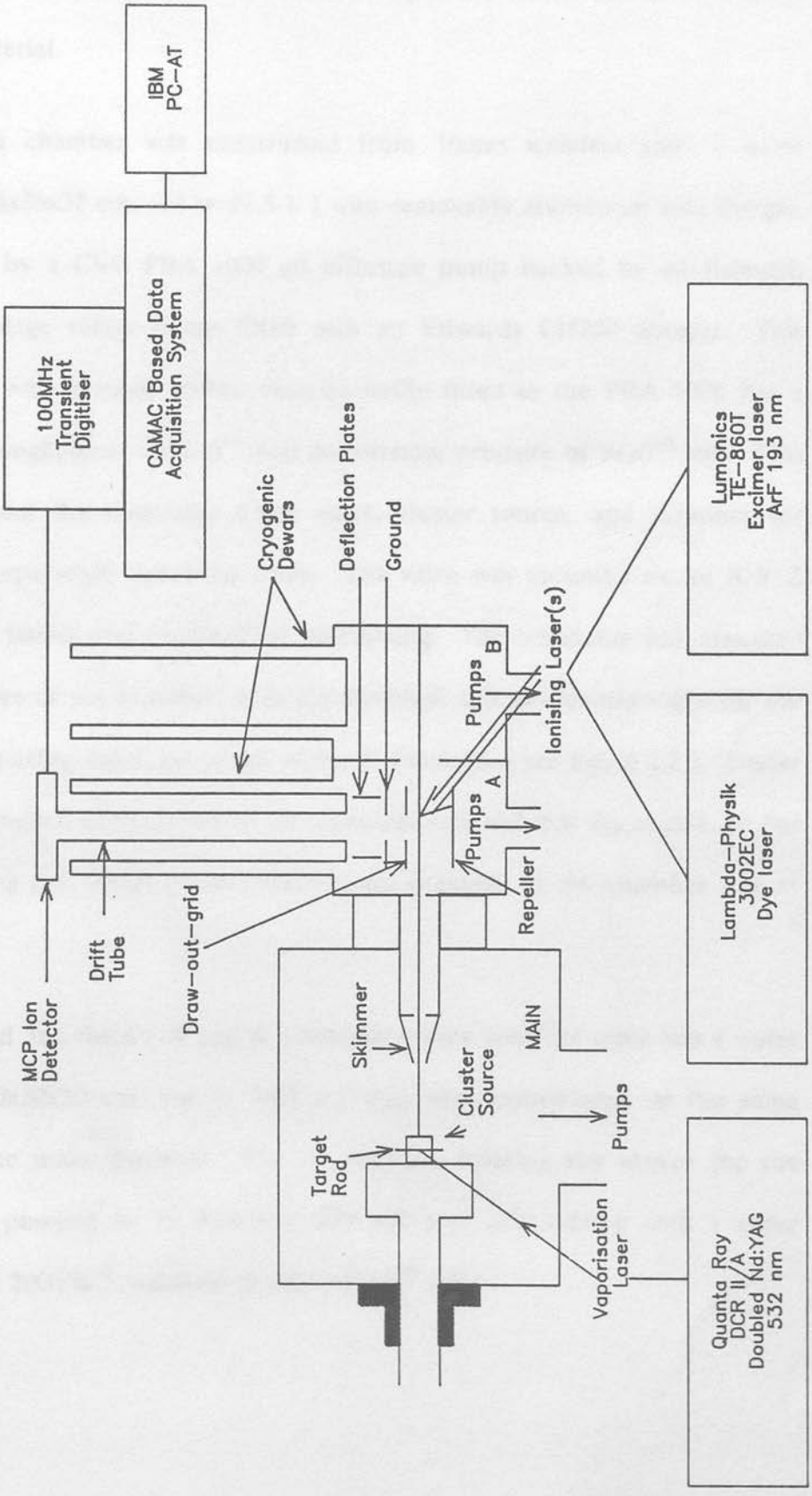

The use of a differentially pumped system as opposed to one large chamber reduced the pumping capacity required of the individual pumps over that needed for a single chamber [1]. The main chamber could be be isolated from the rest of the system and the pumps to allow access to adjust the cluster source, or change the target material.

The main chamber was constructed from 16mm stainless steel (outer dimensions 36x36x32 cm, vol = 61.5 l.) with removable aluminium side flanges, and pumped by a CVC PBA 1000 oil diffusion pump backed by an Edwards E2M40 two stage rotary pump fitted with an Edwards EH250 booster. This combination, with a water cooled chevron baffle fitted to the PBA 1000 has a maximum throughput of 2650 ls^{-1} and an ultimate pressure of $8x10^{-6}$ mb. This chamber housed the molecular beam valve, cluster source, and skimmer for forming the supersonic molecular beam. The valve was mounted on an X-Y-Z translator for lateral and longitudinal positioning. The translator was mounted on the rear face of the chamber, with the electrical and gas feedthroughs for the beam valve entering down the centre of the Z translator (see figure 2.2). Under typical experimental conditions (10 Hz repetition rate, 0.5 mm dia nozzle, 10 bar helium backing gas, 900µs pulse) the average pressure in the chamber was ~ $3x10^{-4}$ mb.

The second and third (A and B) chambers were both the same size (outer dimensions 30x30x30 cm, vol = 19.2 l) and were constructed of the same material as the main chamber. The A chamber, housing the source for the TOFMS, was pumped by an Edwards E09 diffusion pump fitted with a water cooled baffle (2000 ls^{-1}, ultimate pressure $5x10^{-8}$ mb).

Figure 2.2
Detail of the cluster source and nozzle translator

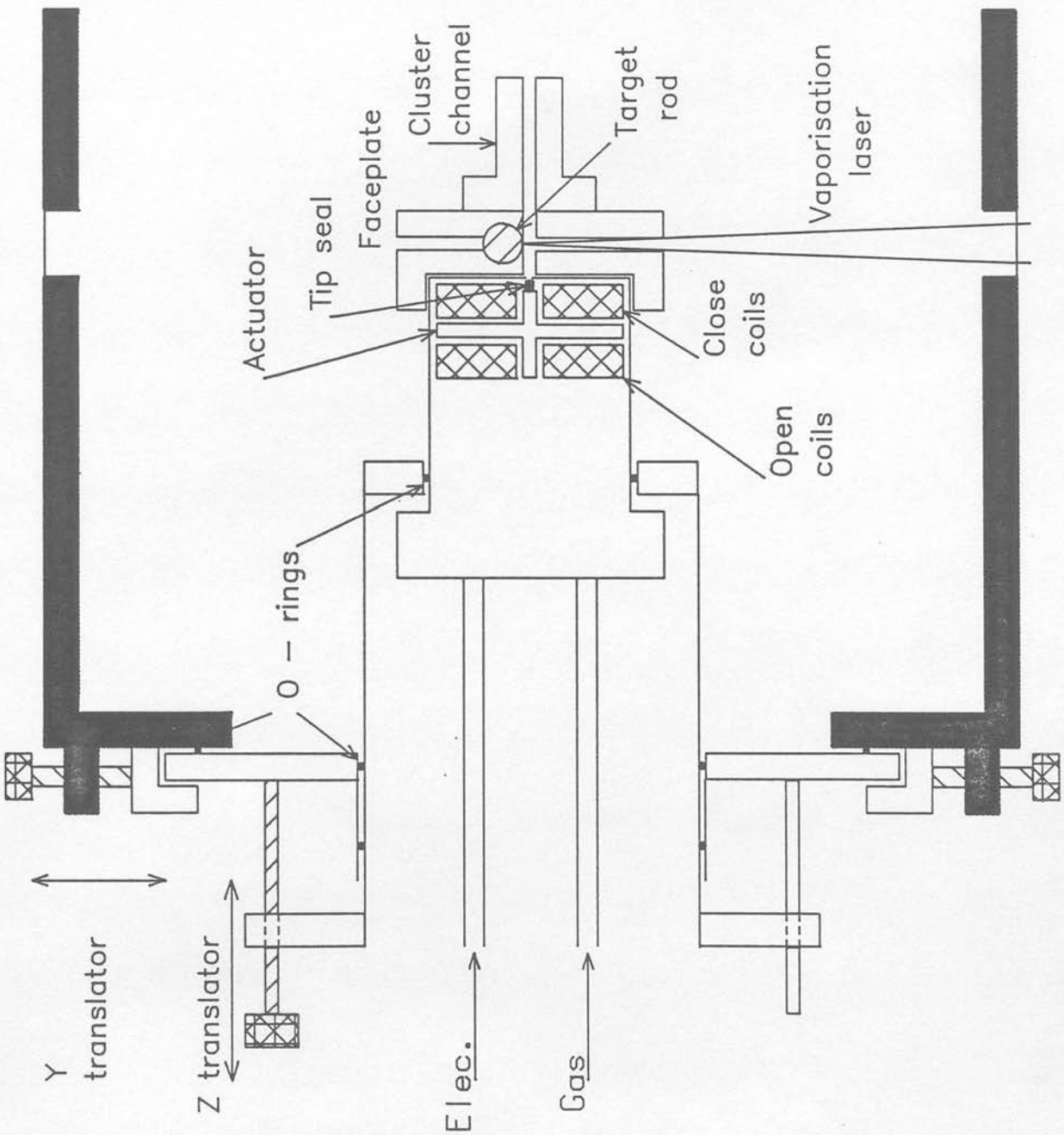

Windows for the admittance of the laser beams and electrical feedthroughs for the TOFMS were mounted on the side flanges.

The B chamber, which acted as a dump region for the molecular beam, was pumped by an Edwards 160/700 Diffstak (1300 ls^{-1}, ultimate pressure $3x10^{-8}$ mb). The diffusion pumps for the A and B chambers were backed by a pair of Edwards E2M8 rotary pumps working in parallel. Both the A and B chambers had double skinned stainless steel dewars attached to the top flange. The dewar on the A chamber surrounded the flight tube of the time of flight mass spectrometer. The dewars were filled with liquid nitrogen during experiments to cryopump the A and B chambers. Under the operating conditions above the pressure in the A chamber was typically $\sim 10^{-7}$ mbar.

The pressure in the vacuum system was monitored via a system of Pirani (Balzers TPR 010 and Edwards PRL 10K), Penning (Edwards CP 25K), and cold cathode (Balzers IKR 020) gauges connected to digital (Balzers PKG 100 and Edwards 1105) and analogue (Edwards Penning 1005) controllers.

2.3 Cold cluster generation

Metal clusters were generated by condensation of a plasma produced by focusing the Q - switched output of a Nd:YAG laser onto a metal target rod located in the throat of the pulsed supersonic nozzle (see section 2.5.2). The clusters were entrained in the flow of helium through the nozzle, which expanded into the main chamber to form a free jet before being skimmed (Beam Dynamics, 3 mm diameter, 50° included angle) to give a supersonic beam. This

beam carried the clusters through the ionisation region of the TOFMS where they were probed using MPI techniques (see section 2.6). The location of the cluster source in the apparatus is shown in figure 2.1 and the detail is shown in figure 2.2. A stepper motor (not shown) mounted on the top flange of the main chamber was connected via universal coupling joints through an O - ring seal to the target rod. This allowed the rod to be rotated and translated in the cluster source to ensure even removal of material.

The molecular beam valve used in the present work was a Newport Research Corporation BV 100 controlled by a BV 100-D driver unit, and synchronised to the rest of the experiment by a trigger pulse from a computer controlled delay generator. This valve was of the double solenoid type described by Grant et. al. [8]. The valve was typically operated with a 900 μs pulse width and 10 atm of helium backing gas. The temporal profile of the gas pulse from the valve (figure 2.3) was recorded by monitoring the helium ion intensity in the time of arrival signal from the TOFMS whilst scanning the delay between the trigger pulses for the valve and the ArF excimer laser employed to perform the ionisation. The profile shown in figure 2.3 is the result of summing 10 experimental shots at each delay time, the method by which this was accomplished is described in section 3.2.5. The diameter of the valve orifice was 500 μm which gave a throughput of 16.9 τls^{-1} at the 10 Hz repetition rate used, assuming the helium left the valve at the speed of sound (1250 ms^{-1} at 298 K) [4].

The cluster source, shown in figure 2.2, consisted of an aluminium faceplate bolted over the end of the valve. This was drilled through with three mutually perpendicular channels.

Figure 2.3
Temporal profile of the gas pulse obtained from the molecular beam valve

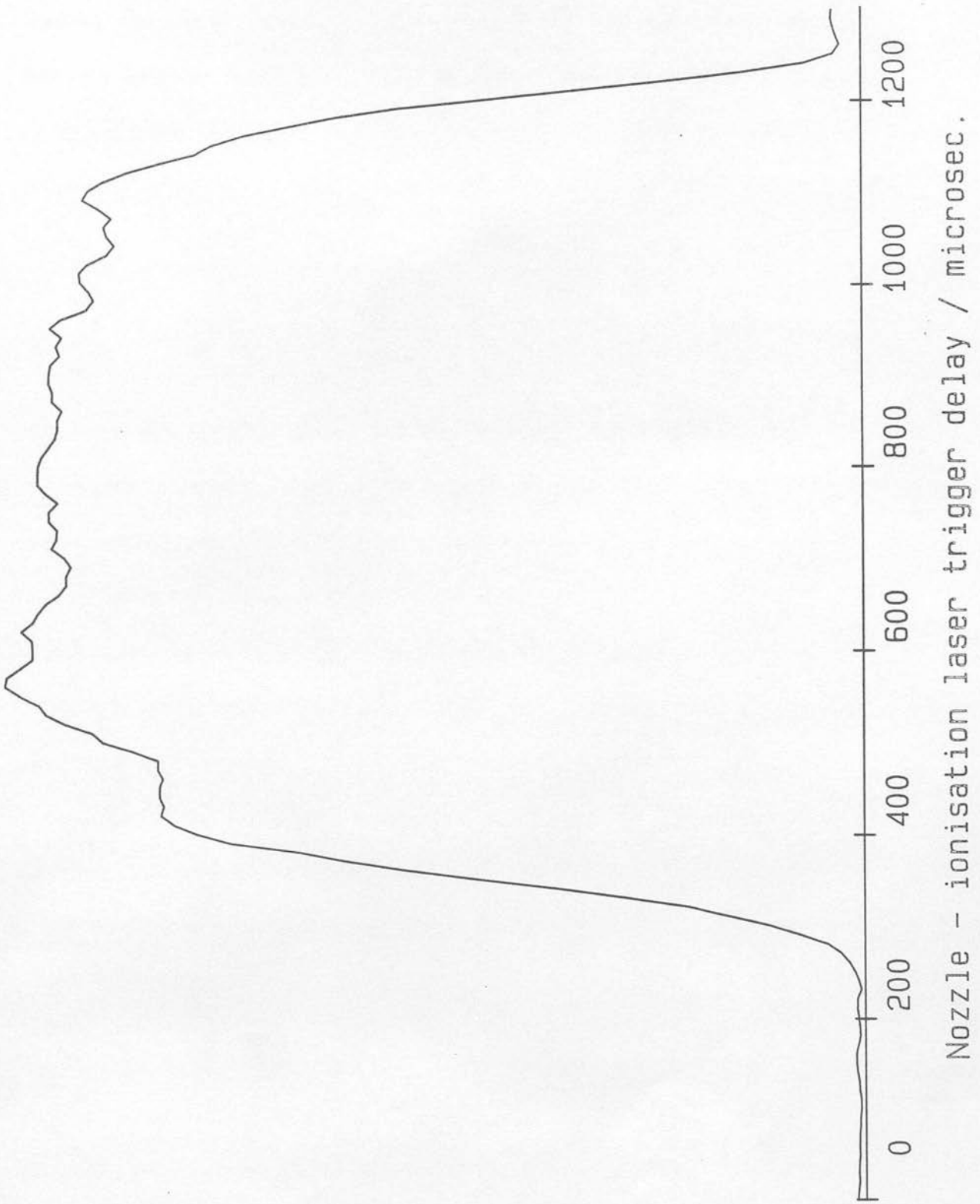

A 1.5 mm cluster channel ran coaxial to the valve to contain and direct the helium flow and act as the nozzle for the formation of a free jet. This was crossed 7 mm downstream of the valve by two other channels, one 3 mm in diameter running horizontally for introduction of the vaporisation laser, the other 5 mm in diameter, running vertically and offset so as to tangentially intersect the cluster channel. A 5 mm diameter rod of the metal under investigation was inserted into this channel. By offsetting the metal rod in this manner the flow of helium was not disturbed and the vaporised metal was introduced directly into the helium flow.

The vaporisation laser created a plasma from the surface of the metal rod, which expanded into the cluster channel. Entrainment and subsequent collisions in the flow of helium quenched the plasma after which the atoms underwent condensation to form the clusters. The condensation is believed to occur by 3 - body collisions between two metallic species and a helium atom [4]. The excess energy of condensation being removed as translational energy in the helium and lost in collisions with the other species in the beam. The efficiency of clustering depended on the metal, with some requiring an extension to be fitted to the cluster channel to allow more time for clustering (see chapter 4). The backing gas pressure also affected the cluster distribution, as expected, with lower pressures resulting in fewer high numbered clusters being formed due to the lower collision rate.

The cluster source was aligned with the skimmer and the ion source of the TOFMS by monitoring the helium ion signal obtained by multi-photon ionisation of the beam with the output of an ArF excimer laser (see section 2.5.3).

Figure 2.4
Gas pulse profile showing drop in helium ion intensity caused by vaporisation of metal into the gas flow

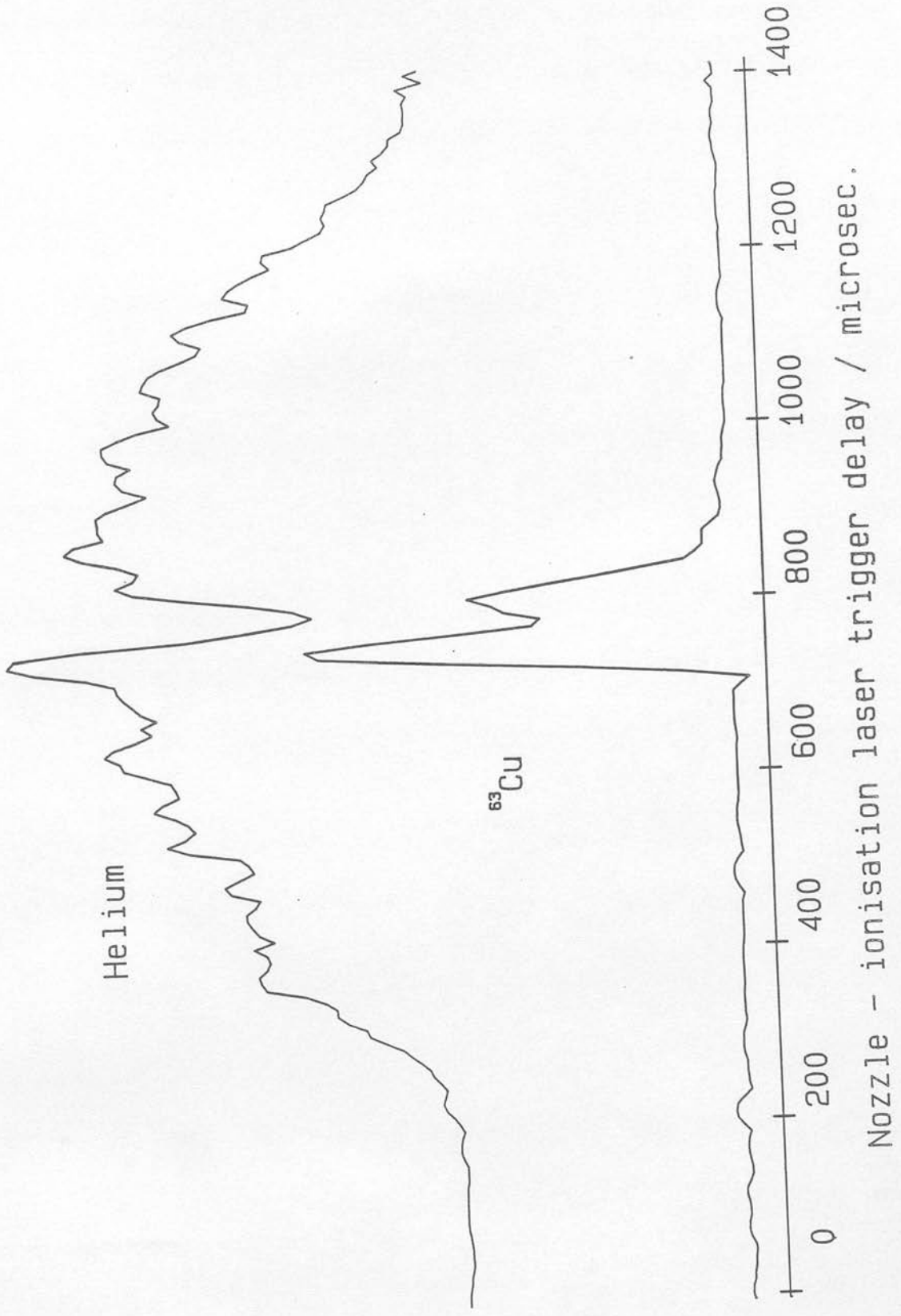

The vaporisation was timed to occur at the peak of the helium pulse so as to fully entrain the metal plasma. The time of arrival of the vaporisation laser pulse was ascertained by mapping out the temporal profile of the helium pulse as above. The profiles obtained without the vaporisation laser and when it was operating are shown in figures 2.3 and 2.4. The latter figure shows a clear dip in the intensity of the helium ion signal coinciding with the copper atom ion signal. This shows that some of the helium in the beam was displaced by the metal plasma. The dip in the helium ion intensity was used to set the delay of the vaporisation laser during the setup procedure before metal clusters were observed in the mass spectrum.

2.3.1 Supersonic beams

The expansion out of the cluster channel into the main chamber formed the flow of helium and the entrained metal clusters into a free jet. The collisions occurring as the beam exited the channel converted the random translational motion and some of the internal vibrational and rotational motion of the clusters, via 2 - body collisions, into directed mass flow along the axis of the nozzle. This increased the velocity of the beam on axis whilst lowering the internal temperature and freezing the cluster distribution. The shock wave formed by the expanding gas has been shown by Campargue [9] to push the residual background gas out of the path of the expansion. This allowed high background pressures to be tolerated in the main chamber and thus lessen the pumping capacity required. The free jet passed through a skimmer mounted on the inner wall of the main chamber opposite the cluster source, to form a supersonic beam

[2] - [7]. The skimmer was stood off the wall to reduce the interference caused to the beam by material from the beam being backscattered off the wall.

The end result of the expansion, after skimming was a beam of gaseous clusters with a very low internal temperature. The final translational temperature reached during the expansion was estimated from the rotational temperature of the R2PI spectra recorded for the dimers entrained in the beam ($T_{TR} \simeq T_{ROT}$ [19]). With the conditions in use (10 atm. He, 0.5 mm valve orifice) the rotational temperature in the beam was typically ~ 5 K (see chapters 5 and 6). The final speed of the beam was found from the distance between the nozzle and the ion source of the TOFMS (51 cm), and the time delay between firing the lasers used for vaporisation and ionisation (~ 300 μs). These figures gave a velocity of ~ 1700 ms^{-1} along the axis of the beam. The narrowing of the translational velocity spread is simulated in figure 2.5 where the Maxwellian distributions for helium at 300 K and 5 K are shown. The distribution for 5 K has been shifted to give an average speed of 1700 ms^{-1}. The figure shows the magnitude of the increase in the average molecular velocity in the beam over a static room temperature sample as well as the reduction in velocity spread.

The reduction in the spread of translational velocity gave a corresponding reduction in the Doppler width of the observed spectroscopic transitions [24]. Another advantage of cooling the clusters was that only the lowest few vibrational and rotational levels were populated. With so few levels populated the number of observable transitions was reduced giving much less congested spectra. The consequent increase in the Boltzmann population of the lowest states meant that there were more clusters in these levels which could be excited.

Figure 2.5
Maxwellian velocity distributions for helium at 5 K and 300 K
(5 K distribution maximum shifted to average speed of molecular beam)

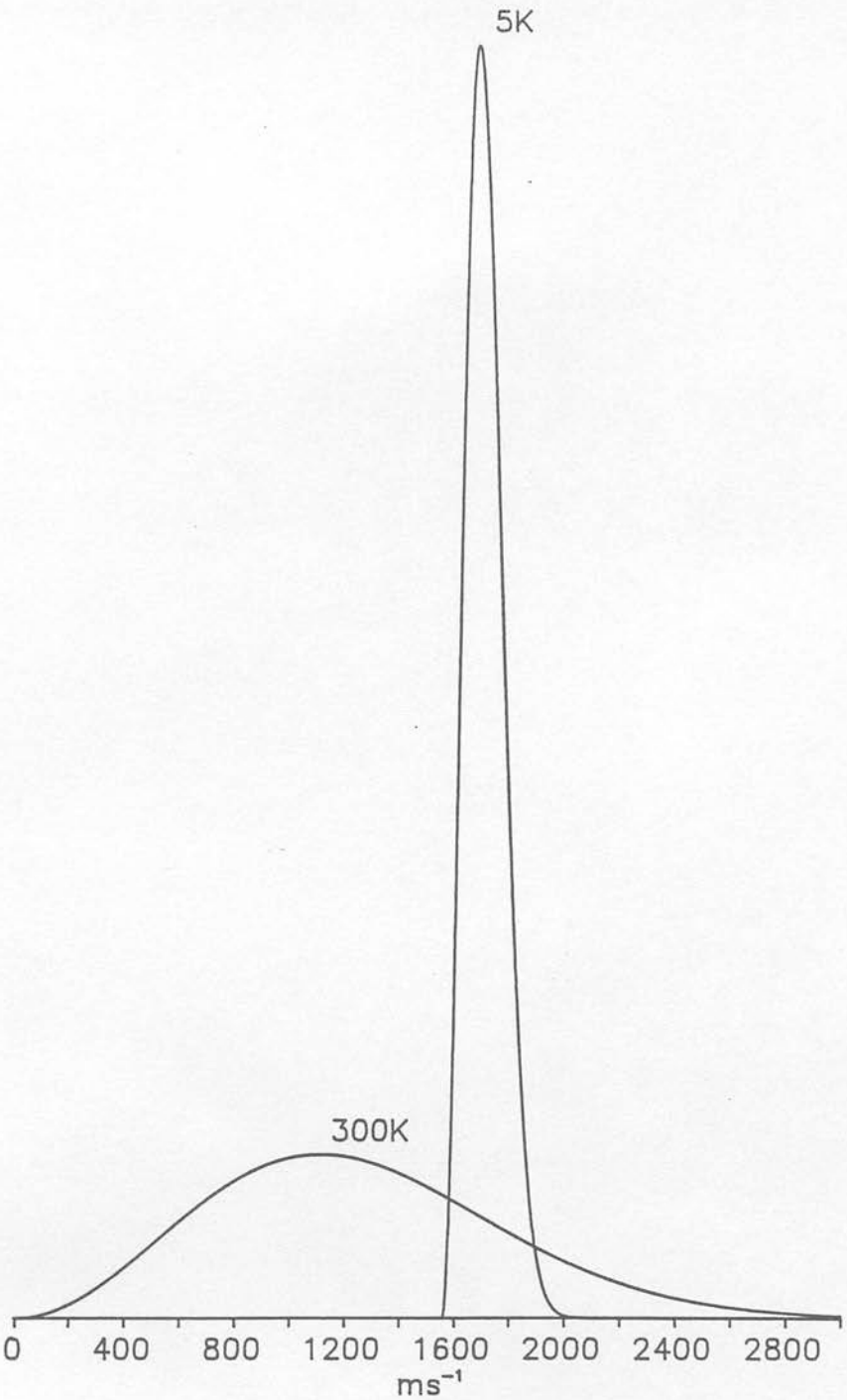

This gave an increase in the ion signal observed over that expected from a room temperature sample for individual rovibronic excitations. The R2PI spectra recorded for the copper and silver dimers in chapters 5 and 6 show no vibrational excitation and population of rotational levels up to $J'' \simeq 20$ in the ground state.

The degree of cooling achieved could be altered by changing the backing pressure [14] or the carrier gas [19] [20]. However both of these methods had adverse effects on the cluster intensity and some gases (e.g. argon) are known to form Van der Waals' complexes with metallic species [18].

2.4 Time of Flight Mass Spectrometer

The time of flight mass spectrometer (TOFMS) employed in the analysis of the metal clusters was a variation of the double field design of Wiley and McLaren (see figure 2.1) [15]. The design was modified for use with a molecular beam and laser photoionisation, as described below, by the inclusion of deflection plates and ports in the sides of the ion source. The 1.21 metre long flight tube was aligned perpendicular to the axis of the molecular beam and surrounded by a cryogenic dewar to maintain a low background pressure. The time of arrival profile of the ions at the end of the flight tube was monitored by a Micro - Channel Plate detector (Jordan dual MCP). The output from the MCP was amplified, digitised and stored by the PC - AT as described in chapter 3.

The ion source of the TOFMS was surrounded by a copper cryoshield, attached to the base of the cryogenic dewar surrounding the flight tube. The

cryoshield helped maintain a low pressure in the source region and prevent any back scattered material from the beam colliding with the ions formed. The use of copper reduced any stray electric fields which would affect the performance of the TOFMS. The cryoshield had ports in each side to permit passage of the molecular and laser beams. After passing through the source of the TOFMS the molecular beam was dumped in the B chamber to reduce backscattering of the beam into the TOFMS ion source.

The repeller, draw - out - grid (DOG), and ground plane were fabricated from 0.5 mm stainless steel, 72 x 72 mm. The draw out and ground plates had a 40 mm diameter hole, covered with nickel mesh (90% transmission, 0.074" spacing) to effect transmission of the ions into the flight tube of the TOFMS. The voltages applied to the plates were supplied by two Power Designs high voltage power supplies and one LeCroy CAMAC based power supply (see chapter 3). A third Power Designs unit was used to supply the deflection plates.

The field applied to the deflection plates was to counteract the momentum of the ions created in the molecular beam, perpendicular to the axis of the TOFMS. The clusters were accelerated to the speed of the beam during the supersonic expansion. This momentum had to be compensated for to allow the clusters to traverse the drift tube of the TOFMS after ionisation. The field applied to the deflection plates was fixed and as such could only direct a limited mass range onto the detector at any one time. This gave rise to the strongly mass dependent transmission function of the TOFMS observed in the mass spectra (see chapter 4). The voltages applied to the repeller and DOG were fixed by the geometry of the TOFMS, so as to focus individual ion packets at the detector.

The parameters of the TOFMS used in the work presented in this thesis were:

$V_{repeller}$ = 3015 V

V_{DOG} = 2555 V

distance repeller to DOG = 32 mm

distance DOG to ground plane = 6 mm

Ionisation laser beam midway between repeller and DOG.

Ionisation laser width = 1.6 mm

The maximum resolution of a mass spectrometer is defined as the maximum mass at which there is complete separation of adjacent masses. Wiley and McLaren [15] and other workers [16] have presented detailed analyses of the factors affecting resolution in time of flight mass spectrometers. The main non - instrumental factors are the initial spatial and velocity spread of the ions formed in the ion source. The supersonic beam used in this work provides a sample with a low velocity spread due to the translational cooling achieved in the expansion. The narrow laser beam used to accomplish ionisation further reduces the velocity spread by sampling only the coldest central part of the beam, as well as creating the ions with a very small spatial spread. The above conditions gave a maximum observed resolvable mass of ~ 350 a.m.u., sufficient for the main purpose of recording mass resolved R2PI spectra of the 1^{st} and 2^{nd} row transition metal dimers.

2.5 Lasers

The present work used the output from 3 different types of high powered pulsed laser systems to perform the vaporisation of the target rod and the photoionisation of the species in the molecular beam. The first was an ArF excimer laser, the second a Nd:YAG laser and finally a high resolution tunable dye laser. The latter laser was pumped by a XeCl excimer laser. These three laser systems and their usage are described in detail in the following sections.

2.5.1 ArF Excimer laser

Photoionisation of the molecular beam was carried out using a Lumonics TE 860-4 excimer laser filled with an argon fluoride mixture (20% Ar, 0.4% F_2, balance He, total pressure = 35 psi.) [23]. This laser emitted broadband radiation centred at 193 nm (6.4 eV, 51616 cm^{-1}) which was energetic enough to ionise all the transition metal clusters with one or two photons [25]. This laser and the XeCl excimer laser used to pump the dye laser operated by passing an electrical discharge through the gas mixture in the laser cavity. The switching of the high voltage (~ 40 KV) was performed by a thyratron. This gave a peak pulse energy of 60 mJ in a 10 ns FWHM pulse. The dimensions of the unfocused output beam were 28 mm x 16 mm at the throat of the laser. The divergence of the beam between the laser and the A chamber was measured as 0.402° vertically and 1.408° horizontally.

The pulse energy of this laser was attenuated when necessary by inserting wire gauze in the beam path. The width of the beam in the ion source of the

TOFMS was narrowed using an iris and a pair of razor blades aligned with the axis of the molecular beam, placed at the window to the A chamber, and estimated to be 1.6 mm from the gap between the blades and the divergence of the beam. The laser power in the TOFMS ion source was typically 0.5 MW cm^{-2}. The output energy fell with use to around 20 mJ/pulse after 1 - 2 hours use. This meant that efficient use had to be made of the available laser shots.

The firing of the laser was controlled by using the charge on demand (COD) mode. Two trigger pulses were applied to the charging circuit, the first initiated charging of the capacitors and the second triggered the thyratron to produce the discharge. The output of this laser was used on its own to perform non resonant ionisation, or with the output of the tunable dye laser described in section 2.5.3 to perform resonant enhanced MPI spectroscopy on the metal clusters entrained in the beam.

2.5.2 Nd:YAG laser

Vaporisation of the metal target rod was performed using the Q-switched output of a Nd:YAG laser. The laser used for the current work was a Quanta - Ray DCR / IIA, optimised for a 10 Hz repetition rate [21]. This laser contained two doped glass laser rods arranged as an oscillator - amplifier pair. The operation of this laser required the application of three trigger pulses to the master oscillator, flashlamps and the Q - switch. The master oscillator closed the high voltage relay which applied the voltage to the Pockels Cell Q - switch, and initiated charging of the capacitors used to create the flashlamp discharge. The flashlamp trigger fired the flashlamps surrounding the oscillator and amplifier

rods to pump the lasing transition. The Q - switch trigger released the high voltage relay supplying the Pockels Cell. This produced a short, high energy pulse required for vaporisation. The maximum pulse energy was 800 mJ of 1.06 µm radiation in an 8 ns FWHM pulse when the delay between the flashlamps and the Q - switch was ~ 250 µs. Adjustment of the pulse energy was accomplished by changing this delay using the computer controlled pulse delay generators (see chapter 3).

The maintenance of a constant repetition rate was essential when using this laser as any change in the heat input to the laser rods caused a corresponding change in the thermal lensing. Changes in the thermal lensing altered the beam profile and collimation. The PC - AT controlled the repetition rate as described in the next chapter.

The 1.06 µm output from this laser was frequency doubled using a KDP crystal mounted in a thermostatically controlled oven. The residual infra - red radiation was separated from the visible 532 nm radiation using a Pellin - Broca prism and directed into a beam dump. The 532 nm output was focused by a 1 m lens to a 1 mm spot on the surface of the target rod in the cluster source. The alignment of the laser with the cluster source was checked with the main chamber evacuated by raising the target rod out of the path of the laser and monitoring the beam output through the rear window of the chamber. The inlet window was mounted on an extension arm to avoid accumulation of sputtered material from the vaporisation process.

The target rod was rotated and translated in the faceplate, since if it was

allowed to remain stationary there was a rapid fall off in the cluster intensity. The reasons for this reduction have been investigated by Ready [13] and it is believed to be due to the plasma formed by the leading edge of the laser pulse being trapped in the hole created by vaporisation of the surface, and absorbing the incoming laser radiation, thus preventing removal of more material.

The choice of 532 nm radiation to perform the vaporisation was made purely on the grounds that it was easier to use than any of the available alternatives. Infra - red (Nd:YAG fundamental or CO_2) and ultra - violet (excimer) were considered unsuitable as they are not visible and therefore less easy to align with the cluster source. The green 532 nm radiation was easy to align but does suffer from the high reflectivity of most metals to this wavelength [13] which was not a problem as the laser power was easily increased to compensate for this. The laser power and focus position were adjusted as described in chapter 4.

Similarly the use of Q - switched radiation was not optimal as it not only vaporises the metal but produces a superheated plasma which must be quenched before condensation can take place. The alternative un Q - switched radiation is believed to remove material as large molten droplets unsuitable for the formation of clusters [13] [14].

2.5.3 High resolution dye laser

Spectroscopic studies of the metal dimers in the beam were carried out using a tunable high resolution dye laser (Lambda - Physik 3002EC) [22] to perform resonant two photon ionisation (R2PI). Both one colour and two colour R2PI

were used. For two colour R2PI the fixed frequency ArF excimer laser described above was used to effect ionisation out of the excited state populated by the dye laser. The two laser beams were spatially and temporally overlapped and counterpropagated through the ion source of the TOFMS.

The dye laser was pumped by an excimer laser (Lambda-Physik MSC201) operating on the 308 nm line of XeCl. This excimer operated in a similar manner to the ArF laser described above. The only difference was that only one trigger pulse was required to fire the laser. The output of this laser appeared to contain more temporal jitter relative to the trigger pulse than the ArF laser as measured with a photodiode and an oscilloscope. This led to problems in maintaining temporal overlap of the dye laser output with that of the ArF excimer in two colour experiments (see chapter 6 and section 3.2.9).

For the work described in chapters 5 and 6 the following dyes dissolved in methanol were used in the dye laser:

Coumarin 153: 522 nm - 560 nm peak at 540 nm

Coumarin 120: 423 nm - 462 nm peak at 441 nm

The 3002EC dye laser contained 3 cuvettes through which the dye was continuously circulated during operation. The XeCl excimer laser was used to transversely pump the three cuvettes containing the circulating dye solution. The oscillator cuvette was located in a Hansch type laser cavity [24], the end reflectors being a Littrow grating (600 lines mm^{-1}) and a dielectric reflector. The output from the oscillator passed through a prism beam expander (PBE)

before reaching the grating. This reduced the power density to avoid damaging the grating as well narrowing the bandwidth by using more of the grating [24]. The beam then passed back through the oscillator cuvette which acted as a preamplifier stage. The beam was further amplified as it passed through the other two cuvettes. A telescope was used to collimate the beam between the latter two cuvettes. Wavelength tuning was accomplished by changing the angle of the grating.

Ultra - violet radiation was produced by second harmonic generation (SHG) using a potassium dihydro phosphate (KDP) crystal (Lambda-Physik FL31). This crystal was mounted on a motorised stage along with a quartz compensating crystal (QCC) to correct for any beam walkoff caused by the SHG crystal. Beam walkoff was critical in the experiments performed in the present work as the laser was situated 8 metres from the rest of the experiment, so that only a very small amount of walkoff was required to destroy the alignment with the supersonic beam in the TOFMS ion source or the beam from the ArF excimer laser. The frequency doubled light was separated from the residual fundamental with a UG5 filter placed in the beam after the QCC.

For high resolution spectroscopic studies of the metal dimers, the output of the laser was line narrowed using an intra - cavity etalon (Lambda-Physik FL83). The air spaced Fabry Perot etalon used had a free spectral range of 1 cm^{-1} and provided a resolution of 0.04 cm^{-1}. The etalon was mounted on a motorised stage between the PBE and the grating. Wavelength tuning was accomplished by synchronously moving the grating and the etalon.

The wavelength scanning and tracking of the SHG crystal in this laser was controlled by a dedicated microprocessor (Lambda-Physik FL538) running a program stored on an EPROM. This controller synchronously moved the grating and the etalon, as well as tracking the SHG crystal when frequency doubling was required. The SHG crystal was tracked according to a function calculated by optimising the angle of the SHG crystal at a number of points throughout the expected scan range. The wavelength tuning was synchronised with the rest of the experiment by the PC - AT (see section 3.2.6).

The power density was adjusted by focusing or collimation of the beam. For one colour experiments where the output was frequency doubled, ultra - violet, light the optimum signal was obtained by collimating the beam with a 5 times telescope [26]. Single lens focusing was found to cause excessive power broadening of the rotational transitions as well as an increase in the amount of non resonant ionisation. Attenuation by splitting off part of the ultra violet beam with a quartz beam splitter typically led to a total loss of signal as the focused power density dropped below that required for two photon absorption. The power density was more easily controlled with the telescope by adjusting the amount of collimation. For two colour experiments using visible radiation direct focusing of the beam with a single lens was used as it was trivial to attenuate the visible beam using neutral density filters. During two colour experiments the ArF excimer laser output was attenuated to increase the contrast between the resonant signal and the non resonant background.

Relative wavelength calibration of the high resolution spectra obtained using the 3002EC laser was achieved by splitting off part of the output beam before

frequency doubling and passing it through a confocal etalon (Lambda-Physik FL54). This etalon had a free spectral range of 0.1 cm^{-1}. The interference fringes generated by passing the beam through this etalon were monitored by a photodiode the output of which was recorded by a sample and hold circuit for capture by the data system (see chapter 3). The variation in the intensity of the transmitted light as the wavelength was tuned over the free spectral range of the etalon produced a series of fringes spaced at 0.1 cm^{-1}, which were used as an accurate relative wavelength monitor. The confocal etalon was calibrated by recording the fringes along with an iodine LIF spectrum in the wavelength region of interest. Using the accurately known iodine lines [27], the fringe spacing was calculated by a least mean squares fit [28]. This gave a spacing of 0.10 cm^{-1} between the fringes, which was used to determine the spacing of the rotational lines in the R2PI spectra of the metal dimers (see chapters 5 and 6).

2.6 Multi Photon Ionisation and spectroscopy

The analysis of the metal clusters entrained in the beam was carried out using resonant and non - resonant multi photon ionisation (MPI) in the ion source of the TOFMS [10] [17]. The overall cluster distribution was probed by non - resonant MPI using the fixed frequency ArF excimer laser. This was the technique used for the mass spectroscopic studies described in chapter 4.

The absorption of the photons in non - resonant MPI need not correspond with a real excited state of the molecule as shown in figure 2.6(a). Resonant MPI requires the existence of a rovibronic level at the energy above the ground state of the exciting photon, with the second photon causing ionisation out of the

intermediate state (see fig 2.6(b) and (c)). When this is combined with mass selective detection as in the present work, it is possible to resolve the individual isotopomers. This is not possible in non mass selective MPI or other spectroscopic techniques such as LIF.

When investigating states lying less than half way to the ionisation threshold the second photon must be more energetic than the first. In the current work the ArF excimer laser was used to provide the additional photon in the two colour experiments. The photon for the initial electronic excitation was provided by the high resolution dye laser.

A major problem encountered in the two colour experiments was maintaining the temporal overlap of the lasers. This is discussed further in the following chapter. In cases where the cluster has a low ionisation potential part of the XeCl excimer laser output used to pump the dye laser could have been used to effect ionisation, thus removing any possible jitter between the excitation and ionisation lasers. This was not practical in the work on the silver dimer presented in chapter 6 as ionisation out of the excited state would have required two XeCl photons (308 nm, 32467 cm^{-1}). A 1 + 2 absorption scheme was not considered viable as it would have required too much of the XeCl output to overcome the decreased cross section for two-photon absorption ($\sim 10^{-50}$ cm^4 sec) over one-photon absorption ($\sim 10^{-20}$ cm^2) [10] [17], leaving insufficient to pump the dye laser.

Figure 2.6
Two photon ionisation schemes

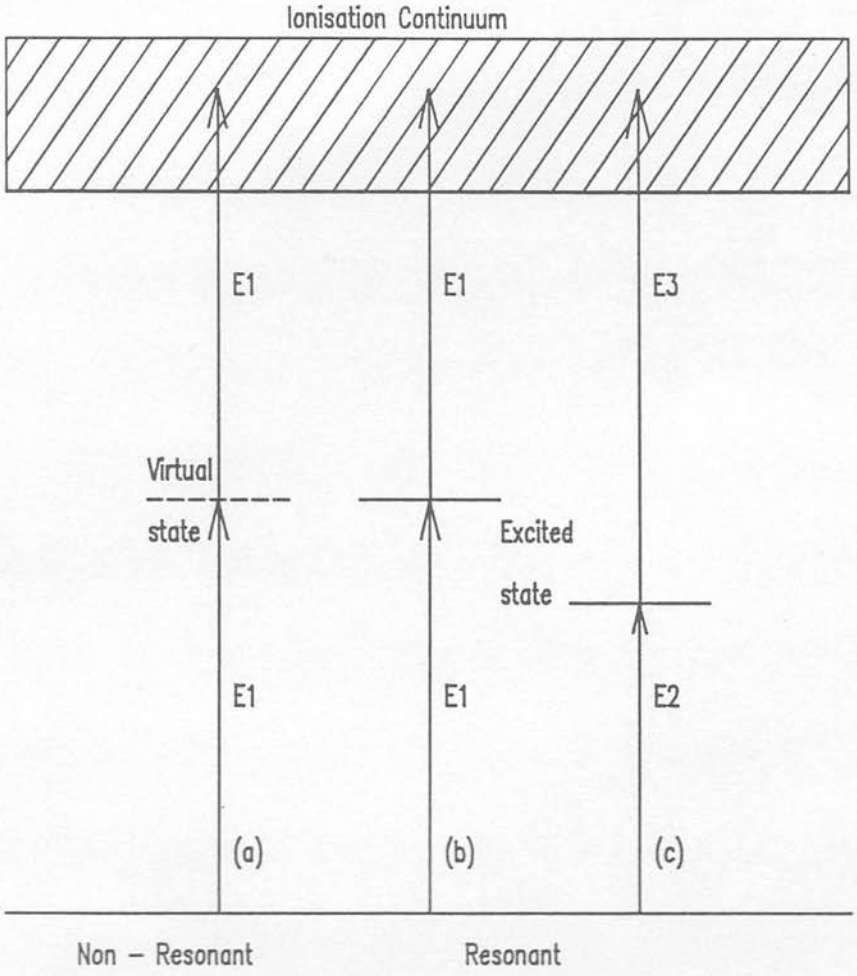

E1 >= I.P./2

E3 > I.P./2 > E2

The pulse energy of the lasers used for R2PI required careful adjustment to obtain the optimum signal. High pulse energies caused power broadening of the rotational features, fragmentation [12] [11], and a high non resonant background in one colour experiments. Too little power in the dye laser output gave a poor signal to noise ratio for the resonant signal over the non resonant background.

When performing two colour R2PI it was possible to record time resolved spectra by scanning the delay between the two lasers to map out the decay of the upper state after excitation. The resolution available in the time resolved studies was limited by the width of the laser pulses, with short decay profiles being hidden by the convolution of the two laser pulses, as described in chapter 6.

References

[1] Fluendy M.A.D., Lawley K.P., *Chemical Applications of Molecular Beam Scattering*, Chapman and Hall, London, 1973.

[2] Kantrowitz A., Grey J., Rev. Sci. Instrum., **22**, p 328, (1951)

[3] Kantrowitz A., Grey J., Rev. Sci. Instrum., **22**, p 333, (1951)

[4] Smalley R.E., Wharton W., Levy D., Acc. Chem. Res., **10**, p 139, (1977)

[5] Lubman D.M., Rettner C.T., Zare R.N., J. Phys. Chem., **86**, p 1129, (1982)

[6] Gole J.L., *Metal Clusters, ed. Moskovits M.*, Wiley Interscience, Toronto, 1985.

[7] Toinies J.P., Winkelmann, J. Chem. Phys., **66**, p 3965, (1977)

[8] Adams T.E., Rockney B.H., Morrison R.J.S., Grant E.R., Rev. Sci. Instrum., **52**, p 1469, (1981)

[9] Campargue R., Rev. Sci. Instrum., **35**, p 111, (1964)

[10] Johnson P.M. Otis C.E., Ann. Rev. Phys. Chem., **32**, p 139, (1981)

[11] Brucat P.J., Zheng L.S., Pettiette C.L., Yang S., Smalley R.E., J. Chem. Phys., **84**, p 3078, (1986)

[12] Durant J.L., Rider D.M., Anderson S.L., Proch F.D., Zare R.N., J. Chem. Phys., **80**, p 1817, (1984)

[13] Ready J.F., *Effects of High Power Laser Radiation*, Academic Press, 1971.

[14] Powers D.E., Hansen S.G., Geusic M.E., Pulu A.C., Hopkins J.B., Dietz T.G., Duncan M.A., Langridge-Smith P.R.R., Smalley R.E., J. Phys. Chem., **86**, p 2556, (1982)

[15] Wiley W.C., McLaren I.H., Rev. Sci. Instrum., **26**, p 1150, (1955)

[16] Opsal R.B., Owens L.G., Reilly J.P., Anal. Chem., **57**, p 1884, (1985)

[17] Parker D.W., *Ultra Sensitive Laser Spectroscopy, ed. Kliger D.S.*, Academic Press, New York, 1983.

[18] Gough T.E., Knight D.G., Scoles G., Chem. Phys. Lett., **97**, p 15, (1983)

[19] Amirav A., Even U., Jortner J., Chem. Phys., **51**, p 31, (1980)

[20] McClelland G.M., Saenger K.L., Valentini J.J., Herschbach D.R., J. Phys. Chem., **83**, p 947, (1979)

[21] Quanta - Ray, *DCR II/A Pulsed Nd:YAG Laser Instruction Manual*, Mountain view, CA., U.S.A., 1982.

[22] Lambda Physik, *FL3001/2 Instruction Manual*, Gottingen, W. Germany, 1986.

[23] Lumonics Inc., *Series TE-860-4 Excimer Laser Instruction Manual*, Kanata, Ontario, Canada, 1984.

[24] Demtroder W., *Laser Spectroscopy*, Springer - Verlag, Berlin, 1981.

[25] Morse M.D., Chem. Rev., **86**, p 1053, (1986)

[26] Halliday D., Resnick R., *Physics*, Wiley Interscience, New York, 1978.

[27] Gerstenkork S., Luc P., *Atlas du Spectre D'Absorption de la Molecule D'Iode 14800 - 20000 cm^{-1}*, Editions du Centre National de la Recherche Scientifique, Paris, 1978.

[28] Bevington P.R., *Data Reduction and Error Analysis for the Physical Sciences*, McGraw - Hill, New York, 1969.

Chapter 3
Development of the Data System for the Cluster Apparatus

3.1 Introduction

In order to perform the experiments outlined in the previous two chapters a sophisticated set of electronic instrumentation was required both to control the apparatus and record the data. The instruments formed part of an integrated system of hardware and software developed to enable a microcomputer to be used to control the apparatus described in the previous chapter. A schematic of the hardware of the data system is shown in figure 3.1. The use of a computer to control the experiment and record the data had a number of advantages in that the data could be displayed on a V.D.U. as an experiment was in progress, and once optimised the experimental parameters could be easily reset. Digital storage of the data made the task of analysis easier as it was already in machine readable form. This chapter describes the instrumentation used, the software developed to make use of it, and finally a section on the performance of the complete data system.

The data system was designed round an IBM Personal Computer - AT (PC - AT) and CAMAC instruments.

Figure 3.1
Block diagram of the electronic and computer hardware
used for control and data logging

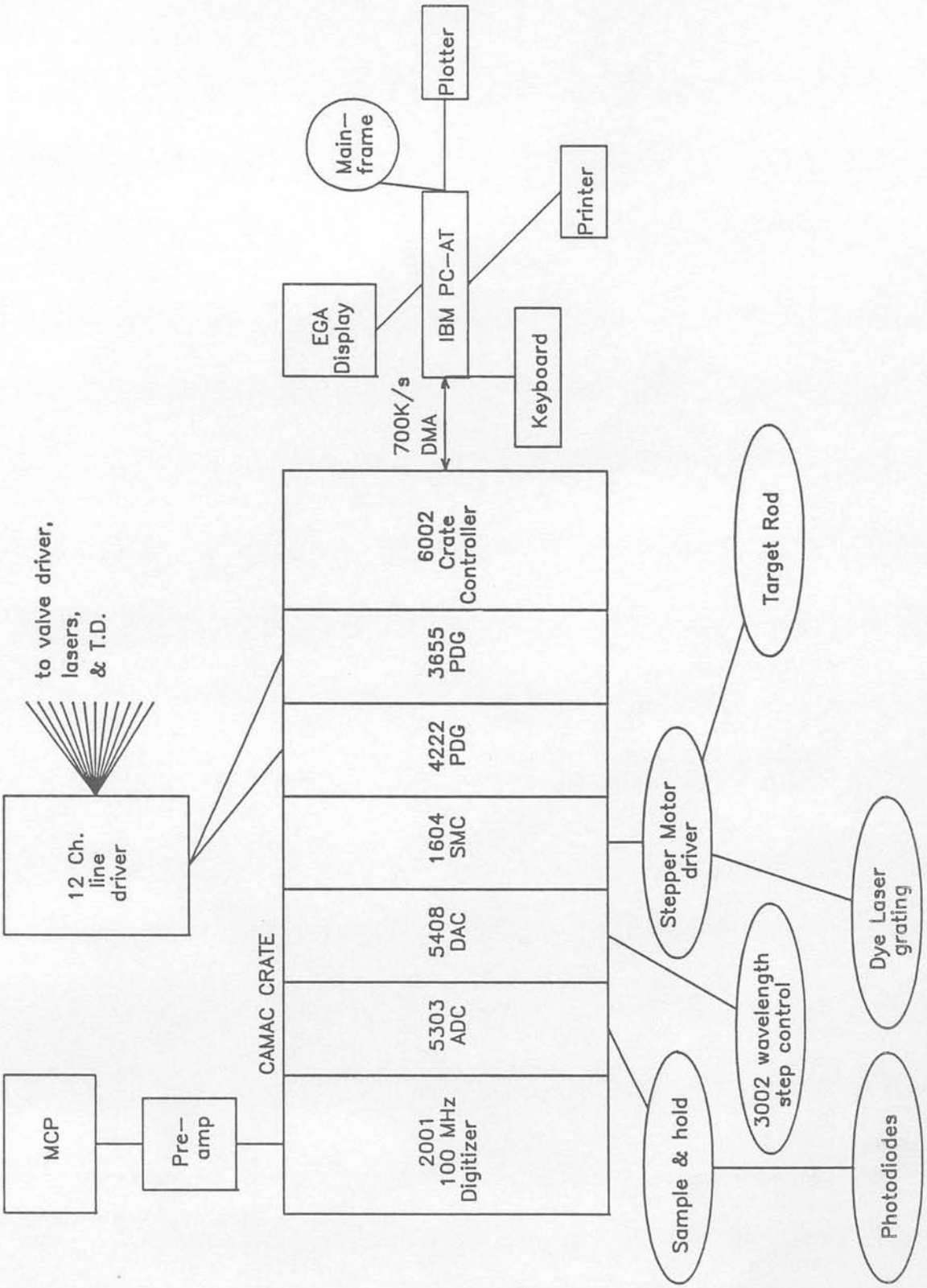

3.1.1 CAMAC instrumentation

All the control and measurement instrumentation was based on the IEEE CAMAC (Computer Automated Measurement And Control) standard for plug - in modules [1]. This standard defines a common dataway to which a wide range of instruments can be connected. The instrument modules slot into a *crate* whose backplane supports the power and data lines. Connection to the data and power lines is through an edge connector at the back of each module. 24 bidirectional read / write lines are used in parallel to transmit the data. Associated with these are lines for directing the commands (known as F lines), and data (D) to the correct module (N), subaddress lines (A) for accessing specific parts of the module addressed, and lines used by the modules to acknowledge commands (Q and X) and request attention (L). Individual N and L lines connect each station to the crate controller, the other lines run in parallel to all the stations. The current work employed a WES model FHD-HV3 24 station crate.

The crate controller consisted of a dedicated microprocessor located in the rightmost station, which controlled the functioning of the crate. This processor accepted the commands from the computer controlling the experiment and oversaw the transfer of data between the computer and the CAMAC modules, passing them to the appropriate module. Data transfer took place a word (8, 16, or 24 bits) at a time (word transfer) or in blocks by direct memory access (DMA), depending how much there was. Each of the modules used in the current work is described below.

The DSP 6002 crate controller was programmed through a DSP PC004 interface card located in an 8 bit expansion slot of the PC - AT. An LED display on the front panel of the 6002 showed the dataway lines in use, and was used for debugging the software. The 6002 / PC004 combination was capable of DMA transfer at 700 Kb s^{-1} with the PC - AT. The PC004 mapped all the CAMAC dataway lines to 12 consecutive ports on the i/o expansion bus of the PC - AT.

A DSP 2001 transient digitiser (TD) was used to record the time of arrival profile from the MCP detector. The digitising rate and record length were selectable by front panel switches. The memory was divided into different record lengths selectable in powers of 2 from 256 bytes to 32 Kb. The digitising rate was selectable for 100, 50, 20, 10, 5, 2, and 1 MHz. After the TD was armed by a CAMAC dataway command the input signal was continuously sampled and stored at the chosen rate until a stop trigger was applied. The TD then continued to sample the input for the selected record length. The signal stored before the stop trigger could be observed by setting a number of pre trigger samples to be kept, in this case the number of samples recorded after the trigger was reduced by the number of pre trigger samples. The TD had 8 bit resolution with a range of 512 mV, giving a minimum detectable change of 2 mV. The output from the MCP passed through a 100 times amplifier (Pacific Instruments 2A50 video amplifier) attached directly to the MCP to amplify the signal and lessen the effect of any stray electrical noise picked up by the cable connecting it to the TD.

Slowly varying signals such as the output of the photodiodes monitoring the etalon fringes and laser power were recorded by a gated sample and hold circuit. A BiRa 5303 16 channel, 12 bit analogue to digital converter (ADC) was used to

record the sample and hold signal. The zero to five volt scale used gave a resolution of 1.2 mV.

Analogue output was accomplished using a BiRa 5408 12 bit digital to analogue converter (DAC). This had 8 independently programmable channels providing continuous output of the signals being monitored during wavelength scans. Trigger pulses for synchronising the tuning of the dye laser were produced using the DAC by stepping the output voltage of one of the channels, as shown in example 2 below. Normally this was used with an output range of ± 10 V.

The movement of the target rod was controlled using a Hytec 1604 stepper motor controller (SMC) connected to a stepper motor driver unit. The SMC was programmed by the PC - AT with the number of steps to be moved by the motor. During large movements of the motor the SMC ramped the stepping speed from a slow starting rate to a maximum and back again to avoid loss of synchronisation due to the inertia of the motor. This was not critical for movement of the target rod, but in other experiments not described in this thesis the SMC was used to control the position of the grating in a dye laser. In this case it was vital that the stepper motor moved exactly the number of steps requested, otherwise the computer lost track of the grating position. The module contained inputs for detecting when limit switches were opened, or a power failure occurred in the motor. The driver unit was capable of moving the stepper motors full or half steps.

Two programmable pulse delay generators (PDGs) were used to generate the trigger pulses required to run the experiment. A Kinetic Systems 3655 PDG

with 8 channels was used along with a 4 channel LeCroy 4222 PDG. The former had a minimum delay step of 1 μs, and the latter 1 ns. Both produced TTL pulses which were boosted by a custom 12 channel line driver unit housed in a NIM bin module. The 4222 was triggered off one of the channels of the 3655 which was triggered internally from the dataway by the PC - AT.

The individual CAMAC modules were programmed using integer numbers as commands. The functions used to issue these commands, *camac_out* and *camac_in* are given in code 3.1. First the station number of the module was sent followed by the command to be executed, then the subaddress within the module. If the command was a write command the data followed the subaddress. A CAMAC cycle was then executed to initiate the command. For a read command the module returned the requested data. The following examples, written in C, show how the DAC was used to output 100 5 volt pulses and the ADC used to read in voltage levels.

example 1:

```
camac_out(DAC,16,1,2048);  /* set channel 1 to 0 V. */
for(i=0;i<100;i++){
 camac_out(DAC,16,1,3072); /* set channel 1 to 5 V */
 camac_out(DAC,16,1,2048); /* reset channel 1 to 0 V. */
 }
```

Code 3.1 - Routines for input & output to the CAMAC crate

```
unsigned camac_in(n,f,a)
unsigned n,f,a;
{
unsigned lowbyte,highbyte;
outp(NC,n); outp(AC,a); outp(FC,f);
outp(CC,0); /* execute CAMAC cycle to send command to crate */
nop(); /* waste some time while CAMAC module returns data */
lowbyte = inp(RL);  highbyte = inp(RM); /* read in data */
return (lowbyte + highbyte*256);
}



void camac_out(n,f,a,d)
unsigned n,f,a,d;
{
outp(NC,n); outp(AC,a); outp(WL,d%256); outp(WM,d/256);
outp(WH,0); /* set 3rd byte to 0 as only 16 bits used */
outp(FC,f);
outp(CC,0);
 /* execute CAMAC cycle to send command & data to crate */
}
```

NC, AC, CC, WL/M/H are the port numbers to which the CAMAC dataway lines are mapped on the i/o bus of the PC - AT.

example 2:

```
for(i=0;i<8;i++){
adcv[i]=camac_in(ADC,2,i);/* store value from ADC in array. */
}
```

DAC and *ADC* were the station numbers in the CAMAC crate occupied by the DAC and the ADC. 16 was the command for writing to the DAC and 2 was the command for reading from the ADC. The appropriate channel was addressed as a subaddress within the module. The other CAMAC modules were programmed in a similar fashion to that above, and further modules could be added with a minimal amount of additional programming.

3.1.2 IBM PC - AT microcomputer

The PC - AT contained an Intel 80286 (16 bit) processor and 80287 maths coprocessor. The main 80286 processor was originally clocked at 6 MHz, which was increased to 8 MHz during the present work by substituting a different microprocessor crystal. Two disk drives, one 20 megabyte (Mb) hard disk and one 1.2 Mb 5 1/4" floppy drive, were used for storing the software and data. The system contained 640 kilobytes (Kb) of random access memory (RAM). The 640 x 350 pixel display was driven by an IBM enhanced graphics adapter (EGA) equipped with 256 Kb of RAM. The graphics memory was split into 8 text pages and one 16 colour graphics page for the current work. This allowed the use of pop - up menus which were written once and recalled by setting the appropriate page to be the display page.

3.2 Experimental control and data logging - the THOR program

The software required to run the experiment was written using the 'C' programming language (Microsoft v 5.00), with some assembler (IBM MACRO Assembler v 2.00) for the time critical functions required to process the data as it was acquired. The use of assembler allowed precise control over the code whereas high level language compilers generated unnecessary instructions which slowed the processing. 'C' was used as it provided many of the low level functions required to access the CAMAC interface card (see code 3.1) and was preferable to the library of assembler functions provided with the crate controller and interface card. The compiled code was very compact, and when optimised ran reasonably fast. This was an important consideration with the limited amount of memory available. This compared with an initial attempt using FORTRAN which produced a large volume of compiled code, required a large amount of programming in assembler, and was not particularly fast.

The software was developed to provide the functions required for setting up and performing the experiments, automating the control as far as possible with single keystroke commands selected from an on screen menu. Two separate menus were used, one for executing all the data acquisition functions, storing and retrieving data on disk, hard copy output etc., the other for modifying the style of the display and experimental parameters while an experiment was in progress. The latter menu contained functions to change the axis scales to zoom in on part of the spectrum, change the number of shots to be averaged, halt data collection, type comments on the screen, etc.

The completed software package was called THOR and is archived at Edinburgh as described in appendix A.

The program had three modes of operation; time of flight (TOF), timescan (TSCAN), and wavelength scan (FSCAN). These three modes allowed mass spectrometric, time resolved and spectroscopic investigations of the metal clusters to be carried out. Each of these modes is described in detail below.

3.2.1 Repetition rate

The constant repetition rate demanded by the Nd:YAG laser (see section 2.5.2) was accomplished using the interrupt mechanism of the PC - AT. This was preferable to using an external clock source and having to synchronise the computer with the rest of the experiment. By using the computer to trigger each experimental shot it was possible to ensure that any changes made to the experimental parameters were carried out in the dead time between shots. The timer in the PC - AT was set so as to generate an interrupt at twice the desired repetition rate by loading the number of computer clock cycles (1.197 MHz) that had to pass between each interrupt into the counter for the event timer. The vector for the timer interrupt (interrupt number 8) was changed to point to an interrupt handler function within the program. Upon receipt of an interrupt from the timer the processor jumped to execution of the handler function which counted how many times it had been called and alternately called one of two other functions.

Code 3.2 - The TIC function

```
void tic()
{
int i;
if(TDSTART){TDSTART=0; TOCGO=1;} /* flag TOC to collect data */
lpulsers(); /* load time delays into PDGs */
f9clear(TD); f9clear(NANO);  /* clear digitiser & 4222 PDG */
f26enable(TD); f26enable(NANO); /* enable digitiser & 4222 PDG */
camac_out(PULSER1,25,0,0);
 /* trigger 3655 pulser to initiate expt. cycle */
if(eachshot) pplot_on_tic();
 /* plot data on screen during timescan */
if(!(tics%ntik)){
  /* move target rod, ntiks = number of shots between movements */
 camac24_out(STEMOT,16,1,(long)1);
 camac24_out(STEMOT,23,12,(long)0x00000FC0);
 camac24_out(STEMOT,19,12,(long)0x00000400);
}
tics++;                                  /* record this tic */
}
```

TD, NANO, PULSER1, & STEMOT at the station numbers of
the modules in the CAMAC crate.

Code 3.3 - The TOC function

```
void toc()
{
unsigned i,xplot_on_toc;
double funny;
if(TOCGO) {TOCGO=tocs=TDDONE=0;}
 /* reset TDDONE to show data collection in progress */
if((tocs>=nshots)||TDDONE||(sumshots>=shots2sum))
     {TDDONE=1; return;}
 /* check to see if TOC should be executed & return if not */
readADCs(); /* read data from ADC */
tddump_dma(TD);  /* read data from digitiser */
fl0clear(TD); /* reset digitiser for next shot */
if(NORMexci)
 /* if power normalisation required calculate normalisation
    constant */
 {
 if((thispow1&&(POWOPT==1||POWOPT==2))||
    (thispow1&&thispow2&&POWOPT==3))
  {
  switch(POWOPT){
 /* POWOPT = 1, 1 colour - 1 photon;
    POWOPT = 2, 1 colour - 2 photon;
    POWOPT = 3, 2 colour - 2 photon */
   case 0:
    normal=1;break;
   case 1:
    normal =(unsigned)((long)16384*(long)avrgpower1/
                       (long)thispow1);
    break;
   case 2:
    normal=(unsigned)((long)16384*
                      (((long)avrgpower1*(long)avrgpower1)/
                      ((long)thispow1*(long)thispow1)));
    break;
   case 3:
    normal=(unsigned)((long)16384*(((long)avrgpower1*
                      (long)avrgpower2)/
                      ((long)thispow1*(long)thispow2)));
    break;
   }
  }
 else normal = 1; /* otherwise set normalisation factor to 1 */
 }

if(TOFMS) /* for Time of Flight mode */
 {
 xplot_on_toc = (tocs * 3) + 460;
 stl(xplot_on_toc,9,xplot_on_toc,0,129);
  /* plot marker for this shot on screen */
 sumshots++;tocs++;
```

```
 /* record this shot & total number of TOC cycles */
 tdaccum(BYTEBUF,TDBUF,tdpts,normal*NORMexci,TDSUM,tdoffset);
 /* normalise & sum data stored in BYTEBUF into TDBUF */
 TDSUM=1;
 /* set TDSUM so that tdaccum adds next shot to stored data */
 }
else {sumshots++;tocs++;}
/* otherwise just record this shot & total number of TOC cycles */

if(TSCAN) /* for timescans */
 {
 if(setdelay(p2scan,tparm[p2scan].step))
  {
  beep();
  locate(10,10,1);cprintf("Timing error, Data accum. stopped");
  TDDONE=1;
 }
 /* increment time delay, give warning if out of range */
 scan_update(); /* record data */
 databin=scanbin;
 /* record this bin for use in TIC when updating display */
 scanbin++;    /* update bin for next shot */
 }
}
```

Figure 3.2 Typical timing of events required within one experimental cycle (times in microseconds)

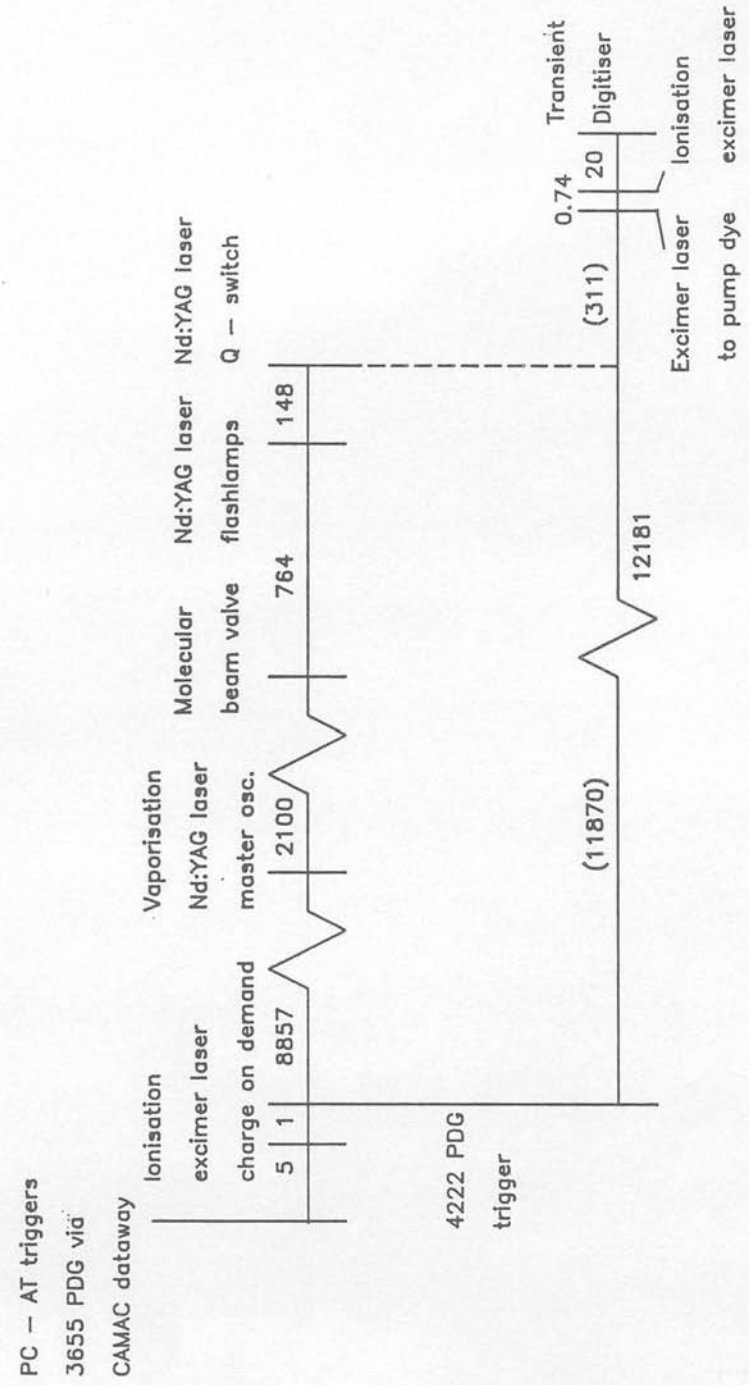

The first function (TIC, see code 3.2) armed the TD, loaded the time delays into the PDGs and triggered the first PDG. The target rod was moved depending on how many shots were to be taken at each position of the rod, normally 1. Once the TIC function completed the processor returned to execution of the task underway when the timer interrupted. By having the TIC routine running *in background* like this a constant repetition rate was maintained irrespective of what the computer was doing. A typical example of the time delay sequence initiated by TIC is shown in figure 3.2.

When accumulation of mass spectra was required the second function (TOC, see code 3.3) was executed on alternate interrupts to retrieve the stored data from the TD and the ADC. This function downloaded the digitised waveform from the TD, using DMA, into a temporary buffer in the PC - AT. The channels of the ADC in use were read into an array. The raw data in the buffer then underwent limited processing to invert it (the MCP signal was negative) and sum it with the previously acquired shots. Each shot processed by TOC was recorded and a marker plotted on the screen to show how many shots had been accumulated.

3.2.2 Time of flight mode

In time of flight (TOF) mode the recorded mass spectra were displayed on the screen of the PC - AT. A loop was created in the program to provide a continuous data capture and display cycle. Code 3.4 demonstrates how this was programmed. A flag (*TDSTART*) signalled the TIC function to set another flag (*TOCGO*) which caused the TOC function to collect and store data.

Code 3.4
Section of program used to record & display TOFMS

```
do{
  TDSUM=0; /* discard previously stored data */
  sumshots=0; /* reset data shot counter */
  do{
    TDSTART=1; /* start data collection see TIC function */
    while(TDDONE){}; /* wait for 1st shot, TOC sets TDDONE = 0 */
    while(!TDDONE){};
     /* wait for data collection to finish - see text */
    tdplt(); /* plot time of arrival profile on screen */
    if(kbhit()){c=lower(getch());keyhandler(c);}
     /* check if any entry made at keyboard */
  }while(sumshots<shots2sum && c!=27);
   /* loop till total number of shots summed */
}while(c!=27) /* keep going till <esc> is pressed */
```

A preset number of mass spectra were recorded and summed by TOC (see above), after which acquisition halted to allow display of the data on the screen. Two variables were used by the program to halt data acquisition. The first variable (*nshots*) determined the number of shots between data display cycles and the second variable (*shots2sum*) determined the total number of shots to be accumulated. Both of these variables could be altered while an experiment was in progress to allow different numbers of shots to be summed for different levels of signal to noise. After the total *shots2sum* was reached the program either waited or cycled back to collect another set. During the data display TOC did not execute so that the data remained in a 'stable' state while it was plotted. TIC continued to execute to maintain the stability of the laser output.

The program, as it was used for the current work could process at most 2048 (2 K) channels of TD data per shot at a 10 Hz repetition rate (see section 3.4). At the highest resolution of the digitiser (10 ns / sample) this meant that only 20.48 µs of the ion time of arrival profile was recorded. Only when individual isotopomers of the clusters had to be resolved was this required, otherwise a slower digitising rate was used to record more of the mass spectrum. To fully resolve clusters with flight times greater than 20.48 µs an appropriate delay was inserted between the ionisation laser and the TD trigger so that the relevant portion of the MCP signal was recorded. The maximum resolvable mass was dependant on the factors discussed in the previous chapter, and also the digitising rate used to record the MCP signal. The slower the sampling rate the lower the resolution. It was even possible for the digitiser to totally miss an ion signal if it fell between two sample times. The TD sample window was 3 ns which meant

that even at the highest digitising speed it could miss the peak of a signal and sample only the wings making it appear much weaker than the true intensity. To reliably record a peak shape at least four samples were required. This placed a lower limit of 40 ns on the width of the ion signals from the detector. This will become a major limit on the resolution of the TOFMS at higher masses where the adjacent peaks are closer together.

The mass spectra were calibrated by fitting known mass peaks to their time of arrival at the MCP by a least mean squares fit to the classical formula for kinetic energy (see chapter 4). The coefficients of this fit were used to scale the X-axis in mass and to determine the mass corresponding to unidentified peaks.

3.2.3 Integration of ion signals for performing spectroscopy

The TOF mode was the basic 'building block' of the program and was used in the investigation of the overall cluster distributions described in the following chapter. To carry out time resolved and spectroscopic studies of the metal clusters, the area under the relevant ion peak in the TOF spectrum was integrated by summing the TD channels comprising the peak, e.g. if the $^{63}Cu_2$ dimer peak was recorded in channels 500 - 505 then a signal was defined as starting at channel 500 and continuing through the following 5 channels. Another signal could be defined as a background signal to be subtracted from the integrated mass signal on a shot - to - shot basis. The average of the latter signal was subtracted from the average of the integrated mass peak. This facility removed any noise due to variations in the baseline current by measuring the size of the peak relative to the recorded baseline rather than the digitiser zero level.

This method was only of use where the ion signal as well as the baseline was affected by the variation such as might occur with an unstable electrical ground. Up to 10 of these signals could be defined at any one time, allowing all the isotopomers of a metal dimer to be recorded simultaneously. The use of these signals in time resolved and spectroscopic investigations is described in sections 3.2.5 and 3.2.6.

3.2.4 Implementation of the routines to control the time delays

The time delays between events were controlled from the PC - AT by the two PDGs. A typical timing setup for an R2PI experiment is shown in figure 3.2, the delay for the TD relative to the ionisation laser trigger was increased to record ions with long flight times (in this case $>$ 20 µs) at the maximum resolution of the digitiser. The time delays required were entered from a menu and stored in an array which was used by the TIC function to program the PDGs.

The time delays were initially set up by estimating the expected delay required between different events, e.g. nozzle firing and photoionisation laser firing. Optimisation of the time delays was carried out using the function keys on the keyboard which were mapped to the channels of the PDGs, whilst monitoring the TOF spectrum. The function keys changed the time delays by a fixed amount per keypress. The magnitude and direction of the change was altered via another of the menu options. The function called by these keystrokes checked that the proposed change was within the range of the PDG before carrying it out.

Figure 3.3 The different modes implemented for linking of the time delays

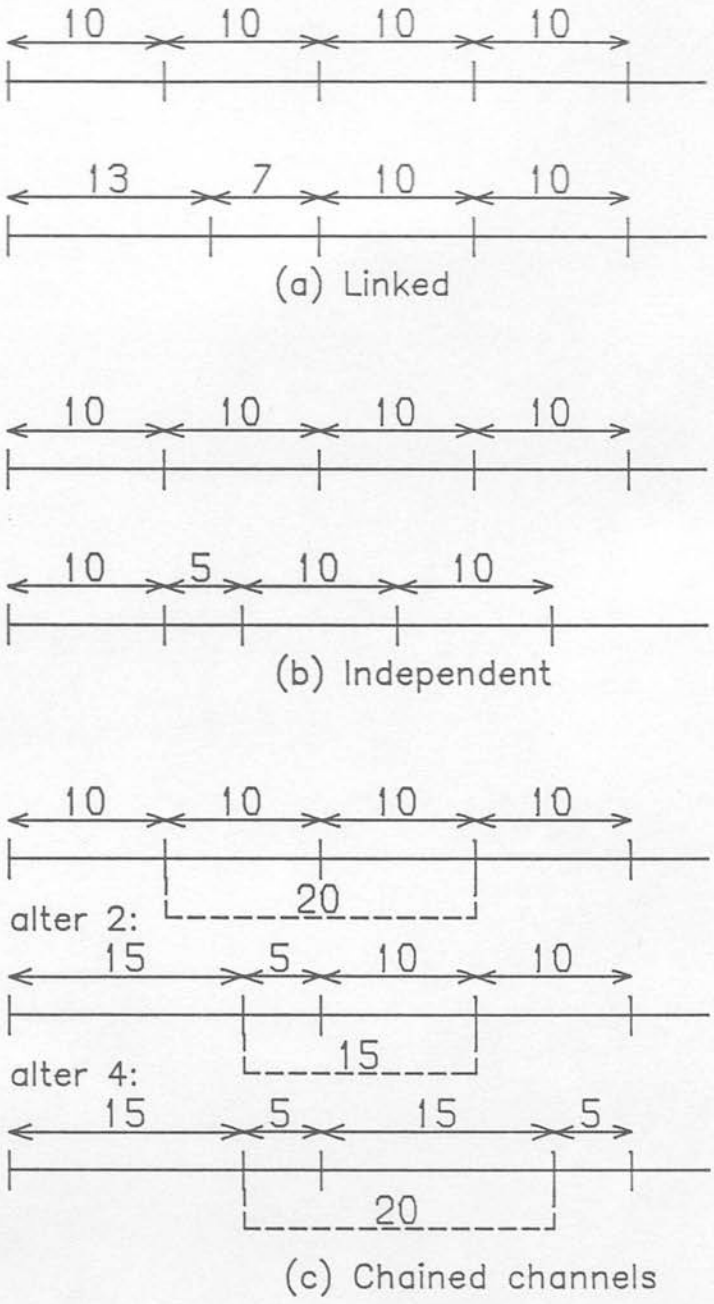

Two modes of changing the time delays were implemented; the *linked* mode and the *independent* mode. When a delay between two pulses was changed in the *linked* mode then the following delay changed by an equal and opposite amount (see figure 3.3(a)). The *independent* mode changed only the delay in the required channel, all the other delays remaining fixed (see figure 3.3(b)), thus changing the delay between all succeeding channels and all preceding channels. A facility was provided for linking together two non - adjacent channels so that when the delay of the later one was changed the earlier one changed by the same amount so that the time delay between them remained fixed (see figure 3.3(c)).

3.2.5 Timescan mode

An advantage of having an integrated data system was that the computer could synchronously change the delay time between events whilst monitoring the effect this had on the ion signals. This simplified optimisation of the time delays and allowed time resolved studies to be accomplished. Ion signals were integrated as described in section 3.2.2 with the time delay in a predetermined channel being stepped after each shot. The size of the step was preset using the timing setup menu option before starting a scan. Limits were set for the range to scan the delay, the range and step size had to amount to less than 256 steps. The ion signals were integrated and stored every shot with the average signal for one of the channels being plotted on the screen by the TIC function. The format used for the storage of the data during timescans is given in appendix B. With weak or noisy signals it was necessary to scan over the delay range several times,

summing the signal at each delay to build up a clear profile such as that shown in figure 2.3. The standard deviation of the recorded intensity of each individual ion signal was calculated and stored at every time delay throughout the scan range. A vertical bar of appropriate size relative to the standard deviation was plotted through each data point to give an estimate of the cluster stability at the different time delays.

In two colour experiments excited state lifetimes were measured by scanning the delay between the excitation and ionisation lasers, while the excitation laser remained tuned to a rovibronic transition. Potentially this mode could be used to determine the lifetimes of individual rotational levels, though in the present work any time resolved studies were accomplished by tuning to the most intense feature, usually a band head (see chapter 6).

3.2.6 Frequency scan mode

Spectroscopic investigations of the metal clusters in the beam were carried out using the R2PI technique described in the previous chapter. The PC - AT accumulated mass spectra as for the TOF mode (section 3.2.2). After a set number of shots (*shots2sum*) had been accumulated the relevant ion signals were integrated, stored (see appendix B), and displayed, before stepping the dye laser to the next wavelength. The wavelength tuning of the 3002EC dye laser (see section 2.5.3) was synchronised to the rest of the experiment by a trigger pulse generated by stepping the voltage of one of the DAC channels. By controlling the tuning of the dye laser the computer ensured that all recorded data shots during one cycle were taken with the laser tuned to a fixed wavelength

and not while the grating (or etalon) was moving. The fringes from the monitor etalon (see section 2.5.3) were recorded concurrently using a photodiode, the output of which was sampled by a sample and hold circuit, captured by the ADC and stored along with the ion signals to provide a relative wavelength calibration.

The frequency scan continued until halted by the operator, the end of the scan range was reached, or the memory allocation was filled up. The spectrum acquired was then stored to disk, and either a new scan started, or the previous one continued from the point at which it was halted. This allowed scans over very long wavelength ranges to be carried out. The limit on the wavelength range which could be covered in a single scan depended on the size of the step and the number of signals being recorded. This is discussed further in appendix B.

The display during a frequency scan could be either the mass spectrum, or a plot of the intensity of one of the predefined signals against the laser wavelength. These two options were toggled by one of the menu options, as was the choice of the signal displayed.

3.2.7 Power normalisation

Shot to shot power normalisation of the ion signal was done by monitoring the pulse energy of the lasers by directing part of the beam onto fast photodiodes. The output of the photodiodes was recorded by the ADC via a sample and hold circuit, and used to correct the ion signal for fluctuations in the laser power. The photodiodes were calibrated by averaging 100 shots before the start of a scan. This value was used to scale the normalisation factor:

normal = 16384*avpow/thispow

Where *avpow* was the average ADC reading taken before the scan, and *thispow* was the ADC reading of the shot just recorded. The multiplication by 16 K served to avoid a loss of precision when the value was truncated to an integer. The normalisation was carried out by an assembler routine called from TOC (*tddump*). The raw data from the digitiser was loaded into the ax register of the processor and left shifted by two bits (≡ multiplication by 4) before being multiplied by *normal* to get the corrected data. The corrected value required division by 64 K which was accomplished by storing only the part of the result of the multiplication which had overflowed into the dx register, this being equivalent to dividing the number stored in the ax and dx registers by 64 K. This method of normalisation avoided any divisions or floating point arithmetic, both of which were time consuming operations to perform on the 80286 processor. The 80287 maths co - processor was not used to perform the normalisation as it was found that the extra instructions required to transfer the data to and from it used more time than the above method.

This power normalisation could be carried out for 1 colour - 1 photon, 1 colour - 2 photon, or 2 colour - 2 photon processes, determined by the value of the flag *POWOPT* in TOC (see code 3.3).

3.2.8 Data display

The plotting of the data in TOF mode, though not proceeding until data collection has been halted nevertheless needs to be completed rapidly to avoid

excessive dead time and lost laser shots between data acquisition cycles. The plotting functions made use of two features which were designed as part of the software. The first was to draw the axes on the screen at the start of a data collection run and store them in the main system RAM for recall when the screen was redrawn. This feature could be turned off to provide automatic scaling of each new plot when the signal was widely varying in intensity each time it was plotted (e.g. when the total rather than the average signal was displayed). The difference in time between recalling the blank axes from memory (*auto* = off) and redrawing them (*auto* = on) is shown in table 3.1. The only disadvantage of this procedure was the amount of memory required, as storing a 640 x 350 pixel colour screen took 128 Kb.

The other feature combined customised line drawing and point plotting functions. The line drawing function was based on the *STL* function in reference [2]. This required modification to work with the EGA by setting the bh register of the 80286 to the graphics page (0 or 1) in use before calling the BIOS point plotting routine (INT 10h [3]). The alternative point plotting function developed, though not having all the functionality of the BIOS software interrupt call, took half the time to plot a point on the screen (see table 3.1). This meant ~10 shots were lost whilst the data was plotted compared to ~20 when using the BIOS interrupt.

Code 3.5 - Fast point plotting function for EGA

```
;*****************************************************************
; A fast point plotting routine for the IBM EGA. (~ 2x EGA BIOS).
; Call by 'call _pltp' with ax, cx, & dx set as for INT 10h ah=12
;*****************************************************************
.286C
.8087
asm_text        segment byte    public  'code'

        assume cs:asm_text
        public  _pltp


EYTY    dw      80


_pltp   proc    far
        push    bx
        push    cx
        push    dx
        push    es
        push    ax          ;colour
        push    dx          ;Y
        push    cx          ;X
        mov     ax,0A800h   ;set es to graphics page 1
        mov     es,ax       ;(page 0=0A000h)
        pop     ax          ;ax=X
        ror     ax,3        ;al = abs(x/8), ah=remainder
        mov     ch,80h      ;ch=10000000b
        cmp     ah,0
        je      ZERO
        shr     ah,5
        mov     cl,ah       ;cl=bit posn of x
        ror     ch,cl       ;rotate ch to make mask for xstart
        mov     ah,0        ;blank ah
ZERO:
        mov     bx,ax       ;bx=byte of x in line, bit in ch
        pop     ax          ;ax=Y
        mul     EYTY        ;ax=Y*80  (80 bytes/row)
        add     bx,ax       ;bx=video ram byte containing pel
        mov     dx,03CEh    ;set Bit mask Reg so only 1 bit is
        mov     ah,ch       ;changed
        mov     al,08h
        out     dx,ax
        mov     al,es:[bx] ;read byte
        mov     dx,03C4h    ;set dx=03C4h for map mask reg of EGA
        mov     ax,0F02h    ;blank byte
        out     dx,ax
        mov     es:[bx],byte ptr 0
        pop     ax          ;ax=color
        mov     ah,al
```

```
        mov     al,2        ;al=2
        out     dx,ax       ;set colour mask reg.
        mov     es:[bx],ch  ;set pixel!!!!    DO_IT!!!!
        mov     ax,0F02h    ;turn all planes on
        out     dx,ax
        mov     dx,03CEh    ;turn all bytes on
        mov     ax,0FF08h
        out     dx,ax
        pop     es
        pop     dx
        pop     cx
        pop     bx
        ret
_pltp   endp
asm_text        ends
        end
```

The point plotting function was written in assembler, and is given in code 3.5, the data could have been plotted in the dead time between shots, but this would have given a distorted representation of the signal due to the points plotted later being the sum of a greater number of data shots.

3.2.9 Timing jitter

A major problem when performing R2PI experiments with the excimer pumped dye laser system was the temporal jitter in the output. In one colour experiments any fluctuation in the time at which the light pulse caused ionisation changed the channels of the TD in which the ion signals were recorded, by altering the time between ionisation and the TD stop trigger. One way round this problem was to trigger the TD from a photodiode monitoring the light pulse, but this was not feasible when the TD needed to be delayed with respect to the ionisation laser. In the current work the change in the TD channels was monitored by displaying the mass spectrum during wavelength tuning and observing the recorded time of arrival of the ions relative to the stop trigger of the TD (i.e. the channel(s) in which the signal was digitised). The time delay of the laser relative to the TD was adjusted using the function keys to keep the ion signal in the same channels in the digitiser.

In two colour experiments the jitter between the two lasers was monitored by two photodiodes using an oscilloscope. The time delay being adjusted as before to maintain the temporal overlap of the two pulses. Another way round this problem would be to use a time to digital converter (TDC) triggered off photodiodes monitoring the two laser pulses. The first laser pulse would trigger

the TDC which would continue counting until stopped by the second pulse. The computer could then discard those shots where the time between the two pulses was outwith a given range, and correct the appropriate time delay to bring the two lasers back into synchronisation.

3.2.10 Other facilities in THOR

The program contained other facilities required to tailor it to individual uses. The time of arrival profile was displayed either as the total ion signal or the average of the number of shots summed. There was a facility for obtaining 'snapshots' of the screen for output to the line printer. The stored spectra were able to be reloaded for inspection, calibration, and output to the plotter.

In addition to storing the data the program also stored all the experimental settings that were controlled from the computer. These included the time delays, signal definitions, calibration factors for the mass spectra, and the dye laser parameters. These settings were able to be stored separately, without all the data, in configuration files. The default configuration file (THOR.CON) was automatically loaded as the program started up. These files allow a previously optimised set of parameters to be quickly and easily recalled and reset, to facilitate rapid changes from one configuration to another (e.g. from single laser ionisation to two laser ionisation). Comments could be typed onto the screen and stored with the data, these were used to record other relevant information such as the backing gas, pressure, the nozzle operating characteristics, and the vaporisation laser energy.

3.3 Data analysis on the PC - the ODIN program

The data workup was carried out using a second program, ODIN, developed to use interactive graphics to simplify the task of analysing the data. This program was written entirely in C, except for the line drawing algorithm as used in THOR (see section 3.2.8). ODIN was used to display all the signals recorded during time or wavelength resolved studies, at the same time. Colour coding eased the identification of the different signals.

The most important functions included in ODIN were those for smoothing and finding the peaks in the spectra, using the method developed by Savitzky and Golay [4] [5]. The smoothing routine acted as a filter, removing random noise from the recorded spectrum. This was carried out using the precalculated weighting coefficients from reference [4] to weight a preset number of data points adjacent to and including the one to be 'smoothed'. The average of the sum of the weighted data points was then used as the new 'smoothed' data point. The function worked through the entire data set one point at a time, always using the raw data as input and substituting the smoothed points back into the array once the raw data was no longer required for the smoothing of subsequent data points. Care had to be taken not to include too many points for smoothing or distortion could occur when two adjacent lines in a spectrum became blended into one wide feature. The peak finding routine was used after the approximate position of a peak had been determined to the nearest bin number[1]. Using the Savitzky

[1] Bin is the term used to describe a data point recorded during a wavelength scan.

and Golay routine it was possible to interpolate the exact centre of a peak to within $1/10^{th}$ of a bin.

The etalon fringes, recorded as a relative wavelength calibration, were also processed using the peak finding routine and the positions found used in a least mean squares fit [6] to the free spectral range of the etalon to give the coefficients of a polynomial function used for converting the separation of the peaks in the R2PI spectra from bin numbers to wavenumbers. The peak positions were then used as described in chapters 5 and 6 to obtain the spectroscopic constants for the species being studied.

3.3.1 Other facilities in ODIN

ODIN contained many other functions for manipulating the data and for outputting it to disk, printer, and plotter in various formats. The peak positions in the R2PI spectra and associated coefficients from the etalon fringes were output to ASCII files for transfer to the mainframe and subsequent analysis, as described in chapters 5 and 6. The data signals were able to be added, subtracted, multiplied and divided by a constant or data from another signal. These functions, along with exponentiation, allowed average power normalisation and background subtraction to be carried out on the stored spectra.

3.4 Performance of the PC - AT / CAMAC system and associated software

A comprehensive investigation of the throughput of the data system was undertaken. This arose from the need to determine the amount of data the

computer could process per shot. Initially this was done by simply increasing the repetition rate and the number of digitiser channels until the computer crashed. This was not a particularly satisfactory situation as it gave no quantifiable results upon which further development could be based.

To obtain such information, the overall performance of the data system, in terms of the amount of data processed per shot, was measured using routines written into THOR. The key functions involved in the acquisition and processing of the time of flight signals were timed by averaging 500 consecutive executions. The results are summarised in table 3.1. The functions were timed on the original 6 MHz configuration of the PC - AT, and after it was upgraded to run at 8 MHz. In addition, the results of running the software on a substantially more powerful Dell Corporation 310 equipped with a 20 MHz 32 bit 80386 processor and 80387 coprocessor were obtained. The internal clock of the computer was used for timing.

The main use of these measurements was to target which areas of the software and hardware needed improvement to increase the data throughput. This was necessary as to increase the resolution of the digitiser or the mass range recorded would require more points to be processed per shot. There were two ways to do this with the current software and hardware system. Firstly to decrease the repetition rate, and secondly to only acquire data every second or third shot. The disadvantage in both cases was the increase in the time taken to record a spectrum and the consequent need to maintain stable output from the lasers over a longer period of time. The latter method also suffered from the number of experimental shots lost when data was not being acquired, the excess

shots causing unnecessary wear and tear on the lasers and the molecular beam valve. The eventual answer to the problem in the current, or any other system, must be a trade off between the repetition rate and the mass range covered at the highest resolution.

The heart of the software system was the TIC - TOC routine controlled by the timer interrupts. The speed of the TIC and TOC functions determined the data throughput. As shown in table 3.1, the time taken for the TIC function was negligible by comparison with the TOC function. At 10 Hz the time between each data shot was 100 milliseconds, and the time between the timer interrupts used to initiate execution of the TIC and TOC functions was 50 ms. Thus for the 6 MHz PC - AT processing 2 K of digitiser channels, the TOC function was still executing when the TIC function was called to initiate the next experimental shot. This did not present a problem as the data was downloaded from the TD and the ADC early in TOC, before TIC interrupted and reset the TD. However increasing to the next digitiser record length of 4 K meant that the TOC function took longer than 100 ms to complete and was interrupted by the subsequent call to TOC. In this case no call to the TOC function ever completed and the computer locked up.

For this reason the software was developed around a limit of 2 K of digitiser channels per shot. The available memory of the PC - AT was allocated according to this limit so that when the processor speed was increased it was not possible to increase the amount of data processed without a corresponding expansion in the memory beyond the 640K supported by the operating system (IBM DOS 3.0 [7]).

Table 3.1 - IBM PC - AT performance figures (times in milliseconds)

Hardware	6MHz PC - AT		8MHz PC - AT		Dell 310	
No. data points	1024	2048	1024	2048	1024	2048
Function						
TIC	1.10	1.10	0.88	0.88	0.44	0.44
$TOC_{DUMMY\ OFF}$	31.5	58.9	23.4	44.6	9.9	17.66
$TOC_{DUMMY\ ON}$	17.8	33.3	12.4	23.2	3.2	6.0
tddump_c	16.8	33.4	13.0	25.8	6.9	13.9
tddump_asm	9.24	18.56	7.0	13.7	4.9	9.9
tddump_DMA	5.92	11.74	4.8	8.9	4.3	8.5
tddump_DMA*	0.12	0.12	0.10	0.10	0.05	0.05
tdaccum	14.6	29.0	10.0	20.0	2.54	5.2
$tdplt_{auto\ =\ ON}$	2534.5	5064.5	2051.5	3998.5	840.0	857.0
$tdplt_{auto\ =\ OFF}$	1430.5	3716.0	1159.0	2911.0	N/A	N/A
lplot	1071.0	3356.0	813.0	2565.0	N/A	N/A
point_int	0.110	0.110	0.078	0.078	0.054	0.054
point_pltp	0.066	0.066	0.044	0.044	0.022	0.022

* As tddump_DMA but no transfer of data is done. i.e. this was the time required by the tddump_DMA function to set up & close down the DMA.

Notes to table 3.1

TIC initiated an experimental cycle (see code 3.2)

TOC collected, processed & stored the data. The times

shown used *tddump_DMA* to download the data from the digitiser. DUMMY was the flag to use test data & not retrieve data from the TD or ADC.

tddump — were the functions used by TOC to download the data from the digitiser. _c & _asm were written in 'C' & assembler to transfer 1 byte at a time. _DMA was written in 'C' to transfer data using DMA controller of the PC - AT.

tdaccum — was used in TOC to power normalise & sum the data from the digitiser.

tdplt — plotted the time of flight mass spectrum on the screen. The flag *auto* was used to signify whether the Y axis was to by rescaled each time the display was updated. If not the blank axes drawn previously were restored from memory.

lplot — used by *tdplt* to plot the data on the screen.

point_int — plotted a point on the screen using the INT 10h call to the EGA BIOS.

point_pltp — plotted a point on the screen by calling the *pltp* function shown in code 3.5.

The total amount that could potentially be processed each shot, were enough memory available, was calculated by taking the difference in time between 1 K and 2 K of data as the time required for each additional 1 K required. The difference between this time, and the measured time for 1 K, was the time required to perform common tasks irrespective of how much data was being processed. By this method the 8 MHz PC - AT was expected to be able to handle 4 K of data in 87 ms and the Dell 310 12 K in 94 ms.

The time taken by the display function *tdplt* shows why real time display of the data every shot was not considered. The repetition rate would be less than 1 Hz, even the Dell 310 would barely be able to achieve 1 Hz. The majority of the time used by *tdplt* was taken up by the *lplot* function which read the accumulated data from memory, scaled it, checked it was within the range of the display, and plotted it using the *sti* function (see section 3.2.8). This used the maths coprocessor which was shown by other tests carried out to by very slow. When performing the same functions as the main processor the coprocessor took the same time, but due to the extra instructions required to initialise it and send the data to it the overall performance was below that of the main processor. The advantage of the coprocessor was only realised when floating point arithmetic was required, such as when scaling the data for output. The only real solution to the problem of displaying the data on a shot to shot basis would appear to be to use a completely separate graphics processor acting independently of the main processor.

3.4.1 Data rate limits

In the limit of processor speed the bottleneck becomes the rate at which the data can be retrieved from the CAMAC modules. The CAMAC dataway cycle time is 1 μs, a rate of 1 MHz, and this is the theoretical maximum rate which the DMA transfer could possibly achieve. Handshaking between the computer and the crate controller will reduce this, and to go to a higher rate it is necessary to move to a faster dataway standard than CAMAC. The 6002 crate controller has a claimed maximum data transfer rate of 700 Kb s^{-1} in DMA mode. The similar times recorded for the DMA block transfer function (*tddump_DMA*) on the PC - AT operating at 8 MHz and the much faster Dell 310 back this up as described below. The actual rate of DMA transfer was obtained by timing 500 cycles of the DMA transfer of 1024 and 2048 data points, and the corresponding time to perform the same function without any data transfer taking place. This gave rates of 230 Kb s^{-1} for the 8 MHz AT and the Dell 310, and a rate of 172 Kb s^{-1} for the 6 MHz PC - AT. The times for the two PC - AT configurations scale as the processor speed, but the value obtained for the Dell 310 seemed at first to be anomalously low. The reason for the lack of increase in speed was due to the standard 8 MHz speed of the i/o bus in the PC - AT and clones. Thus the 8 MHz PC - AT was driving the bus at its maximum designed speed, and in the Dell 310 the i/o bus was restricted to the same speed. Further evidence for this is gained from the similarity in the times taken for the Dell 310 to perform DMA transfer and word transfer (*tddump_asm*). The similarity in the times of the DMA which bypasses the processor and the word transfer which uses the processor to transfer data, show that it is not the computer which is slowing the

transfer rate, but the CAMAC interface card or controller. The Dell is shown by the other figures presented in table 3.1 to be significantly faster than the PC - AT when performing all other functions other than addressing the CAMAC crate (e.g. *tdaccum* which processes the data once it has been downloaded from the TD). All these facts point to the data transfer limit having been reached for the current system.

The difference between the claimed 700 Kb s^{-1} DMA transfer rate and the 230 Kb s^{-1} rate actually measured was due to the PC004 interface card occupying an 8-bit expansion slot. The 6002 to PC004 transfer took place 24 bits at a time, three times the rate at which transfer took place inside the PC - AT, i.e. for every transfer from the crate 3 transfers were needed to move the data within the computer. The simplest way to enhance the data throughput of the PC - AT system would be to have an interface card capable of 16 bit transfers to the expansion slot of the PC - AT. This would more than double the data transfer rate as the DMA controller in the PC - AT uses more clock cycles to complete the transfer of 8 bit data than 16 bit data [3].

3.5 Conclusion

A flexible data system has been developed which allows control of the molecular beam - time of flight mass spectrometer and associated laser instrumentation. Most of the experimental parameters are controlled from the keyboard of the computer. Optimised configurations can be stored by the computer for rapid and simple recall.

The system is easy to use when running an experiment. Progression from simple non - resonant mass spectroscopic studies of the species in the beam to power normalised, calibrated, two colour spectroscopic studies is relatively easy.

The system is capable of monitoring up to ten separate signals simultaneously, providing a great saving in cost and complexity over other methods, e.g. multi channel boxcars and chart recorders.

The use of CAMAC as the instrument standard allows the integration of new instruments as and when they are required. This is achieved with the minimum amount of extra programming as all the necessary interfacing is already in place. This allows expansion of the system for other uses, and it has already proved invaluable in the optimisation of a second time of flight - molecular beam apparatus in the same laboratory.

3.5.1 Future Expansion

Future development of this type of data system must involve some degree of parallel processing. This could be in the form of one additional processor to handle the graphics or a multi processor system for handling large quantities of TD data.

Preliminary testing of an Inmos T800 floating point transputer hosted by the PC - AT was carried out and the results were encouraging. Comparison with the 8 MHz PC - AT showed the T800 to be around 34 times faster for numeric processing. However any process requiring use of the PC - AT for input or output was much slower than the PC - AT, presumably due to the server

program run on the PC - AT, and the need to transfer data via the i/o bus of the PC - AT. For this reason the speed of the T800 will only be of use if the data can be transferred directly from the memory of the TD. A data transfer rate of 2 Mb s^{-1} is claimed for transfer over the Inmos link used to communicate between transputers [8], so a CAMAC crate mounted transputer with access to the TD memory would provide a significant increase in the performance. The overall throughput has been estimated in the region of 96 Kb per shot for a 10 Hz repetition rate for a single transputer hosted by a PC. The potential of the transputer as a processor is its ability to work in parallel with other transputer chips. The TOF signal is ideally suited to processing in this manner as each element is processed individually without reference to any of the other digitised points. The use of a parallel processing system such as an array of transputers, connected directly to the TD and a display could give real time display with each shot displayed as it is recorded.

References

[1] Costrell L., IEEE Trans. Nuc. Sci., **20**, p 557, (1973)

[2] Morgan C.L., *The Bluebook of Assembly Routines for the IBM PC and XT*, McGraw - Hill, 1983.

[3] IBM Corporation, *IBM Technical Reference, Personal Computer AT, part No. 1502494*, IBM, Boca Raton, Florida, 1984.

[4] Savitzky A., Golay M.J.E., Anal. Chem., **36**, p 1627, (1964)

[5] Steiner J., Termonia Y., Deltour J., Anal. Chem., **44**, p 1906, (1972)

[6] Bevington P.R., *Data Reduction and Error Analysis for the Physical Sciences*, McGraw - Hill, New York, 1969.

[7] IBM corporation, *DOS V 3.00 , part No. 6322666*, IBM, Boca Raton, Florida, 1984.

[8] Davidson M., *Inmos Ltd.*, Private Communication,

Chapter 4
Mass Spectroscopic Studies of Transition Metal Clusters

4.1 Introduction

Mass spectrometric measurements have been used previously as a means of investigating the structure of naked metal clusters, initially for measuring dissociation energies of dimers produced using Knudsen cell techniques [1]. They have also found application in reactive studies of these species. This chapter serves to outline some of this work, to present some of the simple observations recorded with the current instrumentation, and to point to areas in which it could be used in the future. As mass spectroscopic studies were not the prime objective of this project an exhaustive investigation was not undertaken. However it is worth recording some of the more salient features of the mass spectra recorded and the methods used in their optimisation for the spectroscopic studies described in the following chapters.

Mass spectra were recorded for a number of transition metals during the current work, using two different pulsed beam valve sources and two different Nd:YAG lasers for vaporisation. The beam valves used were the NRC BV-100 described in chapter 2 and a General Valve Corporation series 9 flange mount pulsed beam valve. The latter had only a single solenoid coil, which was used to open the valve and relied on the pressure of a spring to close it. The two lasers employed for vaporisation were the Quanta - Ray DCR II/A, described in chapter 2 and a JK HY750. In both cases the output was frequency doubled to

532 nm before use. The JK laser had the disadvantage that the output pulse energy was not as easily controlled, due to the Q - switch delay being fixed. Neutral density filters placed in the beam before the lens used to focus the beam onto the target rod, or alteration of the charging voltage for the flashlamp capacitor bank were used to adjust the pulse energy of this laser. Ionisation of the clusters was accomplished in all cases with the 193 nm (6.4 eV) output of an ArF excimer laser.

The laser vaporisation technique lends itself to studies of even the most refractory of materials such as tungsten (b.p. 5800 K) [2]. Heteronuclear mixed metal clusters can also be studied by using target rods comprising alloys of the elements of interest, or by the addition of a suitable gaseous precursor, such as $Fe(CO)_5$, to the buffer gas [5]. Successful studies of this type have been carried out by a number of groups on Ni / Cr and Ni / Al [3], and Bi / Cr and Mn / Ag [4].

The time of flight mass spectrometer is ideal for recording the cluster distributions from a pulsed source such as the present one, the pulsed laser used for ionisation removing the need for gated extraction fields in the TOFMS. The only disadvantage encountered was the strong mass dependence of the transmission function of the TOFMS. This produced the *window* effect apparent in mass spectra extending over a large mass range, and was due to the perpendicular geometry adopted for the TOFMS with respect to the molecular beam axis. A constant voltage was applied across the deflection plates to steer the ions along the drift tube and could therefore compensate for only a limited range of m/e values in the direction of the beam at any one time. Compensation

for m/e values outwith this range was either too great or too little and resulted in only partial transmission with many of the ions missing the detector or colliding with the walls of the drift tube. This limited range was not a particular problem for the main purpose of the equipment in studies of the spectroscopy of the metal dimers, as the mass range required was only a few a.m.u. The perpendicular geometry was adopted to enable the spectroscopic laser to be aligned coaxial with the molecular beam, an arrangement not utilised for the work presented in the following chapters. The acquisition of a complete mass spectrum every shot allowed qualitative assessment of the cluster distribution under a particular set of experimental conditions. The time of flight data processing mode described in the previous chapter was used during optimisation of conditions in the cluster source and the mass spectrometer.

4.2 Optimisation of conditions and calibration of mass spectra

4.2.1 Optimisation of the cluster source

The cluster source had five adjustable parameters aside from the choice of target material. These were backing pressure, pulse duration, cluster channel length and diameter, vaporisation laser energy, and focus position. The first two were set at the maximum possible values (10 bar He and 900 μs duration) for most of the work to obtain the maximum possible cooling during the supersonic expansion and ensure the vaporised metal was fully entrained. The length and diameter of the cluster channel was observed to have a profound effect on the cluster distribution, short lengths or large diameters, or the cluster faceplate

alone gave if any a very truncated cluster distribution with a predominance of the atom. This was due to an insufficient integration time being allowed for quenching of the plasma and condensation to occur. Long channel lengths tended to stretch out the pulse of metal clusters produced by vaporisation and reduce the peak concentration in the beam. When using a diameter of 1.5 mm, a length of 40 mm from the point of vaporisation was found to be optimum for small ($n \leq \simeq 30$) clusters of copper and silver. The largest effect on the cluster distribution was produced by the vaporisation laser pulse energy and the size of the focal spot. This was found to be heavily dependant on the target material, with reoptimisation required to obtain the most intense cluster signal for different metals. The cluster signals were maximised by monitoring the time of arrival profile displayed on the screen of the PC - AT whilst adjusting the backing pressure, pulse duration, and vaporisation laser energy or focus. For the work on copper and silver dimer in chapters 5 and 6 the following pulse energies and positions of the 1 m focusing lens were used:

Cu: 22 mJ/pulse, lens 102 cm from target rod

Ag: 17 mJ/pulse, lens 95 cm from target rod

The target rod required minimal preparation other than cleaning the surface with abrasive cloth and solvent. The surface was found to be more efficiently cleaned by using the vaporisation laser to remove material under vacuum in the cluster source, under normal experimental conditions. If the surface appeared heavily contaminated the laser power was increased to speed the cleaning process. The removal of surface contaminants in this fashion was monitored as a

reduction in the carbon and 'CH' species in the mass spectrum. This cleaning process ensured that most of the oxides and other surface contaminants were removed, and the cluster signal usually increased markedly after this as only metal and no other species was absorbing the vaporisation laser energy.

4.2.2 Optimisation of the TOFMS

The only adjustable parameters in the time of flight mass spectrometer were the deflection field and the voltage applied to the detector. The voltages applied to the ion extraction optics were fixed by the geometry of the TOFMS as described in chapter 2. The dual Micro Channel Plate (MCP) detector had a gain of 10^3 per plate giving a total gain of 10^6 when 1 KV was applied across each plate, the output being further amplified and recorded as described in chapter 3. The effect of the voltage applied to the deflection plates has been discussed above. Figures 4.2 - 4.5 illustrate the *windowing* caused by the limited mass independent range of the transmission function, with clusters to the low and high mass ends of the spectrum displaying reduced intensity. Typical operating voltages for copper dimer were:

V_{DEFL} = 270 V.

V_{DET} = 3600 V. (≡ 730 V / plate)

The lighter helium ion required only 30 volts across the deflection plates for maximum signal.

The photoionisation laser required optimisation by narrowing the beam in

the direction of the drift tube with a pair of razor blades to reduce the initial spatial spread of ions formed. Narrowing the laser beam also served to sample only the coldest central part of the molecular beam, once the height of the slit had been adjusted to coincide with the axis of the beam. By sampling only the coldest part of the beam the initial velocity spread was reduced (see section 2.4).

The mass spectra recorded during the present work were, of necessity, a tradeoff between resolution and range, due to the limited number of data points processed per shot (see chapter 3). At the maximum 100 MHz digitising rate the 2048 samples recorded covered a range of ~300 a.m.u. At slower digitising rates the mass range covered was extended, but at the expense of resolution. When large ranges were recorded the limited mass range of the transmission function of the TOFMS caused a drop in the recorded intensity of masses, outwith the range for which the field across the deflection plates was optimum (see section 4.1). At the maximum digitising speed different portions of the MCP output were selected by delaying the digitiser relative to the time of ionisation. An example of a spectrum recorded is shown in figure 4.1. This shows the copper atom, dimer, and trimer; the leftmost two peaks are due to Al and AlC present in the beam. The presence of the aluminium is due to the vaporisation laser striking the cluster source as well as the copper target rod, and the AlC probably arises from reaction of the atom with residual carbon from fragmented pump oil present in the cluster source. Ideally, striking the faceplate with the vaporisation laser was best avoided as it could cause the rod to stick in the faceplate. When this happened the laser etched a deep hole in the surface of the

rod and the cluster intensity rapidly declined (see chapter 2). The mass spectrum of copper clusters presented in figure 4.1 was recorded with a relatively small voltage applied to the deflection plates (280 volts) whereas that in figure 4.2 was recorded with 450 volts applied to the deflection plates. The loss of resolution with increasing mass is clearly evident in figure 4.2, and is due to the decreasing gap between the arrival times of the ion packets corresponding to heavier masses.

4.2.3 Calibration of the mass spectra

Calibration of the mass spectra was achieved by fitting the time of arrival of ions of known mass to the classical equation for kinetic energy:

$$U = 0.5 \times m \times (D/t)^2$$

$$\Rightarrow t = [\, m / (2U) \,]^{1/2} \times D$$

Where:

U = total kinetic energy

t = time of arrival

D = length of drift tube

m = mass of ion

$[D / (2U)^{1/2}]$ is a constant obtained from the least mean squares fit.

This is the exact solution to the amount of time spent by individual ions in the field free drift tube. However the time spent by the ions in the source region and second stage (DOG - ground) of the TOFMS must be included to achieve an accurate calibration of the X - axis of the time of flight spectra.

Figure 4.1
Mass spectrum of Cu_{1-3}

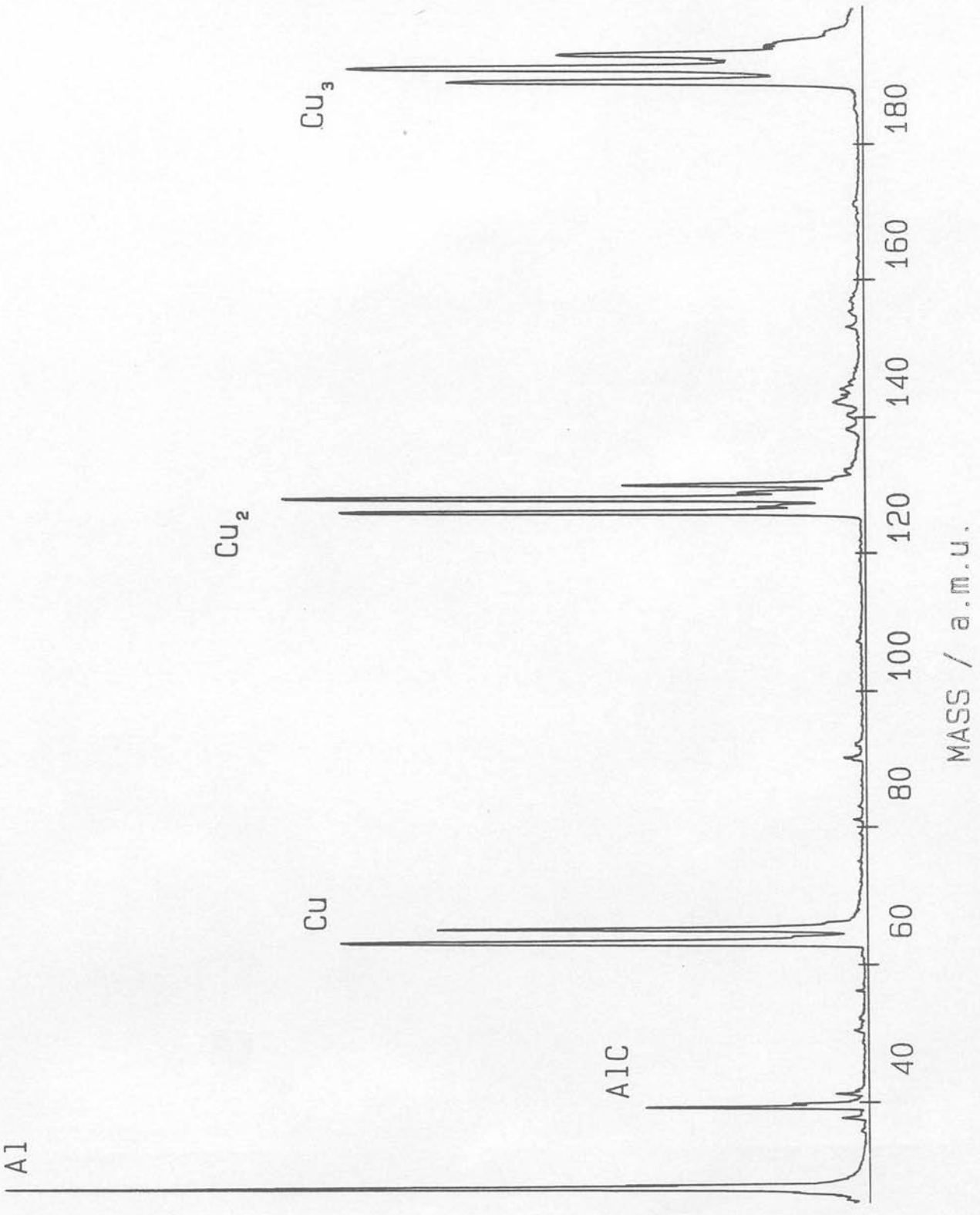

Figure 4.2
Mass spectrum of Cu_{1-36} showing *magic number* clusters

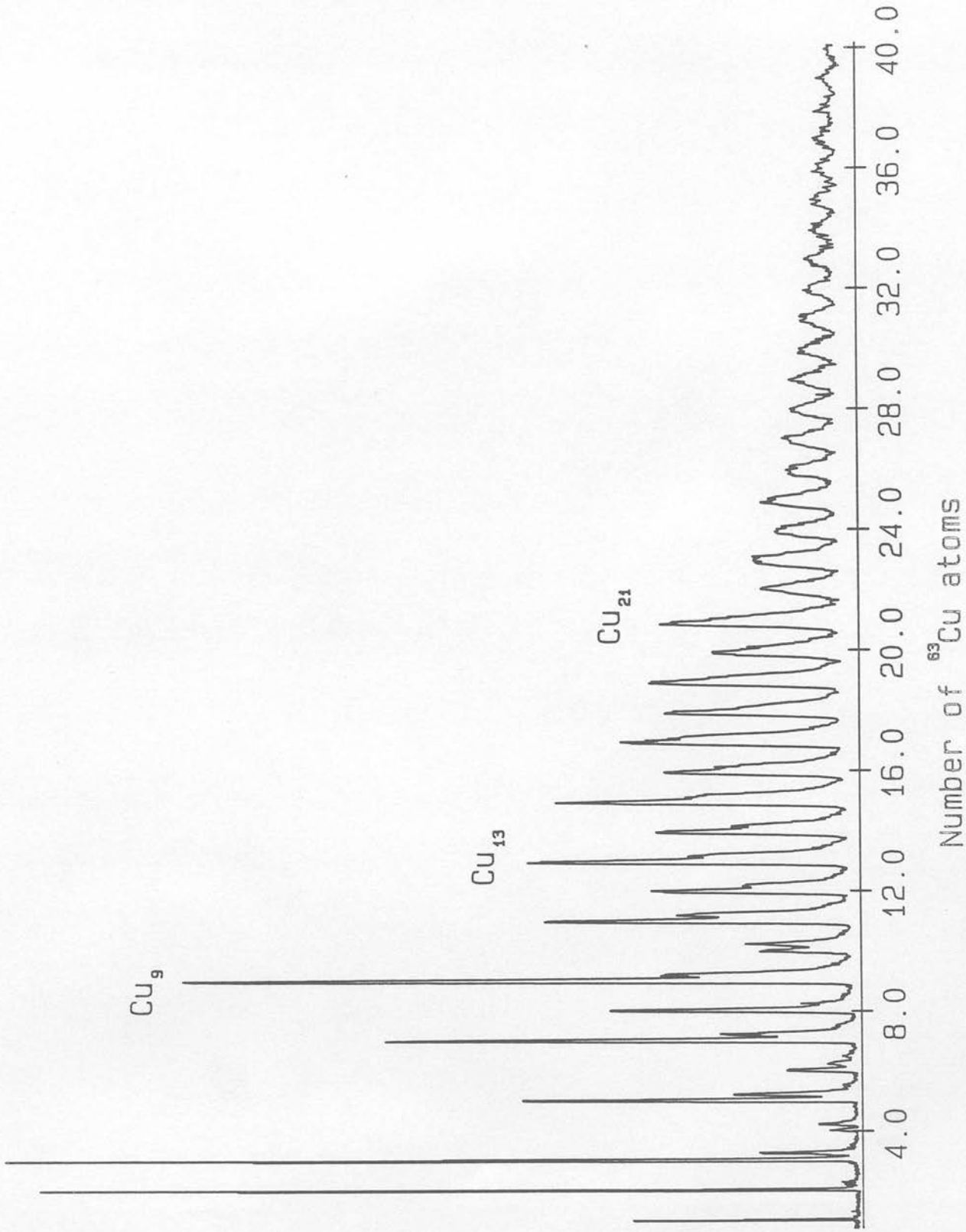

From the equations of Wiley and McLaren [10] it can be shown that the time spent by the ions in the two parts of the source region, and therefore the total flight time, varies as $m^{1/2}$.

$$T_F = T_s + T_d + T_D$$
$$= C_s m^{1/2} + C_d m^{1/2} + [m / (2U)]^{1/2} \times D$$

where:

T_F = total flight time

$T_{s/d/D}$ = time spent in source / 2nd stage / drift tube

$C_{s/d}$ = constant α strength of applied field

This allowed the time of arrival of the ions to be fitted to the mass by the following function:

$$t = a + bm^{1/2}$$

By fitting the digitiser channel number ($\equiv$ t) in which the peak intensity, for each ion, was recorded and the square root of the mass by a least mean squares method, the coefficients a and b were obtained. The second coefficient is equal to the sum $C_s + C_d + [D /(2U)^{1/2}]$. These coefficients were used to scale the X - axis in mass units, or number of atoms of a given mass in each cluster.

4.3 Features of the recorded mass spectra

The cluster intensity distribution was expected to decrease more or less monotonically with increasing cluster size due to the clustering process relying on the number of collisions undergone in the cluster source [5]. Factors affecting the observed cluster distribution, other than the drift tube transmission function described above, are described below.

The field applied across the deflection plates was optimised for detection of Cu_7 in the spectrum shown in figure 4.2. The strong dimer and trimer signals are due to the high concentration of these species in the beam. The discontinuities in the intensity distribution occurring at Cu_9 and Cu_{21} can be explained using the *jellium* model for metal clusters [7]. In this model the cluster is treated as a spherical drop, with the molecular orbitals formed from the atomic valence orbitals mimicking the atomic orbitals of hydrogen. Thus the Cu_9^+ and Cu_{21}^+ ions correspond to 8 and 20 electron 'closed shell' species [6] [8]. The observed increase in the intensity of these two clusters is therefore due to the stability of the ion formed, removal of the electron from the neutral being more facile than for neighbouring clusters.

Cu_{13} also appears with greater intensity than its neighbours in the mass spectrum. However, this is believed to be an artefact of the highly stable closed icosahedron formed, with the 13^{th} atom enclosed in the centre [3]. Clusters containing 13 atoms appear with enhanced intensity for many metals, not just those of group 1B. The mass spectrum of iron clusters shown in figure 4.3 exhibits the same behaviour.

Figure 4.3
Mass spectrum of Fe_{1-28} showing the effect of the drift tube transmission function, and the enhanced intensity of 13 atom clusters

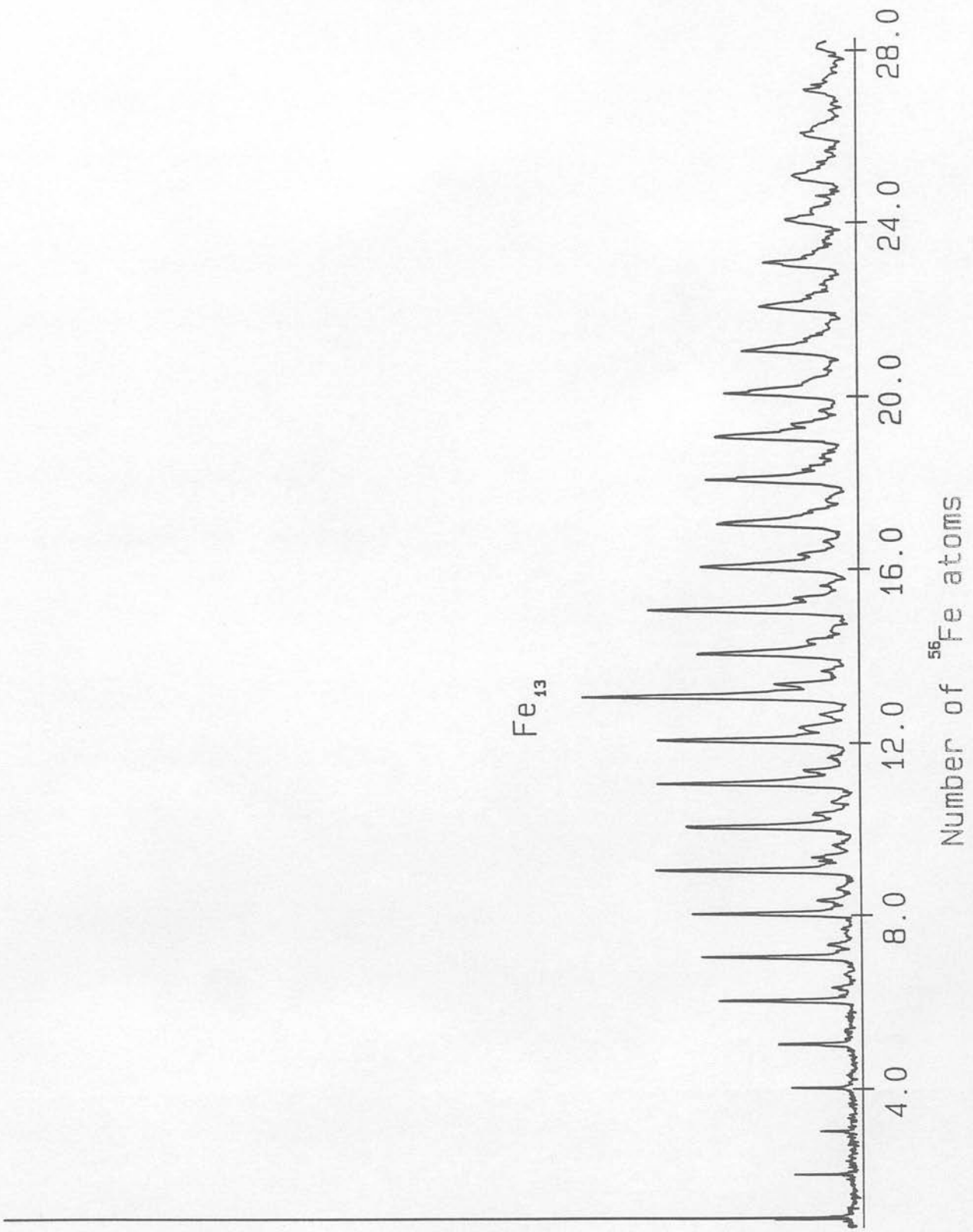

These are two examples of *magic number* clusters which appear with enhanced intensity relative to their neighbours in elemental mass spectra of both the transition and main group elements.

4.4 The determination of cluster ionisation potentials

Although all the work carried out in the present investigation used an ArF laser to carry out photoionisation, other workers have previously used different fixed frequency lasers to probe the gross electronic structure of the naked metal clusters. These studies were aimed at determining the variation in ionisation potential as a function of cluster size. Rohlfing et. al. [9] in an extensive study of clusters of iron, using four fixed frequency lasers, were able to bracket the ionisation potentials of clusters up to Fe_{25} to within a fraction of an electronvolt. By recording the variation in cluster ion intensity against laser fluence they determined the number of photons of a particular wavelength required to photoionise individual clusters. This showed that even at a cluster size of 25 atoms the ionisation potential was still more than 0.8 eV greater than the bulk work function. The other interesting point to arise from this investigation was that the ionisation potential did not monotonically decrease from that of the atom with increasing cluster size. This was not readily apparent from the cluster mass spectra recorded for iron in the current work as only one wavelength was used for ionisation, but a comparison with the mass spectrum of copper clusters in figure 4.2 shows a marked difference between the two elements.

Figure 4.4
Mass spectrum of Ag_{1-21} showing alternation in intensity between odd and even numbered clusters

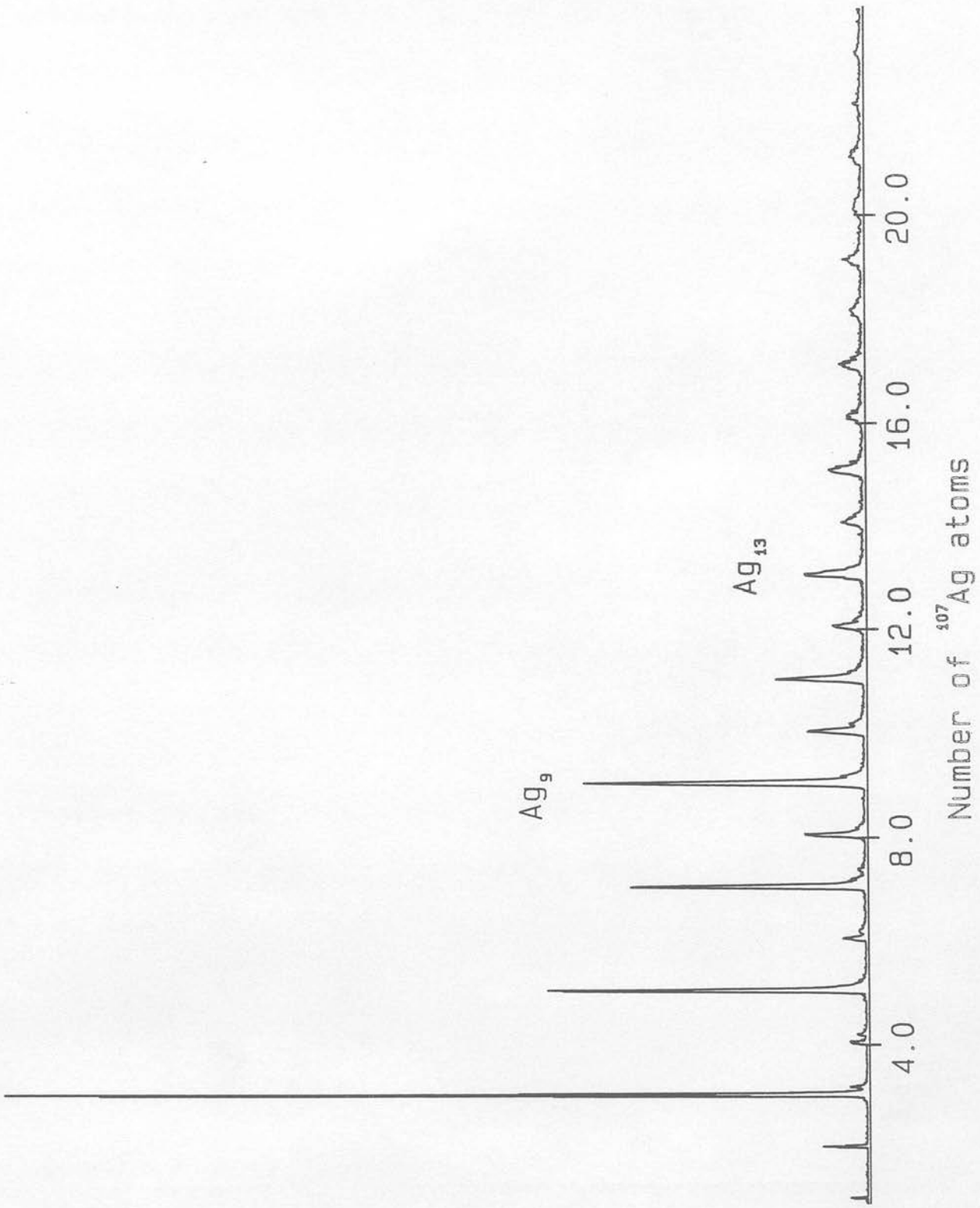

The cluster mass spectrum of copper, like that of silver shown in figure 4.4 displays an alternation in the recorded intensity between the odd and even numbered clusters. This behaviour has been observed previously, and can be explained by the adoption of the following simple model for the bonding in the clusters [11] - [14].

If it is assumed that, because of their contracted nature, the full d - orbitals on the copper and silver atoms play little part in the bonding, then the clusters can be compared with those of the group 1A metals. In this case the bonding is purely due to the interactions of the 1/2 filled s - orbitals. For even numbered clusters the highest occupied molecular orbital (HOMO) will be doubly occupied resulting in it having a strongly bonding character, and it will therefore have a relatively high ionisation potential. Conversely the odd numbered clusters will have a single unpaired electron in the HOMO, which will have an anti - bonding or non - bonding character. This electron will require less energy to remove it than one of the paired electrons in the HOMO of an even numbered cluster. Thus there will be an alternation in the ionisation potential of the clusters. If the ionisation potentials of the odd and even clusters lie at, respectively, less than and greater than the energy of a single photon of the photoionisation laser radiation, then a strong alternation in signal intensity will be expected. This arises because of the change in the cross - section between one and two photon absorptions (see section 4.6).

The ionisation potentials of copper atom (7.7 eV) and silver atom (7.6 eV) are greater than the 6.4 eV energy of a single ArF photon, as are the ionisation potentials of the respective dimers (Cu_2 = 7.9 eV, Ag_2 = 7.6 eV). Therefore

both the atom and dimer of copper and silver will require two photons of ArF radiation to achieve ionisation. This has previously been recorded experimentally, using an ArF laser for photoionisation, with measurements made of the cluster ion signal intensity as a function of the photoionisation laser intensity [13]. These studies showed a quadratic dependence of the ion signal on the laser intensity for the atom, dimer, and higher even numbered clusters. Odd numbered clusters higher than, and including, Cu_3 showed a linear dependence on the photoionisation laser intensity. Thus the odd / even alternation was shown to be a result of the changing ionisation cross - section between one and two photon absorptions required for ionisation.

Extending this model to the negative cluster ions, the reverse behaviour is expected as the odd numbered clusters will have two paired electrons in the HOMO, whereas the even numbered clusters will have a single unpaired electron occupying what was previously a strongly anti - bonding LUMO. Measurements of the electron affinities of copper clusters as a function of the cluster size were carried out by Zheng et. al., using photodetachment studies of negative cluster ions [14] [15]. These studies have shown that even numbered clusters have a lower electron affinity than odd numbered clusters. This has been taken as proof of the simple model described above.

4.5 Reactions of the clusters

The second main avenue of investigation opened up by the use of the mass selective technique described in this thesis has been the study of the reactions undergone by these clusters. These can be unimolecular decomposition reactions

or heterogeneous reactions with other reagents present in the source. The former are a source of much information on the structure and relative stability of different clusters [18]. They show up as changes in the intensity and shape of the time of arrival peaks of the individual ion packets. In the present work the amount of fragmentation occurring was reduced as much as possible by attenuating the laser energy when required, so as not to interfere with the spectroscopic studies of the dimers of copper and silver described in the following chapters.

Reactions of the clusters with other reagents can be easily monitored with the TOFMS as the appearance of additional peaks in the mass spectrum. These reagents can be added to the buffer gas or injected into the nozzle downstream of the point of laser vaporisation. Studies of the reactivity of small metal clusters should give information on their rôle in catalysis.

The only reaction observed in the course of the present work was with residual oxygen present in the system. All the mass spectra shown in this chapter exhibit cluster oxide peaks to some extent. The spectra in figures 4.5 and 4.6 show clusters of nickel and their oxides. Figure 4.6 shows a rise in the number of oxygen atoms commensurate with an increase in the number of metal atoms in the cluster.

The current instrumentation could easily be modified for investigations of the reactivity of the clusters by the addition of secondary solenoid valves for injecting reactants into the gas flow.

Figure 4.5
Mass spectrum of Ni_{1-28}

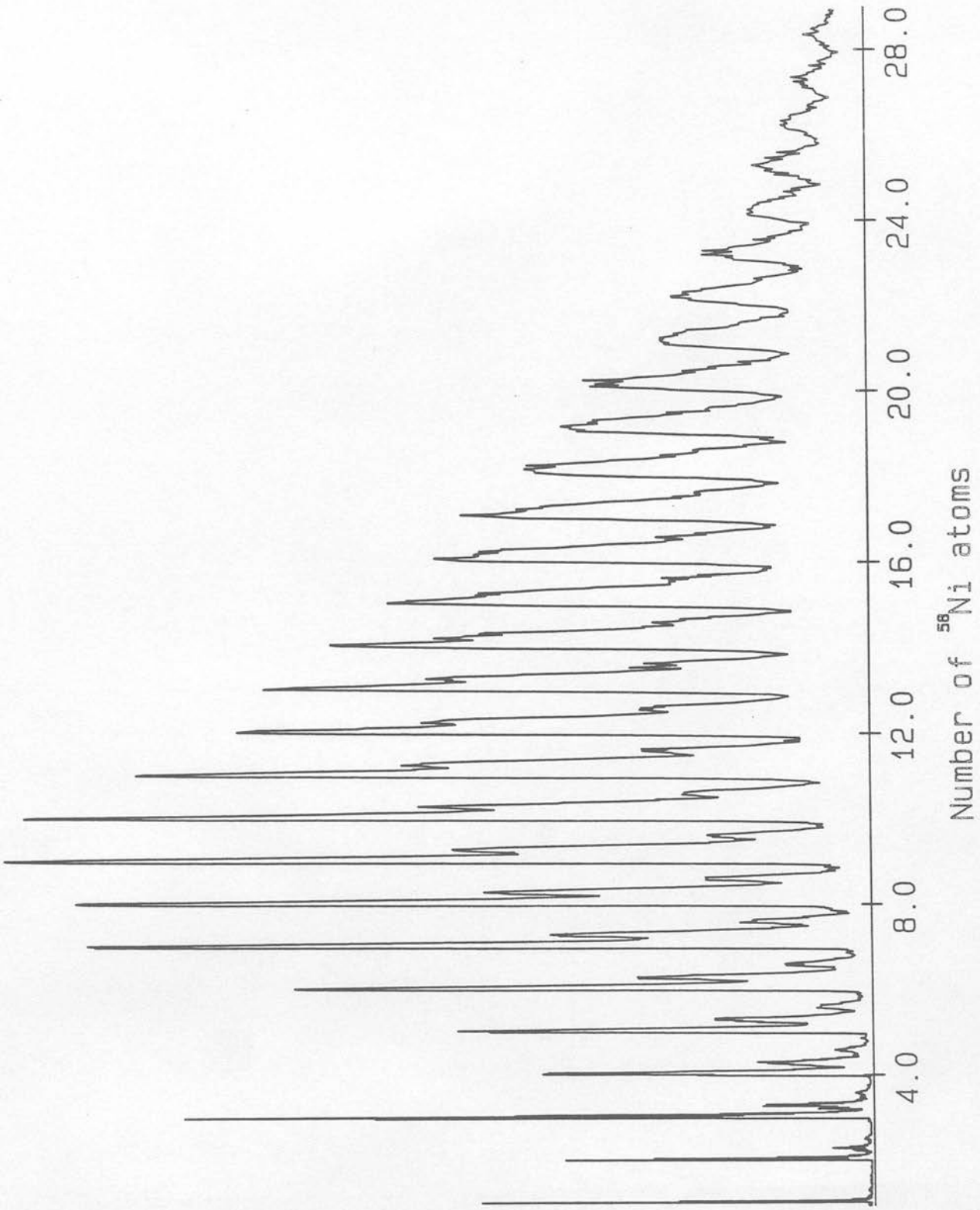

Figure 4.6
Mass spectrum of Ni_{1-5} and $Ni_{1-5}O_x$ showing increase in number of oxygen atoms with increasing cluster size

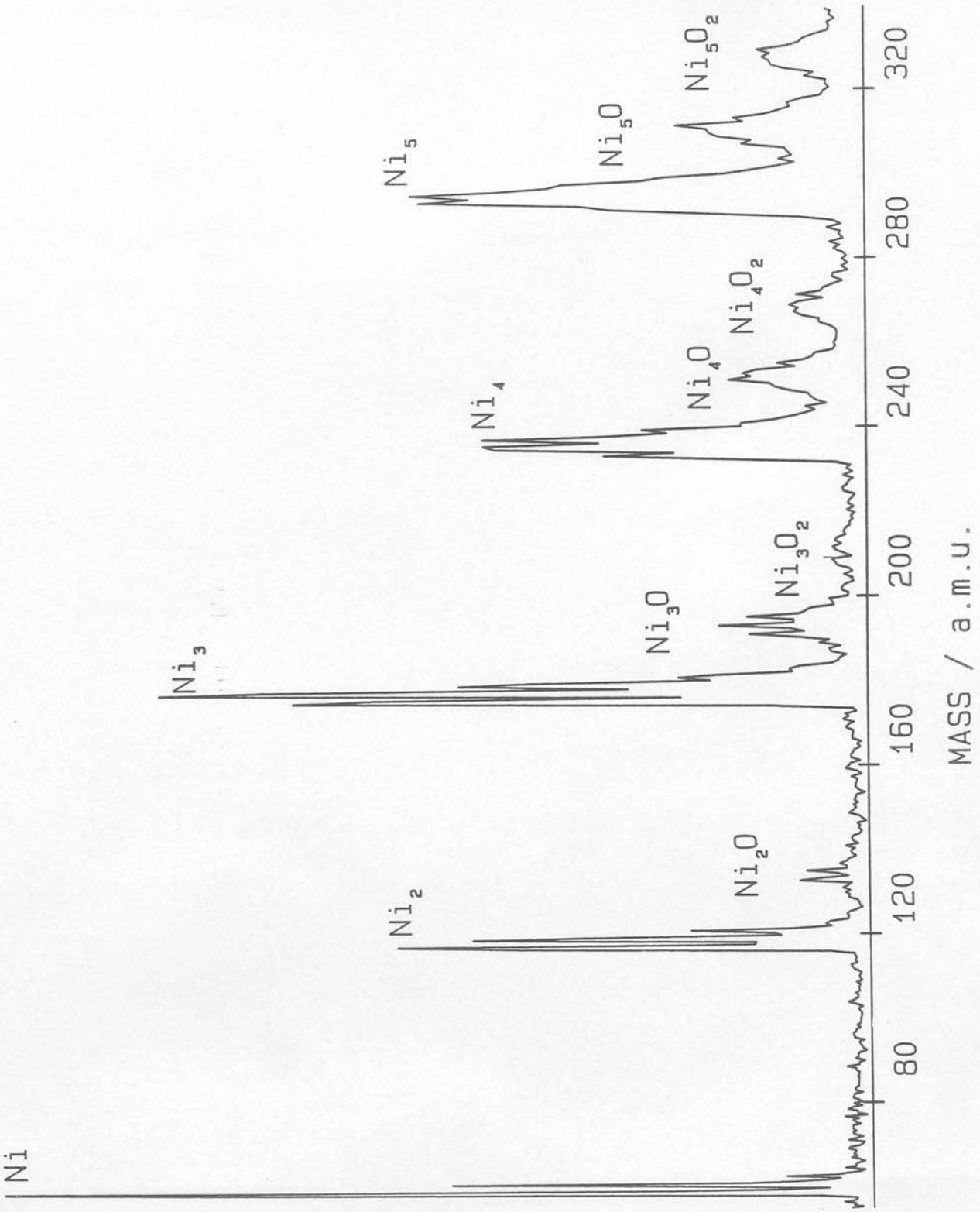

When coupled to a computer controlled gate for the pulses from the pulse delay generators, it would be possible to alternate between data shots where reactant was injected into the flow through the supersonic nozzle and those where no reactant was present. This would allow the background cluster ion signal to be subtracted to leave only the signal due to reactions of the clusters. This would be especially useful where reaction resulted in fragmentation of higher clusters into smaller clusters, as removal of the background signal would make any reaction products more visible. Highly reactive clusters would show up as negative signals in the spectrum after subtraction of the signal obtained in the absence of any reactant.

4.6 Resonant Ionisation

All the work described so far in this chapter has involved non resonant photoionisation of the metal clusters. Figure 4.7(b) shows the effect of resonant photoionisation achieved by employing two lasers, operating at different wavelengths. A tunable dye laser aligned coaxial with and counterpropagating the excimer laser photoionisation beam was used to excite a resonant transition to an excited state of silver dimer, which was then single photon ionised by the ArF laser. This gave a large increase in the recorded ion signal due to the reduction in cross section between absorption of two photons and one photon of the ArF laser radiation to achieve ionisation. Typically the cross section changes from $\sim 10^{-20}$ cm^2 for single photon absorption to $\sim 10^{-50}$ cm^4 sec for two photon absorption [16] [17]. The ratio of the signals for the Ag_3^+ and Ag^+ ions remains at 7:1 in both spectra, as these species are non - resonantly ionised by

the ArF laser. The relative intensity of the Ag_2^+ ion, however, increases from 0.7 of the Ag^+ ion intensity to 24 times the Ag^+ signal when the dye laser is tuned to a resonance corresponding to excitation to an electronically excited state of silver dimer.

This R2PI method was used to study the excited states of silver and copper dimer as described in the following chapters, using a continuously tunable dye laser to scan across individual rovibronic transitions.

Figure 4.7
Mass spectra of Ag_{1-3} showing the difference
between resonant and non - resonant photoionisation of Ag_2

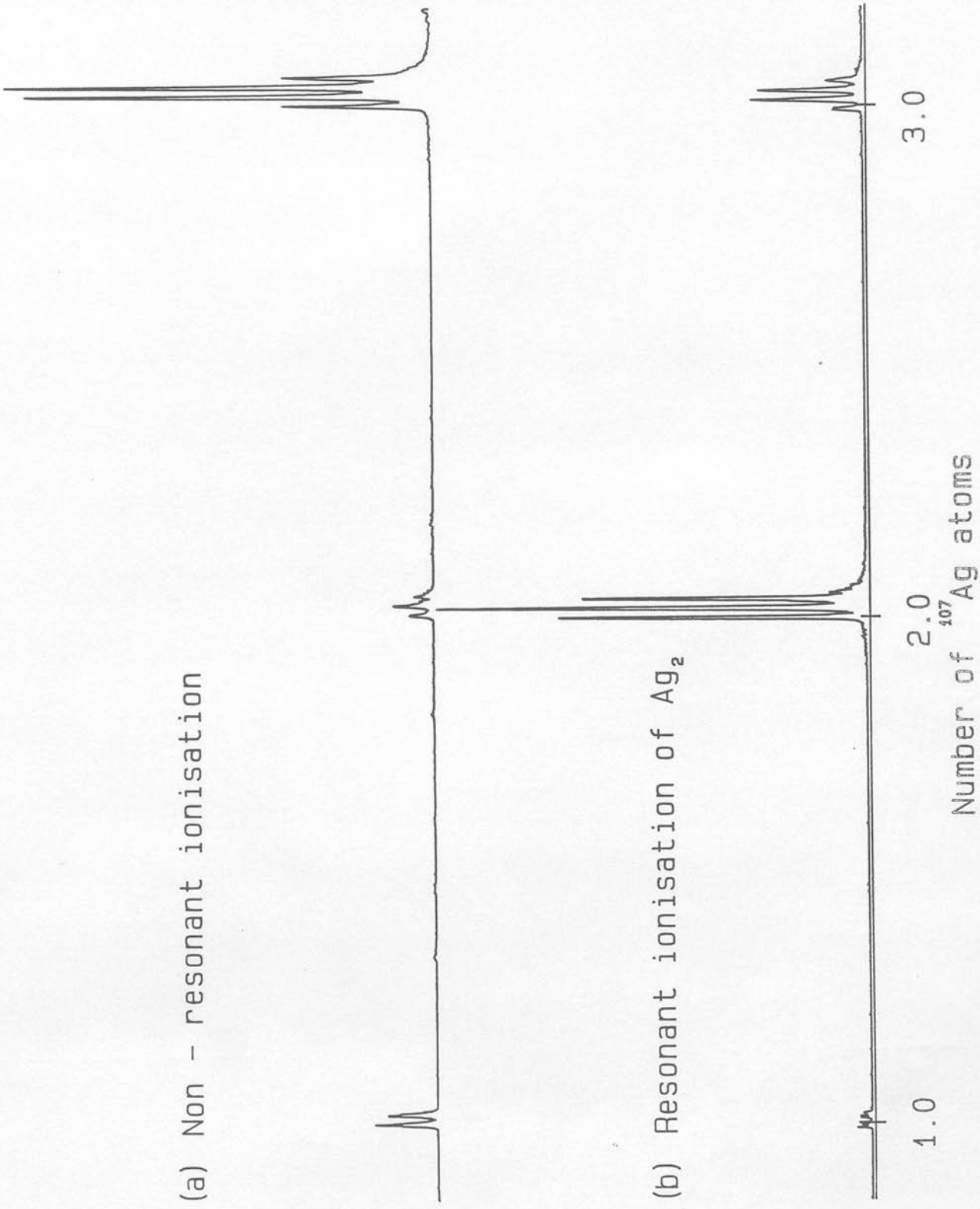

References

[1] Schissel P., J. Chem. Phys., **26**, p 1276, (1957)

[2] Hopkins J.B., Langridge - Smith P.R.R., Morse M.D., Smalley R.E., J. Chem. Phys., **78**, p 1627, (1983)

[3] Rohlfing E.A., Cox D.M., Petrovic-Luton R., Kaldor A., J. Phys. Chem., **88**, p 6227, (1984)

[4] Lai-Hing K., Cheng P.Y., Duncan M.A., J. Phys. Chem., **91**, p 6521, (1987)

[5] Duncan M.A., *PhD Thesis*, Houtston, 1981.

[6] Bergmann W., Dreihofer S., Gantefor G., Siekmann H.R., Meiwes - Broer K.H., Lutz H.O., *Elemental and Molecular Clusters, ed. Martins J.P.*, Springer - Verlag (Berlin), 1987.

[7] Knight W.C., Clemenger K., de Heer W., Saunders W., Chou M., Cohen M., Phys. Rev. Lett., **52**, p 2141, (1984)

[8] Cohen M.L., Chou M.Y., Knight W.D., de Heer W.A., J. Phys. Chem., **91**, p 3141, (1987)

[9] Rohlfing E.A., Cox D.M., Kaldor A, Chem. Phys. Lett., **99**, p 161, (1983)

[10] Wiley W.C., McLaren I.H., Rev. Sci. Instrum., **26**, p 1150, (1955)

[11] Baetzold R.C., J. Chem. Phys., **55**, p 4355, (1971)

[12] Baetzold R.C., J. Chem. Phys., **55**, p 4363, (1971)

[13] Powers D.E., Hansen S.G., Geusic M.E., Michalopoulos D.E., Smalley R.E., J. Chem. Phys., **78**, p 2866, (1983)

[14] Zheng L.S., Korner C.M., Brucat P.J., Yang S.H., Pettiette C.L., Craycraft M.J., Smalley R.E., J. Chem. Phys., **85**, p 1681, (1986)

[15] Cheshnovsky O., Brucat P.J., Yang S., Pettiette C.L., Craycraft M.J., Smalley R.E., *Proceedings of the International Symposium on The Physics and Chemistry of Small Clusters*, Richmond, Virginia, 1986.

[16] Johnson P.M., Otis C.E., Ann. Rev. Phys. Chem., **32**, p 139, (1981)

[17] Parker D.H., *Ultra Sensitive Laser Spectroscopy, Ed. Kliger D.S.*, Academic Press, New York, 1983.

[18] Brucat P.J., Zheng L.S., Pettiette C.L., Yang J., Smalley R.E., J. Chem. Phys., **84**, p 3078, (1986)

Chapter 5
High Resolution Electronic Spectroscopy of the J State of Cu_2

5.1 Introduction to the electronic spectroscopy of Cu_2

Copper dimer has been of major interest to both theoreticians [1] - [11], and experimentalists for a long time. The first spectra were observed in emission and absorption from King furnaces and cryogenic matrices, and gave electronic term values, vibrational constants, and in some cases rotational constants [2], [9], [12] - [21]. These studies have suffered from the high internal temperatures of the dimers created, and perturbation of the spectra by other agents present such as the matrix. The high temperatures meant that a great number of the vibrational and rotational levels were populated giving very congested spectra that were difficult to analyse reliably. Later studies by Smalley and co-workers [22] - [23] and others [15], [24] using supersonic molecular beam techniques combined with LIF or photoionisation TOFMS, similar to the apparatus described in earlier chapters, led to the determination of accurate gas phase rotational constants and bond lengths for some of the low lying states. The ionisation potential and electron affinity have been determined from beams of neutral [23] and negative ion [25] clusters. The major interest in copper has been as an intermediate case between the alkali and transition metals, for the testing of theoretical models of the bonding in metallic species. The ground state electron configuration of the copper atom is [Ar] $3d^{10}$ $4s^1$ and for this reason it is viewed as a pseudo alkali metal equivalent to potassium, with the full d-shell being essentially inert. The

other advantage of copper as a simple species for the testing of new theoretical methods is that the ground state of the atom has only one possible configuration with no spin orbit components and therefore can only give rise to one possible electronic configuration for the ground state of the dimer. The main thrust of the theoretical and experimental work is to elucidate what, if any, effect the 3d electrons have on the bonding properties of the copper atom. It is well known that the interaction of the 3d electrons can have a dramatic effect on the bonding of the transition metal dimers as witnessed in Cr_2 (Cr ground state electronic configuration is [Ar] $3d^5\ 4s^1$) where the bond length was observed to be 1.68 Å [26], much shorter than the 2.5 Å nearest neighbour distance in the bulk metal [27]. The effect of the d - electrons can also seen by comparing the dissociation energies of Cu_2 and K_2, both of which formally have a single 4sσ bond. D_0 for Cu_2 is 2.03 eV against 0.514 eV for K_2 [43]. The stronger bond in Cu_2 indicates some degree of d - d interaction or mixing of the d and s orbitals, though some of the increased bond strength will be due to the shortening of the 4sσ bond caused by the contraction of the 4s orbitals on going from left to right across the periodic table.

Copper dimer is used as the testbed for any theoretical modelling of these complex d-bonded systems as it is assumed that the d-d interaction is small in the ground state due to the two closed d^{10} shells. This small interaction between the d-shells is much simpler to simulate than the larger interactions that exist between open shell species as fewer orbitals must be correlated to obtain an accurate description of the bonding. Some treatments ignore any effect due to the 3d electrons, combining them into an inert core and only involving the 4s

valence electrons in the bonding interaction. These models tend to overestimate the bond length [2] [6] [9], whereas those incorporating the d-electrons in the configuration interaction give estimates of R_e closer to the experimentally derived values [6] [28]. Methods that do not take account of the d-electron interaction will obviously not be of much use for describing excited states where one (or more) of the d-electrons has been promoted, leaving an open d-shell which may have quite strong interactions.

Relativistic effects have been investigated in a number of theoretical studies and found to play a small part in the bonding characteristics (R_e, ω_e) of copper dimer [6] [7] [8] [11]. Typical relativistic contractions in the bond length of the copper dimer are in the region of 0.03Å [7] [8].

The ground and lowest electronically excited states have been studied in some depth and are well characterised [46]. The electronically excited states of copper dimer provide a means by which theoretical models can be extended to cope with open d - shell species, as a basis for modelling other transition metal dimers. All the states of copper dimer investigated to date have been shown to have a longer equilibrium bond length than the ground state, which will be expected to decrease rather than increase the interaction between the d - electrons, the 3d orbitals being significantly contracted with respect to the 4s orbital ($<R_{4s}>/<R_{3d}> = 3.36$ [6]).

The spectroscopic constants for the known electronic states of Cu_2 are summarised in table 5.1 and the RKR curves calculated from these constants are shown in figure 5.1.

Table 5.1
Spectroscopic constants of the known electronic states of $^{63}Cu_2$

	T_e / cm^{-1}	ω_e / cm^{-1}	$\omega_e x_e$ / cm^{-1}	B_e / cm^{-1}	α_e / cm^{-1}	$10^5 D_e$ / cm^{-1}	R_e / Å
J 0_u^+	37440.1	288.4	0.64	*0.1166*	*0.0021*		*2.138*
I	~35000	280	1				
H	~36782						
c ($^3\Delta$)	~34870	100	0.5				
b ($^3\Delta$)	~33120	90	0.5				
G	~30753	116.0	0.046				2.73
F	~28560	248.0	0.90				
E	~27153	231.5	1.25				
D ($^3\Delta$)	~25560	~160					2.38±0.03
C	~21870	221	2	0.10456	0.000967		2.257
B 0_u^+	21758.35	245.8	2.0	0.09889	0.000606	6.30	2.3274
A 0_u^+	20433.2	192.47	0.353	0.10309	0.000906	11.34	2.2797
a $^3\Sigma_u^+$	~15420	125±25					
X $^1\Sigma_g^+$	0	266.43	1.035	0.10874	0.000614	7.16	2.2197

The above data has been assimilated from references [43], [39], and [46]. Uncertain assignments are given in brackets and results from this work in italics.

Figure 5.1
Known electronic states and some atomic asymptotes of Cu_2.

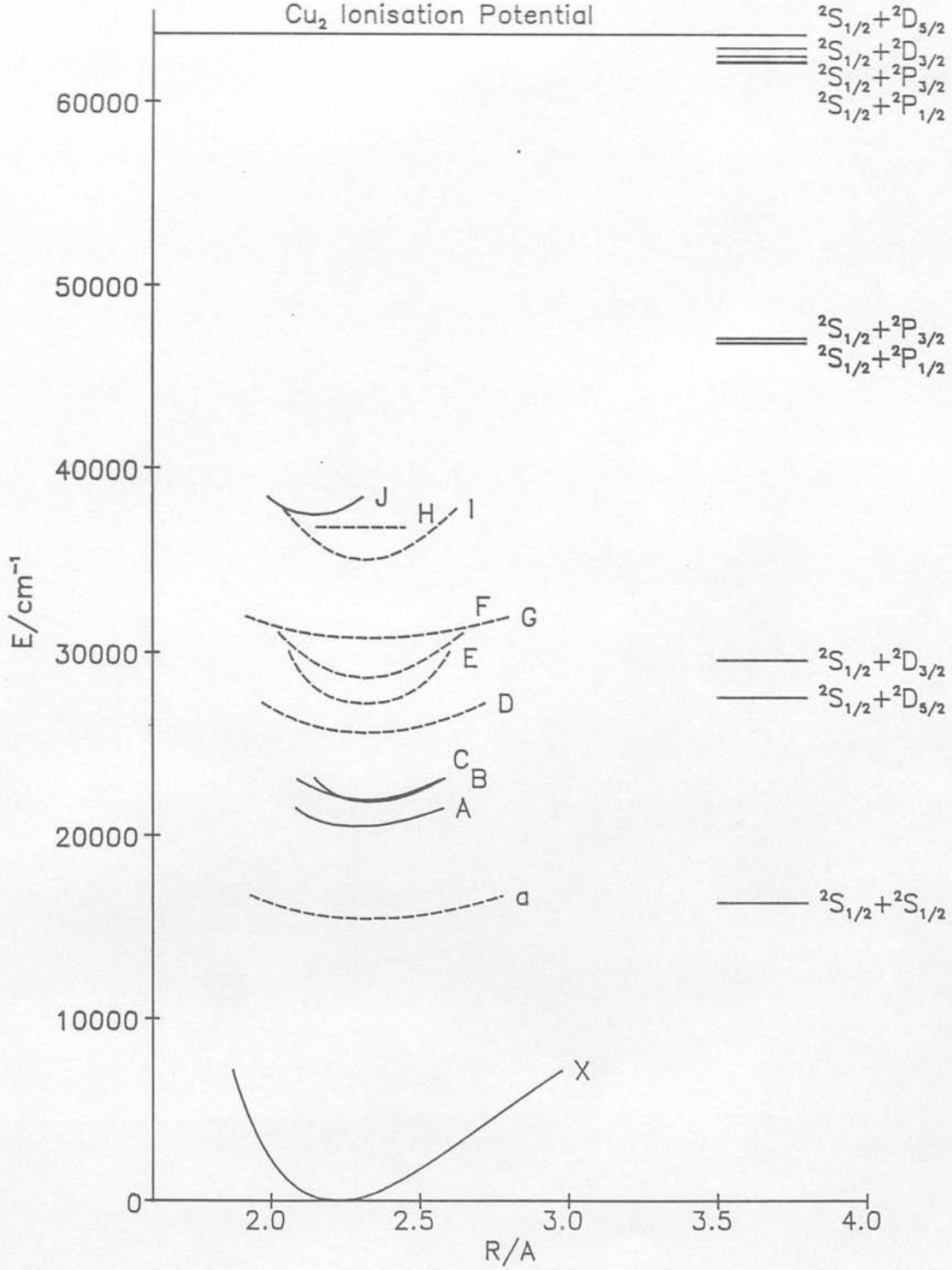

Note that the atomic limits shown in figure 5.1 have been adjusted by the addition of the Cu_2 ground state dissociation energy of 16344 cm^{-1} [46]. States for which no rotational analysis has been reported are shown as dashed curves. The position of these curves along the X - axis does not imply anything about the bond length, the curves having been constructed from the known vibrational constants and placed vertically according to the known term values.

5.2 Spectroscopy of Cu_2 in the ultra violet

Little is known about the states of copper dimer in the ultra violet region of the spectrum, compared to those in the visible region. None of the states that have been observed have been rotationally analysed [43], [46]. A series of states lying in the ultra-violet region of the spectrum were initially observed by Powers et. al. in 1983 [23]. They recorded the vibronic spectra of five different systems lying between 28560 cm^{-1} and 37440 cm^{-1} which they labelled systems I - V. These states have since been relabelled F - J [46]. The only other study of the excited states of Cu_2 in the UV region was by Rohlfing and Valentini [29] who used LIF to obtain an extended spectrum of the fluorescence from the G state to the ground state. Fluorescence from $v'=0$ to $v''=0 \rightarrow 72$ allowed accurate determination of the ground state vibrational constants. Some of these states are thought to have been observed in emission from matrix isolated copper clusters [2], but there is some disagreement about whether or not the observed emission comes from the copper dimer or larger copper clusters present in the matrix [42].

Other than the above mentioned studies there has been no other work

carried out on the spectroscopy of the UV states of Cu_2, in particular no rotational analyses have been obtained. The J state is particularly noteworthy in that it is one of only two excited states of Cu_2 observed, to have a larger vibrational constant (ω_e) than the ground state. The significance of this is realised by the application of the empirically derived Badgers' Rule [30] - [33], modified to relate ω_e to R_e:

$$R_e \propto k_e^{-1/3} \tag{5.1}$$

when substituted with the equation for the classical vibration frequency:

$$\omega_e = (c/2\pi) \times (k_e/\mu)^{1/2} \tag{5.2}$$

$$\Rightarrow R_e \propto \omega_e^{-2/3} \tag{5.3}$$

Using this relationship with the known R_e and ω_e for the ground state and ω_e for the J state [46], the equilibrium bond length of the J state was predicted to be 2.105 Å. This is markedly less than the ground state bond length of 2.220 Å, pointing to a greater involvement of the d - electrons in the bonding. To accurately determine the bond length it was necessary to rotationally resolve the spectrum observed for the transition to the J state from the ground state.

5.3 Spectroscopic investigation of the J ← X system of Cu_2

Cold copper dimer was generated by the laser vaporisation / supersonic expansion technique described in chapter 2. The copper target rod (Johnson

Matthey Specpure grade) contained both isotopes in natural abundance. The J state was studied by one colour R2PI using the Lambda-Physik excimer pumped dye laser system described earlier (see section 2.5.3). The laser was operated with coumarin 153 dye (Lambdachrome LC5400, 522 - 600 nm, peak at 540 nm). The output was frequency doubled with an FL31 doubling module (KDP crystal), with the residual visible light being removed by insertion of a UG5 filter into the path of the beam. This filter was not uniform in its transmission of the frequency doubled light, so by moving the position of the filter in the beam different amounts of attenuation could be achieved. A 5 times Ga lilean telescope [34] was used to further collimate the beam to a 2 mm spot in the ion source of the TOFMS. This was necessary to obtain sufficient power density for the two photon absorption required for ionisation. Direct focusing with a single lens was not used as it was found too difficult to control the power. Too much power resulted in non - resonant ionisation becoming the dominant process as well as power broadening the transitions which resulted in a loss of resolution when recording rotational spectra of the individual bands. Too little power did not give an intense enough resonant signal to overcome the background noise. Single lens focusing was extremely sensitive to both the lens position and the amount of attenuation in the beam. The telescope arrangement was not so sensitive to changes in the attenuation making it easier to control the power input.

The low abundance of the $^{65}Cu_2$ isotopomer which constituted only 9.5% of the total dimer distribution (see figure 4.1), meant that there was insufficient signal intensity in the resonant features of this system to overcome the non -

resonant background signal. The other two isotopomers, $^{63}Cu_2$ and $^{63}Cu^{65}Cu$, were present as 47.7% and 42.7% of the total dimer signal respectively, and well resolved spectra of each were obtained. A contributing factor to the poor integrated signal intensity observed for the $^{65}Cu_2$ species was the temporal jitter in the output of the dye laser. This is discussed fully in section 3.2.9, but briefly; any fluctuations in the time of ionisation led to a different time of arrival for the ions at the detector relative to the TD trigger. This meant that the ion signal was no longer recorded in the channels being integrated.

Low resolution (0.15 cm^{-1} / step) scans over the region where the (0 - 0) and (1 - 0) bands of the J ← X system were observed by Powers et. al. allowed the spectra in figures 5.2 and 5.3 to be recorded. These spectra were obtained without the use of the FL83 intracavity etalon (see section 2.5.3). The wavenumber scale in these spectra was not calibrated to any absolute transition, the scale being produced from the laser dial reading and the grating step size. The measured origins of the (0 - 0) and (1 - 0) bands for $^{63}Cu_2$ are 37463.1 cm^{-1} and 37750.9 cm^{-1}, compared to 37451.1 cm^{-1} and 37738.4 cm^{-1} as measured by Powers et. al. [23]. The isotope shifts of the (0 - 0) and (1 - 0) bands are 0.2 cm^{-1} and 2.6 cm^{-1}, these were determined more accurately from the rotationally resolved spectra as described below. Both of these spectra show clear P and R branches, degraded to the blue. This points to a shorter bond length in the J state compared to the ground state, as predicted by Badgers' rule. No hot bands were observed, demonstrating the high degree of cooling achieved with the supersonic molecular beam source used.

Figure 5.2 Low resolution R2PI spectra of the J ← X (0 - 0) band of Cu_2

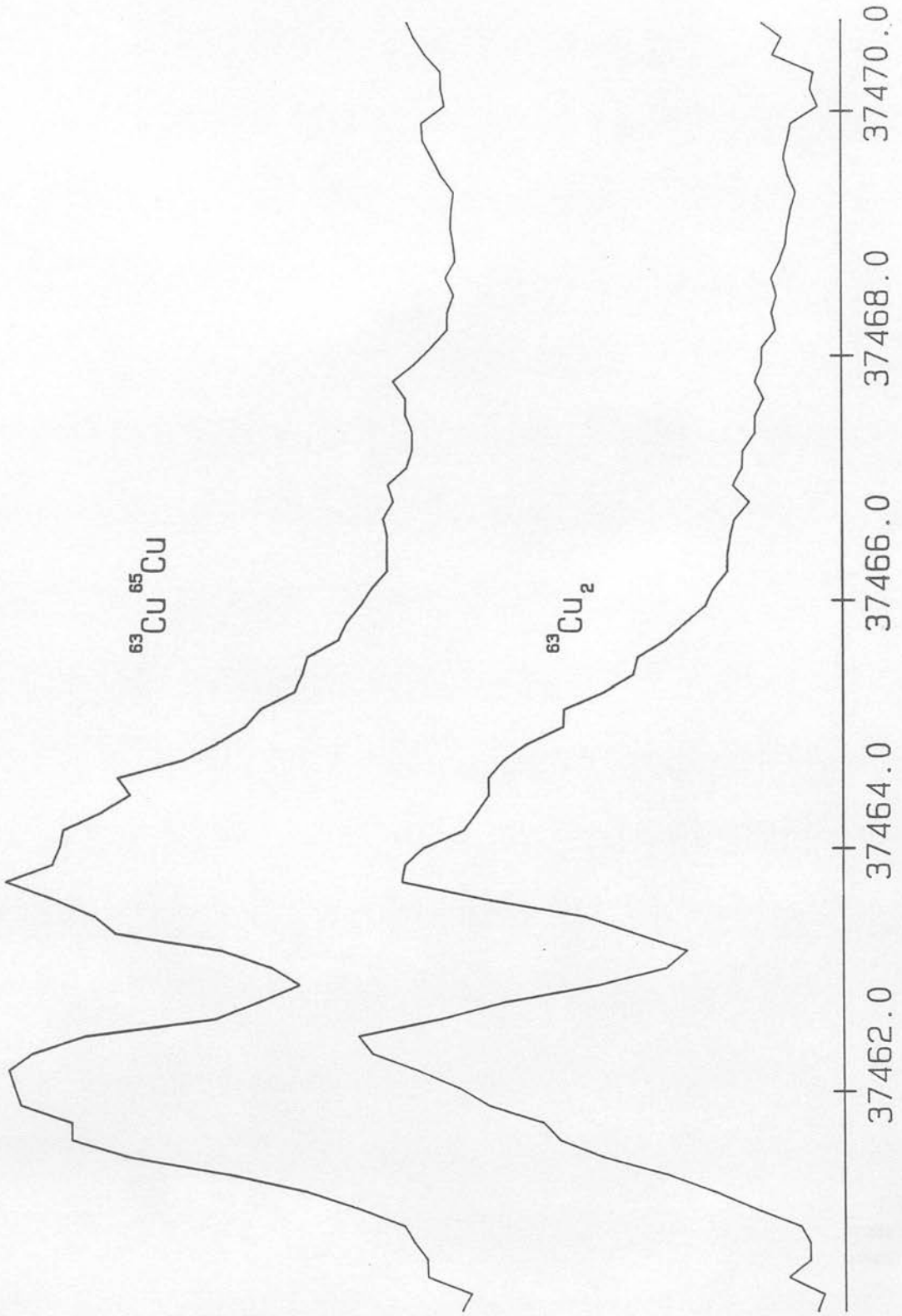

Figure 5.3 Low resolution R2PI spectra of the
$J \leftarrow X$ (1 - 0) band of Cu_2

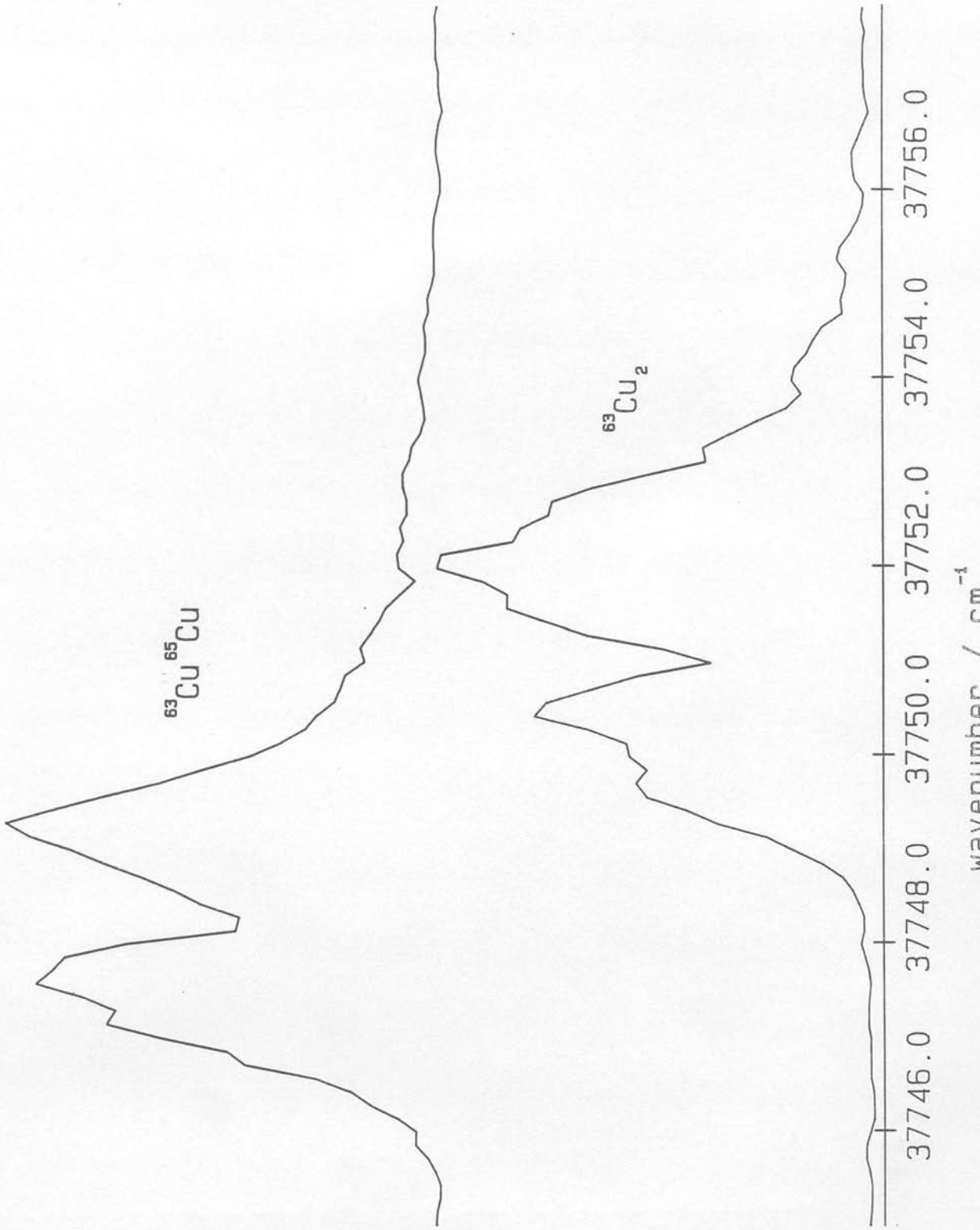

5.4 Rotational analysis of the high resolution spectra of Cu_2 J ← X

Once the approximate position of the bands had been found an airspaced intracavity etalon (FL83, see section 2.5.3) was inserted to narrow the output bandwidth to 0.04 cm^{-1} (≡ 0.08 cm^{-1} when frequency doubled). The use of the intracavity etalon with the FL54 confocal monitor etalon (FSR = 0.1 cm^{-1}, finesse = 25) enabled rotationally resolved spectra to be recorded with concurrent wavelength calibration. Part of the fundamental output of the laser was split off, passed through the confocal etalon and monitored with a photodiode. This provided a set of fringes as an accurate wavelength calibration. R2PI spectra of the (0 - 0) and (1 - 0) bands for the homonuclear $^{63}Cu_2$ species are shown in figures 5.4(a) and 5.5(a). These spectra are the result of summing 60 experimental shots at each point during a scan over the wavelength region at 0.000318 nm/step. They have been smoothed by the 9 point method of Savitzky and Golay [47] as described in chapter 3. The mass resolved spectra together with their associated etalon fringes were processed using ODIN (see chapter 3) to determine the positions of the peaks and the wavelength calibration factors to obtain the relative line positions in wavenumbers. The line positions were calculated as an offset in bin numbers[2] from an arbritary zero point, normally taken as the first recorded point in a spectrum.

---

[2] A bin number corresponds to one laser step.

Figure 5.4 High resolution R2PI spectrum of the J ← X (0 - 0) band of $^{63}Cu_2$

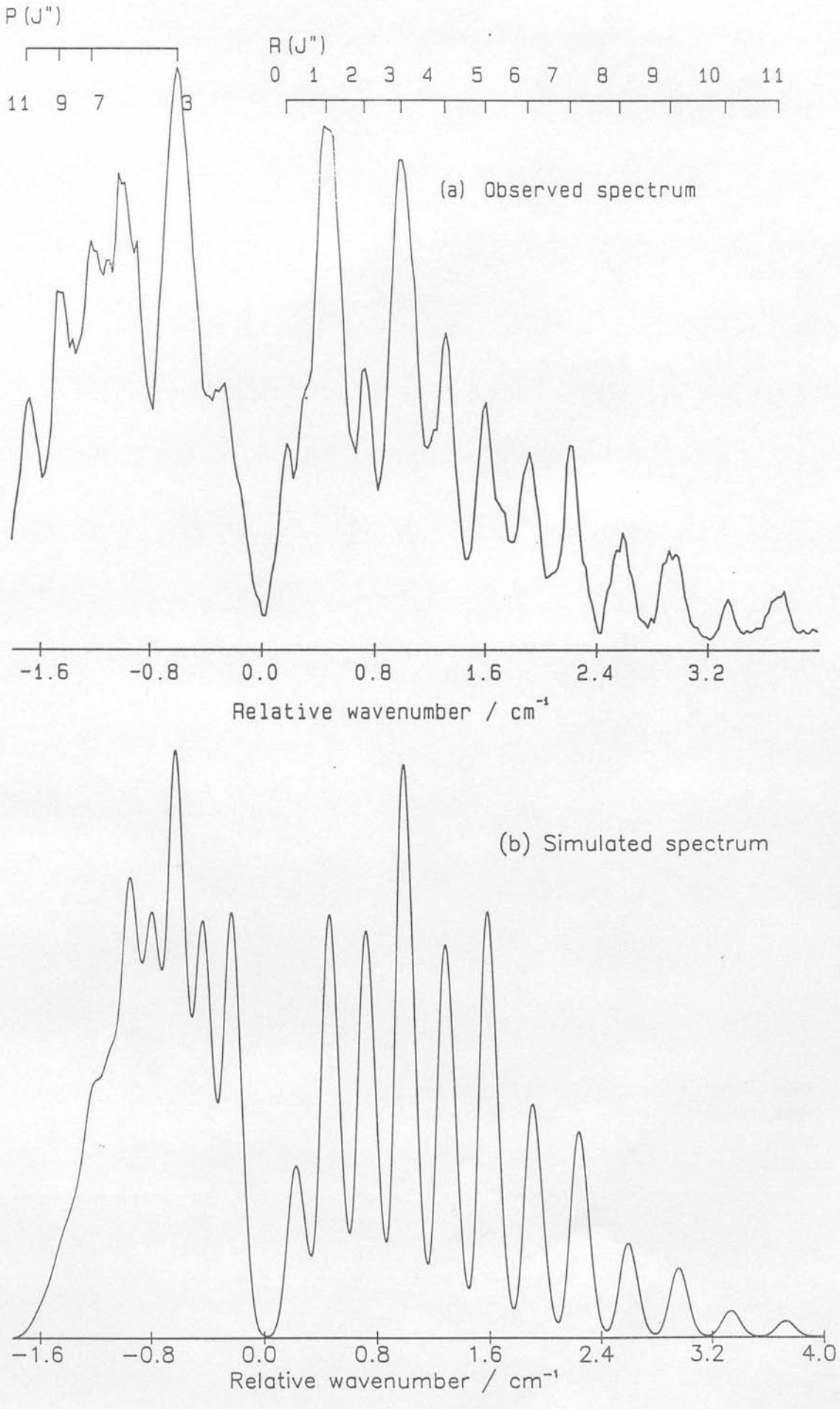

Figure 5.5 High resolution R2PI spectrum of the J ← X (1 - 0) band of $^{63}Cu_2$

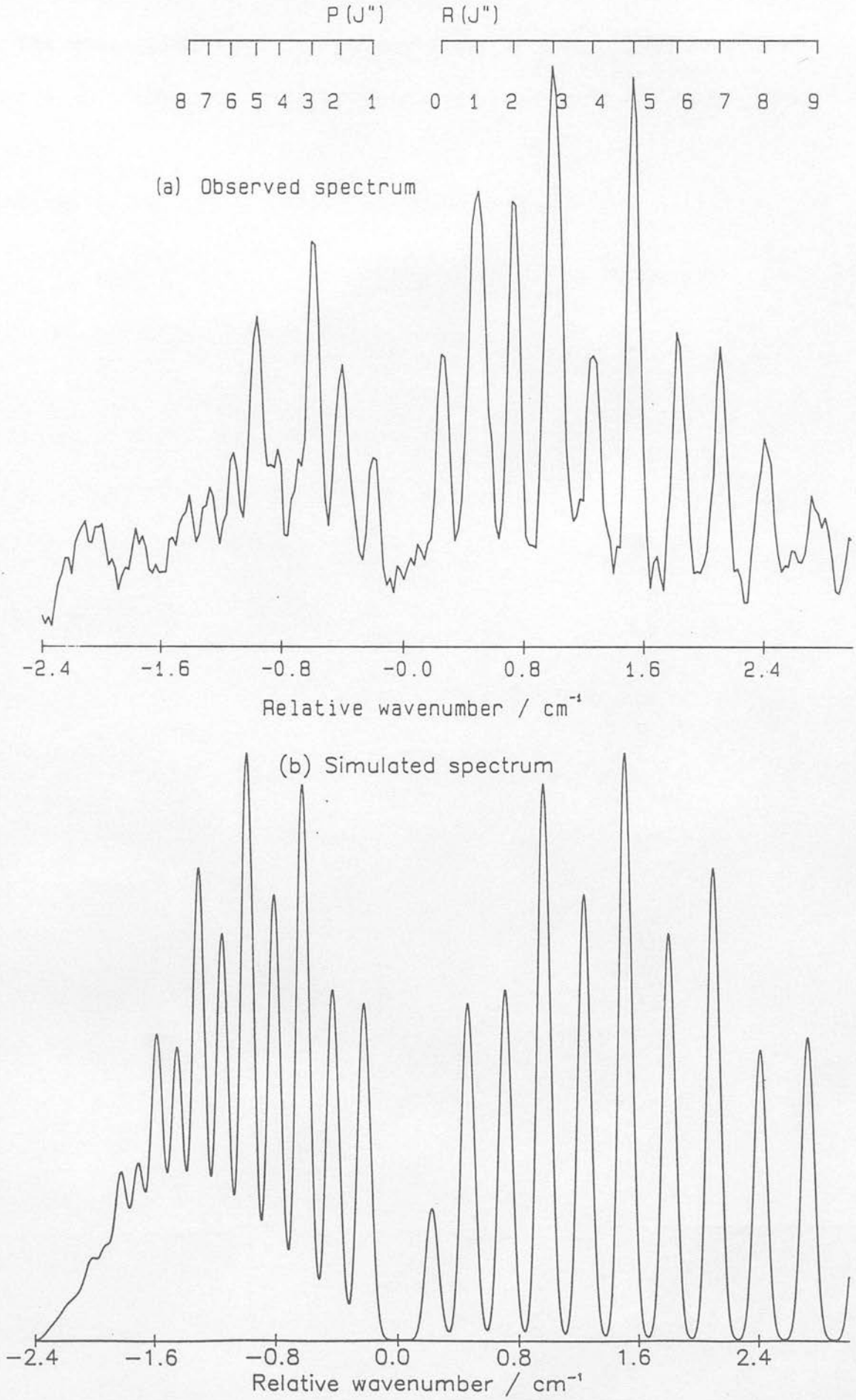

The conversion of the offset from bin numbers to wavenumbers was accomplished using a polynomial whose coefficients were calculated by fitting the peaks of the monitor etalon fringes (spacing 0.1 cm^{-1}) by a least mean squares fit. The relative positions of the rotational lines (in wavenumbers) were then used to determine the excited state rotational constants. Individual lines identified in the P and R branches were fitted simultaneously to the following functions by a least mean squares method [35]:

$$E_P = B_v'J''(J''-1)-D_v'(J''(J''-1))^2 + \ldots\ldots - B_v''J''(J''+1)+D_v''(J''(J''+1))^2-\ldots\ldots \quad (5.4)$$

$$E_R = B_v'(J''+1)(J''+2)-D_v'((J''+1)(J''+2))^2 + \ldots\ldots - B_v''J''(J''+1)+D_v''(J''(J''+1))^2-\ldots\ldots \quad (5.5)$$

where:

$E_{P/R}$ = relative line position in cm^{-1}.

J' / J" = upper / lower state rotational level.

The computer program written to accomplish this analysis of the recorded spectra is given in appendix C. This method was used to evaluate the $B_v'(J)$ and $B_0''(X)$ values for each isotopomer. The observed and calculated line positions for the (0 - 0) and (1 - 0) bands of the $^{63}Cu_2$ and $^{63}Cu^{65}Cu$ isotopomers along with the derived rotational constants are given in tables 5.2 - 5.5. The constant term (A_0) calculated by the least mean squares fit is the offset of the origin of the band from the arbritary zero chosen for each spectrum.

Table 5.2
Observed and calculated line positions and rotational constants for the J ← X (0 - 0) band of $^{63}Cu_2$

Branch	J"	Obs. / cm^{-1}	Calc. /cm^{-1}	Resid. / cm^{-1}
P	7	-1.213	-1.214	0.001
P	3	-0.605	-0.607	0.002
R	1	0.478	0.477	0.001
R	3	1.009	1.012	-0.003
R	4	1.318	1.301	0.017
R	5	1.608	1.604	0.004
R	6	1.920	1.922	-0.002
R	8	2.583	2.601	-0.018
R	9	2.943	2.962	-0.019
R	10	3.338	3.338	0.000
R	11	3.728	3.728	0.000
R	12	4.151	4.133	0.018

Reduced $\chi^2 = 0.0001$

Floating both upper and lower state constants ⇒

$B_0'' = 0.1082(10)\ cm^{-1}$

$B_0' = 0.1155(9)\ cm^{-1}$

With ground state $B_0 = 0.1084\ cm^{-1}$ (giving calculated positions and residuals as above):

$A_0 = 1.8563(108)\ cm^{-1}$

$B_0' = 0.1156(1)\ cm^{-1}$

$R_0 = 2.147(1)Å$

Table 5.3
Observed and calculated line positions and rotational constants for the J ← X (0 - 0) band of $^{63}Cu^{65}Cu$

Branch	J"	Obs. / cm^{-1}	Calc. /cm^{-1}	Resid. / cm^{-1}
P	7	-1.220	-1.225	0.005
P	4	-0.780	-0.777	-0.003
R	1	0.455	0.466	-0.011
R	2	0.704	0.718	-0.014
R	4	1.276	1.261	0.015
R	5	1.565	1.552	0.013
R	6	1.855	1.856	-0.001
R	7	2.168	2.172	-0.004
R	9	2.862	2.844	0.018
R	10	3.183	3.199	-0.016
R	11	3.571	3.567	0.004
R	12	3.942	3.948	-0.006

Reduced $\chi^2 = 0.0001$

Floating both upper and lower state constants ⇒

$B_0'' = 0.1068(4)\ cm^{-1}$

$B_0' = 0.1133(3)\ cm^{-1}$

With ground state $B_0 = 0.1068\ cm^{-1}$ (giving calculated positions and residuals as above):

$A_0 = 1.6396(108)\ cm^{-1}$

$B_0' = 0.1132(1)\ cm^{-1}$

$R_0 = 2.153(1)Å$

Table 5.4
Observed and calculated line positions and rotational constants for the J ← X (1 - 0) band of $^{63}Cu_2$

Branch	J"	Obs. / cm^{-1}	Calc. /cm^{-1}	Resid. / cm^{-1}
P	8	-1.451	-1.451	0.000
P	7	-1.310	-1.305	-0.005
P	6	-1.148	-1.149	0.001
P	5	-0.995	-0.983	-0.012
P	3	-0.619	-0.620	0.001
P	2	-0.432	-0.423	-0.009
P	1	-0.220	-0.217	-0.003
R	0	0.238	0.227	0.011
R	1	0.463	0.464	-0.001
R	2	0.711	0.711	0.000
R	3	0.978	0.968	0.010
R	4	1.239	1.236	0.003
R	5	1.512	1.513	-0.001
R	6	1.813	1.801	0.012
R	7	2.097	2.099	-0.002
R	8	2.398	2.407	-0.009
R	9	2.717	2.725	-0.008
R	10	3.062	3.053	0.009

Reduced $\chi^2 = 0.0001$

Floating both upper and lower state constants ⇒

$B_0'' = 0.1086(4)\ cm^{-1}$

$B_1' = 0.1136(3)\ cm^{-1}$

With ground state $B_0 = 0.1084\ cm^{-1}$ (giving calculated positions and residuals as above):

$A_0 = 4.5251(50)\ cm^{-1}$

$B_1' = 0.1135(1)\ cm^{-1}$

$R_1 = 2.166(1)Å$

Table 5.5
Observed and calculated line positions and rotational constants for the J ← X (1 - 0) band of $^{63}Cu^{65}Cu$

Branch	J"	Obs. / cm^{-1}	Calc. /cm^{-1}	Resid. / cm^{-1}
P	8	-1.396	-1.393	-0.003
P	7	-1.245	-1.258	0.013
P	6	-1.107	-1.112	0.005
P	5	-0.920	-0.955	0.035
P	4	-0.779	-0.787	0.008
P	3	-0.619	-0.607	-0.012
P	2	-0.436	-0.416	-0.020
P	1	-0.232	-0.214	-0.018
R	0	0.224	0.225	-0.001
R	1	0.460	0.461	-0.001
R	2	0.699	0.708	-0.009
R	3	0.981	0.967	0.014
R	4	1.245	1.237	0.008
R	5	1.510	1.518	-0.008
R	6	1.819	1.811	0.008
R	7	2.123	2.115	0.008
R	8	2.404	2.430	-0.026
R	9	2.756	2.756	0.000

Reduced $\chi^2 = 0.0002$

Floating both upper and lower state constants ⇒

$B_0'' = 0.1064(7)\ cm^{-1}$

$B_1' = 0.1121(6)\ cm^{-1}$

With ground state $B_0 = 0.1068\ cm^{-1}$ (giving calculated positions and residuals as above):

$A_0 = 1.6760(104)\ cm^{-1}$

$B_1' = 0.1124(2)\ cm^{-1}$

$R_1 = 2.160(2)Å$

This offset has been subtracted from the measured and calculated line positions so they are listed as offsets from the band origin. The difference between the A_0 constants for the different isotopes of the same vibrational band is the combined electronic and vibrational isotope shift.

Some variation in the constants calculated from spectra recorded at different times was observed. This took the form of an increase (or decrease) in both constants when neither was fixed. However this discrepancy disappeared when the known ground state rotational constant was included in the fit. The constants for the (1 - 0) band of $^{63}Cu^{65}Cu$ in table 5.5 show this effect to a small degree. The reason for this discrepancy has not yet been identified.

Once the best fit of the lines had been found by excluding those lines which led to large deviations in the calculated B_0'' compared to the accepted value, or were shown to be anomalous by calculating the combination differences between the appropriate P and R branch lines, the accepted ground state rotational constant was inserted into the fit. The B_v' values calculated when the ground state constant was held constant are given in tables 5.2 - 5.5. The errors quoted throughout this analysis are twice the statistical standard deviation calculated by the least mean squares fit of the unweighted line positions as it was assumed that the peak finding routine in ODIN found all the peaks to the same degree of precision. As no absolute wavelength calibration was made when the spectra were recorded it was not possible to combine the spectra for different vibrational levels to directly obtain the vibrational dependence of the rotational constant. The B_e and α_e values for the J state shown in table 5.6 were calculated by substituting the B_0 and B_1 values into the standard expression:

$$B_v = B_e - (v+0.5)\alpha_e \tag{5.6}$$

The rotational constants for the different isotopes are expected to ratio with the mass as given in the following equations [36]:

$$B_{e(i)} = \rho_{(i)}^2 B_e \tag{5.7}$$

$$\alpha_{e(i)} = \rho_{(i)}^3 \alpha_e \tag{5.8}$$

$$\text{Where } \rho = (\mu/\mu_i)^{1/2}, \quad \mu = \text{reduced mass} \tag{5.9}$$

For the B_e constant the ratio of the value for $^{63}Cu^{65}Cu$ to that of the $^{63}Cu_2$ isotopomer should be 0.9846. The ratio of the calculated B_e' values for the two isotopes is 0.9743, within 1.1% of the expected value.

The combined vibrational and electronic isotope shifts calculated from the difference between the A_0 constants determined for each isotope, for the (0 - 0) and (1 - 0) bands are 0.217(15) cm^{-1} and 2.849(12) cm^{-1} respectively. The calculated values of the vibrational isotope shifts from the data in table 5.1 are 0.114 cm^{-1} and 2.294 cm^{-1} for the (0 - 0) and (1 - 0) bands respectively, and the values measured by Powers et. al. [23] were <0.1 cm^{-1} and 3.2 cm^{-1} respectively, the difference between the latter two sets of values suggesting some anomaly in either the measured positions of the vibrational bands or the vibrational constants calculated from them.

Table 5.6
Equilibrium spectroscopic constants and isotope shifts calculated for the J state of Cu_2

	$^{63}Cu_2$	$^{63}Cu^{65}Cu$
α_e / cm^{-1}	0.0021(1)	0.0008(1)
B_e / cm^{-1}	0.1166(1)	0.1136(2)
R_e / Å	2.138(1)	2.149(2)

Isotope shifts:
(in sense of to go from $^{63}Cu^{65}Cu$ origin to $^{63}Cu_2$ origin add the following values)

for $J \leftarrow X$ (0 - 0) = 0.217(15) cm^{-1}

for $J \leftarrow X$ (1 - 0) = 2.849(12) cm^{-1}

The difference between the isotope shift measured in the present work and the previous values was thought to be due to the earlier measurements having been made on the position of the band head rather than the origin of each vibrational band. As can been seen from the spectra presented for the (0 - 0) and (1 - 0) bands the position of the bandhead observed in vibrational studies changes its position relative to the origin, making it an unreliable marker of the relative positions of the origins of the vibrational bands.

The bond lengths for the different vibrational levels and the equilibrium bond length were calculated by substituting the appropriate value for the rotational constant into the standard equation for a rigid rotor [37]. The values obtained for the different vibrational levels and at equilibrium for both isotopomers are given in tables 5.2 - 5.5 and 5.6. The equilibrium bond length for the $^{63}Cu_2$ isotopomer agrees with that predicted using Badgers' Rule to within 1.6%, showing the utility of this empirically derived rule.

5.4.1 Simulated Spectra

Simulations of the experimental spectra were carried out using the J state constants determined in this work together with the previously known ground state rotational constants [43] to calculate the line positions. The intensities of the rotational lines were calculated using the Honl - London formulae for a $\Delta\Lambda = 0$ transition [36]. The population distribution over the ground state rotational levels was assumed to follow Boltzmann statistics. The temperature was estimated initially and then fine tuned to match the rotational distribution of the observed spectra. A rotational temperature of 5 K was found to give the closest

match between the observed and calculated spectra. The simulated spectra shown in figures 5.4(b) and 5.5(b) were generated by convoluting the calculated line positions and intensities with a Gaussian function describing the finite bandwidth of the dye laser (0.08 cm^{-1}). The Doppler width of the transition was ignored as it was $1/40^{th}$ of the laser bandwidth at the temperatures attained in the supersonic beam. The odd - even intensity alternation in the spectra of the homonuclear $^{63}Cu_2$ species is due to nuclear spin statistics ($I_{Cu} = 1.5$), which results in an alternation in the intensity of transitions from the odd numbered J'' levels to those from even numbered J'' levels of $(I+1)/I$ (= 5:3) [36]. The heteronuclear species $^{63}Cu^{65}Cu$ did not show this intensity alternation as it has no centre of symmetry.

5.5 Assignment of the upper (J) state electronic configuration

The assignment of an electronic configuration to the J state must be compatible with the experimentally observed features i.e. a reduced bond length in the upper state compared to that in the ground state, a parallel transition moment, and the observed term value. The excitation must also obey the symmetry selection rules for single photon excitation in diatomic molecules namely: $g \leftrightarrow u$, $+ \leftrightarrow +$, and $- \leftrightarrow -$. The ground state configuration of the dimer is:

$$[Ar][Ar]\ 3d\sigma_g^2\ 3d\pi_u^4\ 3d\delta_g^4\ 3d\delta_u^4\ 3d\pi_g^4\ 3d\sigma_u^2\ 4s\sigma_g^2. \quad [5]$$

In Hunds case (a) coupling of the angular momentum of the atoms this gives rise to the single term $^1\Sigma_g^+$, thus fixing the upper state as $^1\Sigma_u^+$, due to the spin selection rule $\Delta S = 0$.

By making use of the assignments of the excited states lying in the visible region two plausible excitations for the J ← X transition emerge. The main difference between the J state and those that have previously been rotationally analysed, is the marked reduction in the bond length relative to the ground state. The other states involve $4s\sigma_g \rightarrow 4s\sigma_u$ (B state) or $3d\pi_g \rightarrow 4s\sigma_u$ (A and C states) promotions [39] [46], both of which populate the $4s\sigma_u$ antibonding molecular orbital. The A ← X and C ← X transitions remove one of the antibonding $3d\pi_g$ electrons but the population of the $4s\sigma_u$ molecular orbital with this electron obviously outweighs any effect of opening up the d - shell, the 4sσ bond being reduced effectively to a one electron bond. Armed with this knowledge it was possible to narrow the excitation responsible for the observed spectrum to two plausible candidates:

$$3d\pi_g^* \rightarrow 4p\pi_u$$

or

$$3d\sigma_u^* \rightarrow 4p\sigma_g$$

Both of these are $\Delta\Lambda = 0$, parallel transitions which will dissociate adiabatically to one ground state ^2S atom and 1 excited state atom with the electron configuration $3d^9\ 4s^1\ 4p^1$. The excited state atom is postulated to be a ^2P atom for the reasons outlined below. Both promotions will open up the d - shell which is expected to favour a decrease in bond length, as the repulsion between the previously filled d - shells of the atoms will be reduced. The promotion to the 4p shell avoids populating the $4s\sigma^*$ molecular orbital which, as the lower excitations have shown, leads to an increase in bond length. The

optimum bond length for 4pσ overlap is longer than for the 4sσ bond due to the more diffuse nature of the 4p orbitals relative to the 4s orbitals ($<R_{4p}>/<R_{4s}> \simeq 1.23$ [40]) creating maximum overlap at a greater distance. The overlap of the 4pπ orbitals however will increase as the bond length shortens below the 4sσ length, and for this reason the first of the above excitations was thought to be the most likely one to give rise to the J state. This is supported by the SCF-Xα-SW calculations of Ozin et. al. [2] and other calculations by Anderson [9] (see below), who predict that the energy of the $4p\sigma_g$ molecular orbital will increase, whereas the energy of the $4p\pi_u$ molecular orbital will decrease when the bond length contracts. This excitation can be viewed in a simple manner as the transfer of an electron from the $3d\pi_g$ anti - bonding orbital into the $4p\pi_u$ bonding orbital, with an expected increase in bonding and decrease in bond length.

An alternative way to view the molecular transition is as an atomic 3d → 4p transition in one of the atoms comprising the dimer [38]. This means that the transition can be assigned on the basis of the allowed 1 photon transitions from the ground state of the copper atom. Due to the $\Delta S = 0$ and $\Delta L = 1$ atomic selection rules [45] for single photon processes, these will all lead to ^2P states upon excitation of the ^2S ground state. The lowest ^2P term of the atom which has the required electronic configuration ($3d^9\ 4s^1\ 4p^1$) to give either of the above excitations is at 45821 cm^{-1} (see table 5.7 [44]). This atomic transition energy is 8381 cm^{-1} greater than the reported T_e value for the J state of 37440 cm^{-1} [23].

Table 5.7
Lowest ^{2}P and ^{2}D atomic limits for copper

Config.	Term	J	Energy / cm^{-1}
$3d^{10}$ 4s	^{2}S	1/2	0.000
$3d^9$ $4s^2$	^{2}D	5/2	11202.565
		3/2	13245.423
$3d^{10}$ 4p	^{2}P	1/2	30535.302
		3/2	30783.686
$3d^9$ 4s(^{3}D) 4p	^{2}P	1/2	45821.00
		3/2	45879.311
$3d^9$ 4s(^{3}D) 4p	^{2}D	3/2	46172.842
		5/2	46598.34

These are taken from reference [44]

Table 5.8
States arising from the lowest atomic asymptotes of the group 1B metals in Hunds' case (a) and (c) coupling

Atomic states	Hunds' Case (a) L + S	Hunds' Case (c) *j,j*
$^2S + {}^2S$	$^1\Sigma^+, {}^3\Sigma^+$	$0^+, 0^-, 1$
$^2S + {}^2P$	$^1\Sigma^+, {}^1\Pi, {}^3\Sigma^+, {}^3\Pi$	$0^+, 0^+, 0^-, 0^-, 1, 1, 1, 2$
$^2S + {}^2D$	$^1\Sigma^+, {}^1\Pi, {}^1\Delta, {}^3\Sigma^+, {}^3\Pi, {}^3\Delta$	$0^+, 0^+, 0^-, 0^-, 1, 1, 1, 1, 2, 2, 2, 3$

All of the above terms exist as g and u pairs for homonuclear species (e.g. $^{63}Cu_2$, $^{65}Cu_2$, $^{107}Ag_2$, and $^{109}Ag_2$).

This difference is due to the change in energy of the two molecular orbitals ($3d\pi_g$ and $4p\pi_u$) as the internuclear distance decreases in the formation of the dimer. Theoretical calculations [2], [9] show that the $3d\pi_g$ orbital increases in energy with respect to the 3d atomic orbitals, whilst the $4p\pi_u$ orbital decreases in energy with respect to the 4p atomic orbitals. This will give a reduction in the spacing between the two molecular orbitals compared to that between the two atomic orbitals.

Taking the above factors into account it is proposed that the assignment of the J ← X transition is $3d\pi_g \rightarrow 4p\pi_u$. There will be a certain amount of mixing with other electronic configurations, in particular the $4p\sigma$. This will be especially important as the bond length increases towards dissociation.

Confirmation of this assignment of the J state was not possible on the analysis of this state alone and must wait for analysis of neighbouring systems or further theoretical work. The assignment in Hunds' case (a) notation is $^1\Sigma_u^+$, but the observation of another Σ - Σ transition arising from the same atomic limits would require that Hunds' case (c) coupling be invoked to rationalise the observed spectra, as the $^2S + ^2P$ limit gives rise to only one $^1\Sigma_u^+$ state. In this case the state symmetry would be described as 0_u^+ arising from *j,j* coupling of the total angular momentum of the two atoms. The terms arising from case (a) and case (c) coupling of a ^2S atom with either a ^2P or a ^2D atom are given in table 5.8, which shows there are two 0_u^+ states derived from the $^2S + ^2P$ atoms. In case (c) coupling additional atomic asymptotes which give rise to 0_u^+ states can be considered. In this case it is the total spin and orbit angular momentum (Ω) which is governed by the selection rule $\Delta\Omega = 0, \pm 1$. This coupling case allows

transitions to case (a) triplet states (e.g. $^3\Pi(0_u^+)$) thus increasing the number of possible excitations from the ground state. These states can be derived from atomic transitions forbidden by the $\Delta L = 1$ selection rule, which become allowed in the dimer due to the uncoupling of the orbital angular momentum from the internuclear axis in case (c). The most likely atomic state to act in this manner is the ^2D, which as shown in table 5.8 gives rise to two 0_u^+ states when coupled with a ^2S ground state atom. It seems unlikely that the J state is derived from the $^2S + {}^2D$ limit in view of the fact that the J state was one of the stronger transitions observed by Powers et. al. [23]. The strength of this molecular transition will be obtained from an allowed $^2S \rightarrow {}^2P$ excitation of one of the atoms comprising the dimer. A $^2S \rightarrow {}^2D$ excitation of one of the atoms is formally forbidden, and would reduce the strength of the molecular transition at longer bond lengths near the dissociation limit. The difference between the two cases is not expected to be marked for the low vibrational levels where the spin - orbit coupling makes both allowed.

5.6 Comparison of the results with theoretical predictions

To date most of the theoretical studies of the copper dimer have been concerned with the states arising from the 3d and 4s orbitals. Little attention has been paid to higher excitations.

Two studies by Ozin et. al. [2] and Anderson [9] have addressed these higher lying states. Neither of the studies takes account of any relativistic effects. Ozin used the SCF - Xα - SW method for a fixed bond length of 2.22 Å. Anderson calculated the molecular configuration and then placed the atoms on this. He

then calculated the repulsion between the two atoms to arrive at the final internuclear separation and energy.

Ozins' calculations predict an excitation energy for the $3d\pi^* \rightarrow 4p\pi$ transition of 35200 cm^{-1} while those of Anderson predict a value of 38790 cm^{-1}. Anderson predicts a bond length of 2.16 Å for the J state. As neither of these calculations takes any account of relativistic effects they are surprisingly close to the gas phase results. Relativistic effects will be expected to shorten the bond by ~0.03 Å [6], [8].

A full description of the bonding in the J state will have to take into account the interactions of 3d and 4p electrons in addition to the 4s valence electrons.

5.7 Conclusion

The J state of copper dimer observed by Powers et. al. [23] has been rotationally analysed and determined to have the symmetry 0_u^+. The equilibrium bond length is shorter than that of the ground state, pointing to a more highly bound state, caused by promotion of an electron from a $3d\pi_g$ orbital to a $4p\pi_u$ orbital. The state is assigned to the $^1\Sigma_u^+$ state derived from the $^2S + ^2P$ atomic limit at $D_e(X) + 45821$ cm^{-1}.

References

[1] Witko M., Beckmann H.O., Mol. Phys., **47**, p 945, (1982)

[2] Ozin G.A., Huber H., McIntosh D., Mitchell S., Norman J.G., Noodleman L., J. Am. Chem. Soc., **101**, p 3504, (1979)

[3] Bauschlicher C.W., Walch S.P., Siegbahn P.E.M., J. Chem. Phys., **78**, p 3347, (1983)

[4] Bauschlicher C.W., Walch S.P., Siegbahn P.E.M., J. Chem. Phys., **76**, p 6015, (1982)

[5] Joyes P., Leleyter M., J. Phys (B), **6**, p 150, (1973)

[6] Walch S.P., Bauschlicher C.W., *Theoretical Studies of Transition Metal Dimers*, Comparison of *ab initio* Quantum Chemistry with Experiment for Small Molecules; Ed R.J. Bartlett, D. Reidel Publ. Co., Holland (Dordrecht), 1985.

[7] Shim I., Gingerich K.A., J. Chem. Phys., **79**, p 2903, (1983)

[8] Ziegler T., Snijders J.G., Boerends E.J., J. Chem. Phys., **74**, p 1271, (1981)

[9] Anderson A.B., J. Chem. Phys., **68**, p 1744, (1978)

[10] Miyoshi E., Tatewaki H., Nakamura T., J. Chem. Phys., **78**, p 815, (1983)

[11] Martin R.L., J. Chem. Phys., **78**, p 5840, (1983)

[12] Schissel P., J. Chem. Phys., **26**, p 1276, (1957)

[13] Gole J.L., English J.H., Bonbybey V.E., J. Phys. Chem., **86**, p 2560, (1982)

[14] Kolb D.M., Rotermund H.H., Schrittenlacher W., Schroeder W., J. Chem. Phys., **80**, p 695, (1984)

[15] Bondybey V. E., English J. H., J. Chem. Phys., **77**, p 3771, (1982)

[16] Aslund N., Barrow R.F., Richards W.G., Travis D.N., Ark. Fys., **30**, p 171, (1965)

[17] Steele R.E., J. Mol. Spec., **61**, p 477, (1976)

[18] Preuss D.R., Pace A., Gole J.L., J. Chem. Phys., **71**, p 3553, (1971)

[19] Grinter R., Armstrong S., Jayasooriya U.A., McCombie J., Norris D., Springall J.P., Faraday Symp., **14**, p 94, (1980)

[20] Lochet J., J. Phys (B), **11**, p L55, (1978)

[21] Bondybey V.E., Schwartz G.P., English J.H., J. Chem. Phys., **78**, p 11, (1983)

[22] Powers D.E, Hansen S.G., Geusic M.E., Pulu A.C., Hopkins J.B., Dietz T.G., Duncan M.A., Langridge-Smith P.R.R., Smalley R.E., J. Phys. Chem., **86**, p 2556, (1982)

[23] Powers D.E., Hansen S.G., Geusic M.E., Michalopoulos D.L., Smalley R.E., J. Chem. Phys., **78**, p 2866, (1983)

[24] McCaffrey J.G., Bennett R.R., Morse M.D., Breckenridge W.H., J. Chem. Phys., **91**, p 92, (1989)

[25] Zheng L.S., Korner C.M., Brucat P.J., Yang S.M., Pettiette C.L., Craycraft M.J., Smalley R.E., J. Chem. Phys., **85**, p 1671, (1986)

[26] Michalopoulos D.L., Geusic M.E., Hansen S.G., Powers D.E., Smalley R.E., J. Phys. Chem., **86**, p 3941, (1982)

[27] Hull A.W., Phys. Rev., **14**, p 540, (1919)

[28] Weltner W., van Zee R.J., Ann. Rev. Phys. Chem., **35**, p 291, (1984)

[29] Rholfing E.A., Valentini J.J., J. Chem. Phys., **84**, p 6560, (1984)

[30] Badger R.M., J. Chem. Phys., **2**, p 128, (1934)

[31] Badger R.M., J. Chem. Phys., **3**, p 710, (1935)

[32] Moskovits M., DiLella D.P., Limm W., J. Chem. Phys., **80**, p 626, (1984)
[33] Weisshaar J.C., J. Chem. Phys., **90**, p 1429, (1989)
[34] Haliday D., Resnick R., *Physics*, John Wiley, New York, 1978.
[35] Bevington P.R., *Data Reduction and Error Analysis for the Physical Sciences*, McGraw - Hill, New York, 1969.
[36] Herzberg G., *Spectra of Diatomic Molecules*, Van Nostrand Reinhold, New York, 1950.
[37] Hollas J.M., *High Resolution Spectroscopy*, Butterworth, London, 1982.
[38] Lawley K.P., *Private Communication*,
[39] Cartwright P.C., *PhD Thesis*, Edinburgh University, 1989.
[40] Slater J.C., *Quantum Theory of Atomic Structure Vol. 1*, McGraw - Hill, New York, 1960.
[41] Johnson P.M., Otis C.E., Ann. Rev. Phys. Chem., **32**, p 139, (1981)
[42] Moskovits M., Hulse J.E., J. Chem. Phys., **67**, p 4271, (1977)
[43] Huber K.P., Herzberg G., *Constants of Diatomic Molecules*, Van Nostrand Reinhold, New York, 1979.
[44] Moore C.E., *Atomic Energy Levels, Vol. II*, U.S. Department of Commerce, National Bureau of Standards, Washington, 1952.
[45] Herzberg G., *Atomic Spectra and Atomic Structure*, Dover Publications, New York, 1944.
[46] Morse M.D., Chem. Rev., **86**, p 1053, (1986)
[47] Savitzky A., Golay M.J.E., Anal. Chem., **36**, p 1627, (1964)

Chapter 6
High Resolution Electronic Spectroscopy of the A ← X System of Ag_2

6.1 Introduction to the electronic spectroscopy of Ag_2.

Theoretical studies of the bonding and electronic structure of silver dimer have proceeded in parallel with those of copper [1] - [5], [29], but as yet there has been no direct experimental determination of the bond lengths of any of the known electronic states. Table 6.1 summarises the spectroscopic constants of the known electronic states of silver dimer and figure 6.1 shows the RKR curves for these states. The A and X states are shown as full curves as they include the rotational constants derived in this work. The other states are shown as dashed curves to indicate that no rotational analyses are available with which to fix the bond length. This lack of experimental data is in part due to the techniques previously employed which measured the emission from or absorption by samples containing all three isotopomers formed from the two naturally occurring isotopes of silver. Superposition of the spectra arising from the different isotopomers causes severe congestion, precluding any reliable assignment of the rotational structure. Allied to this is an expected reduction in the spacing between the rotational lines caused by the decrease in the rotational constant as given by the standard expression for a rigid rotor [32]:

$$B_e = h / (8\pi^2 c\mu R_e^2) \qquad (6.1)$$

Table 6.1
Spectroscopic constants of the known electronic states of Ag_2

	T_e / cm^{-1}	ω_e / cm^{-1}	$\omega_e x_e$ / cm^{-1}
$H(0_u^+)$	58273.1	166.7	2.48
$E(0_u^+)$	40159.4	146.2	1.55
$D\ 0_u^+$	39014.5	169.0	1.21
$C\ 1_u\ ^1\Pi_u$	37631.3	171.4	0.91
$B(0_u^+)$	35835.6	152.5	0.88
$A\ 0_u^+$	22996.4	155.3	0.59
$X\ ^1\Sigma_g^+$	0	192.4	0.60

This table is taken from reference [14].
Uncertain assignments are given in brackets.
The results of this work are given in table 6.8.

Figure 6.1
Known electronic states of Ag_2 and low lying atomic asymptotes

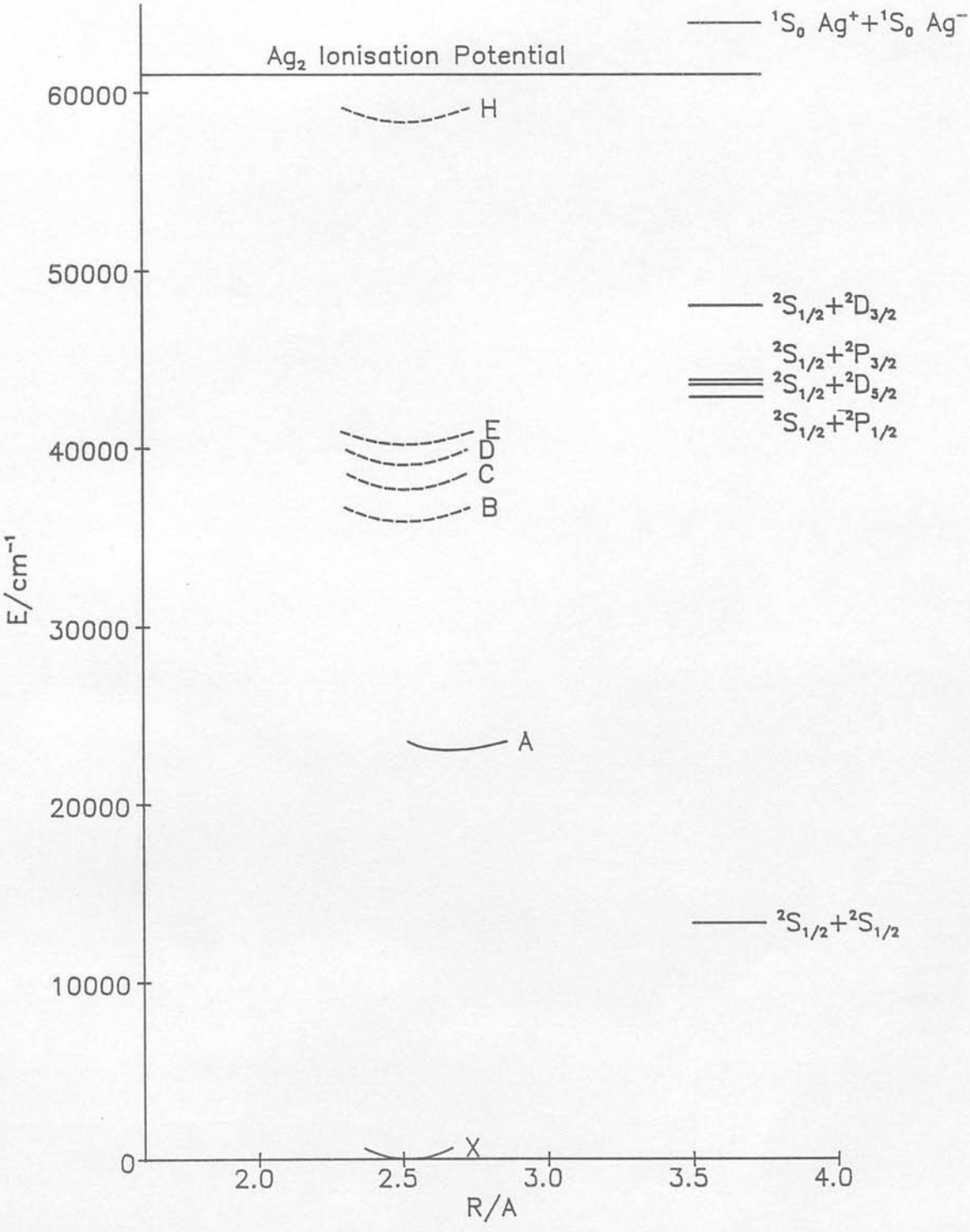

Equation (6.1) shows that increasing the mass or the bond length will result in a decrease in the rotational constant. Compared to copper in the first row, silver is heavier and will be expected to have a longer bond length due to the increase in the principal quantum number. Despite this the main reason that rotational analysis of the recorded spectra has proved intractable in the past has been the mixture of isotopes present. The abundances of the two naturally occuring isotopes ^{107}Ag (52%) and ^{109}Ag (48%) give a ratio of ~1:2:1 for the three isotopomers of the dimer. The nearly equal abundance of all three isotopomers means that the overlaid spectra cannot be separated out by means of the relative intensities of the different isotopomers. Spectra of Au_2, the next member of the group, have been recorded using the same hot oven techniques employed for Ag_2. These spectra have been rotationally analysed despite gold being heavier than silver, and having a correspondingly smaller rotational constant [28]. It has the advantage of only one naturally occurring isotope, resulting in much less congested spectra.

With the significance of small silver clusters in many important processes such as photography [29] - [31] and catalysis [33], [34] information on their physical and electronic structure is of great interest. The obvious starting point for a detailed understanding of the electronic properties of small clusters is the dimer.

The spectrum of silver dimer was first reported by Ruamps [15] in 1954 in emission from a King furnace. This and later work by Kleman and Lindkvist [16] gave vibrational constants for the A and X states. Other workers have investigated the emission and absorption spectra of silver dimer in King furnaces

[17] - [20], electric discharges [21], and cryogenic matrices [22] - [24] to determine vibrational constants and electronic term values for the B, C, D, E, and H states. The spectroscopic constants determined in these studies are given in table 6.1 [14]. The assignments of the state symmetry are based on the observed shape of the vibrational bands.

Sradnov and Pesic [20] estimated the rotational constants for the ground and C states from the position of the Q and R branch heads observed in the vibrational spectrum of the C ← X system. This was carried out using a ground state B_e value determined from an interpolation between the B_e values of Cu_2 and Au_2. This procedure gave the following constants for the ground state; B_e = 0.05121 cm^{-1}, α_e = 0.000132 cm^{-1}, and R_e = 2.48 Å.

Many theoretical methods have been used to model silver dimer. These calculations have been hindered by the lack of experimentally derived values for the bond lengths and state symmetries. Both relativistic and non - relativistic calculations have been carried out and they point to a relativistic contraction of ~ 0.15 Å [4], in agreement with the 0.08 Å relativistic contraction of the 5s orbital on the silver atom [25]. This compares with a relativistic contraction of ~ 0.03 Å for the lighter copper dimer. Interaction of the d - orbitals is expected to be greater in silver dimer as they are less contracted with respect to the s - orbital than in Cu_2 ($<R_{5s}>/<R_{4d}>$ = 2.67, $<R_{4s}>/<R_{3d}>$ = 3.36 [11]). In unpublished work described below Hopkins and co - workers [14] [26] determined the ionisation potential of silver dimer to be the same as that of the atom to within experimental error. From this they concluded that the binding energy of the ion was similar to that of the neutral and therefore the s- electrons

did not play a large part in the bonding (assuming an s - electron was ejected upon ionisation). It is interesting to note that the dissociation energies for Ag_2 and its alkali metal counterpart Rb_2 (1.66 eV and 0.49 eV) show a smaller difference than that between Cu_2 and K_2 (2.05 eV and 0.514 eV) in the previous row. This may point to a lesser contribution by the d orbitals to the bonding in the 2nd row compared to the 1st row. To further the description of the electronic structure of silver dimer it is necessary to rotationally resolve the electronic spectra. Rotational analysis of these systems will give the spin multiplicity, state symmetry, and bond length of the ground and excited electronic states.

To date the laser vaporisation / supersonic beam technique with mass-resolved detection, as used in the present work, has been used only once previously in the investigation of silver dimer. The technique is well suited to the study of Ag_2, particularly with regard to resolution of the rotational structure in the spectra, as the mass selectivity removes the spectral congestion caused by superposition of the different isotopomers. When combined with the cooling achieved in the supersonic expansion, the recorded spectra become much simpler to assign and analyse.

The previous use of this technique was in a limited investigation of the vibrational structure of the A state by Hopkins et. al. [26] in which they determined the ionisation potential of the dimer. Ionisation of the excited dimer was accomplished using the fourth harmonic of a Nd:YAG laser (266 nm, 4.66 eV.). This proved insufficient to single photon ionise vibrational levels below $v' = 3$ of the A state. The ionisation potential of the dimer was therefore fixed as

lying between the energy of the v' = 2 and v' = 3 levels of the A state plus that of the fourth harmonic of the Nd:YAG laser. The value reported was 7.56±0.02 eV [14]. The object of the work presented here was to rotationally resolve the lowest vibrational bands of the A ← X system of silver dimer using the techniques and apparatus introduced in chapters 2 and 3.

6.2 Spectroscopic investigation of the A ← X system of Ag_2

The A ← X system of cold silver dimer contained in a supersonic molecular beam was investigated using resonant two photon ionisation (R2PI) spectroscopy with mass resolved detection. The dimer was formed by condensation from a plasma generated by laser vaporisation of a 5 mm diameter silver rod (Johnson Matthey Specpure grade) in the throat of a pulsed supersonic nozzle (see chapter 2). The resultant molecular beam was crossed by the output of a Lambda Physik 3002EC excimer pumped high resolution tunable dye laser and a Lumonics excimer laser operating on ArF (193 nm). The fixed frequency ArF excimer laser was used for the ionisation step as the A state (T_e = 22996.4 cm^{-1}) lay less than half way to the ionisation threshold (I.P. = 60871.4 cm^{-1} [14]), requiring the second photon for R2PI to be more energetic than the first. The dye laser was operated on Coumarin 120 (Lambdachrome 4400, 423 - 462 nm, peak = 441 nm). The output of the ArF laser was attenuated by insertion of wire gauze in the beam to increase the contrast between the resonant signal and the non - resonant background. Synchronisation between the timing of the two lasers was achieved by directing part of each beam onto a photodiode, the output of which was fed into an

oscilloscope. The temporal overlap of the light pulses was then maintained by adjusting the delay between the lasers via the function keys on the keyboard of the computer used to control the experiment (see chapter 3), whilst monitoring the output of the photodiodes with the oscilloscope. Maintaining the temporal overlap of the lasers was the main practical problem during this work, the short lifetime of the A state compounded the problem (see section 6.4). The spectra presented in this chapter are the result of summing 60 shots at each laser wavelength throughout the scan range. Smoothing of the spectra has been carried out using ODIN as described in chapter 3.

Figure 6.2 shows the vibronic R2PI spectra of all three isotopomers, $^{107}Ag_2$, $^{107}Ag^{109}Ag$, and $^{109}Ag_2$ recorded at 1.56 cm^{-1} per step for the first four vibrational levels of the A state. No hot bands were visible, showing that the cooling in the supersonic expansion had reduced the vibrational population to a single level in the electronic ground state. The energy scale along the X - axis was obtained from the readout of the 3002EC dye laser and was not calibrated to any absolute wavelength. Despite this the positions of the bands and the vibrational constant (ω_e) calculated for $^{107}Ag_2$ (υ_{00} = 22985.4 cm^{-1}, ω_e = 154 cm^{-1}) are in good agreement with those obtained using the data presented in table 6.1 and the previously reported υ_{00} energy of 22977.5 cm^{-1} [16]. The (0 - 0) and (1 - 0) bands were recorded with a smaller laser step size (0.1 cm^{-1}) to observe the shape of the bands and the separation between the isotopomers. The recorded spectra (figures 6.3 and 6.4) show red degraded P and R branches with no evidence of a Q branch, indicating a parallel transition, with the upper state having a longer bond length than the ground state.

Figure 6.2
R2PI spectra of Ag_2 A ← X (v' - 0)

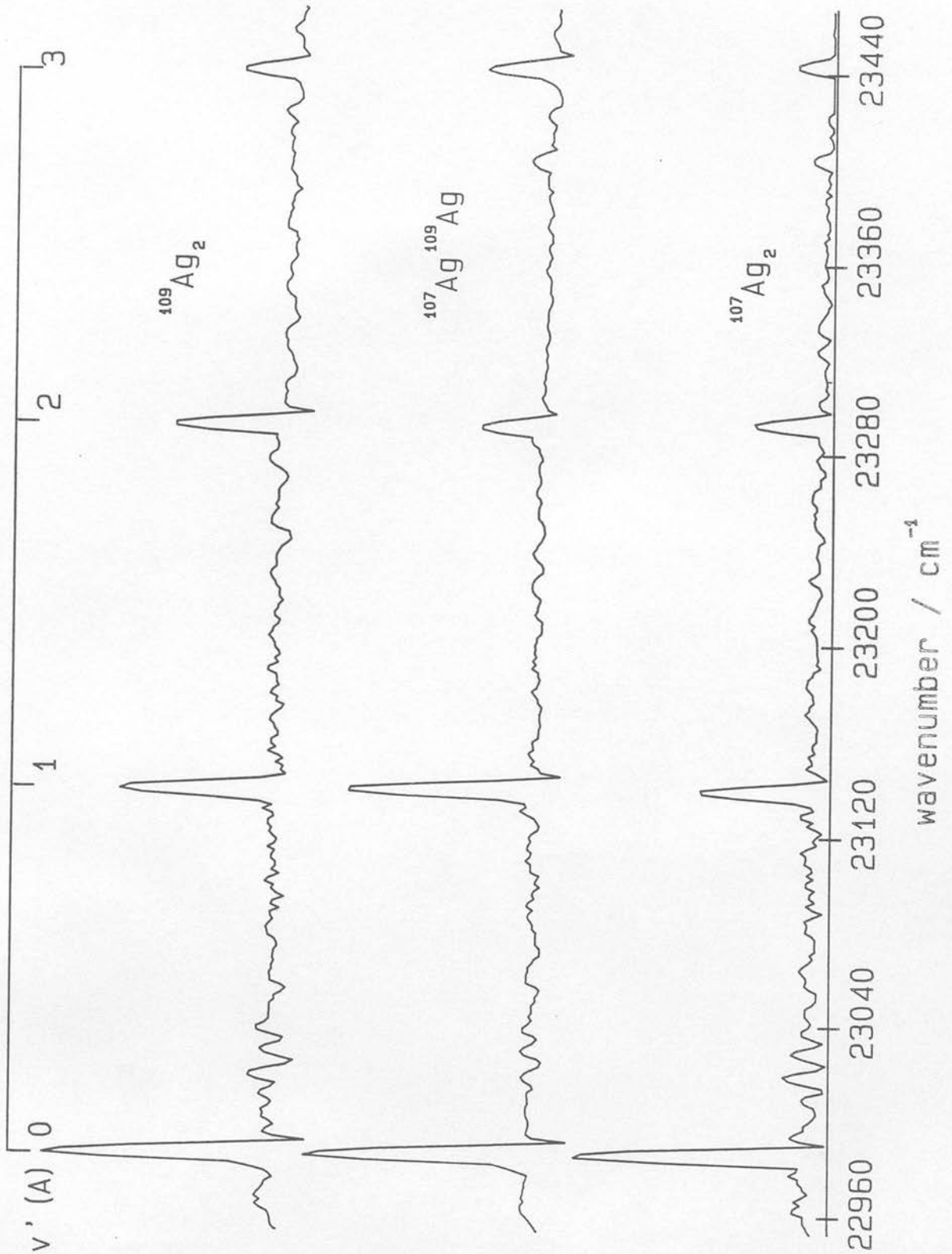

Figure 6.3 Low resolution R2PI spectra of the
$A \leftarrow X$ (0 - 0) band of Ag_2

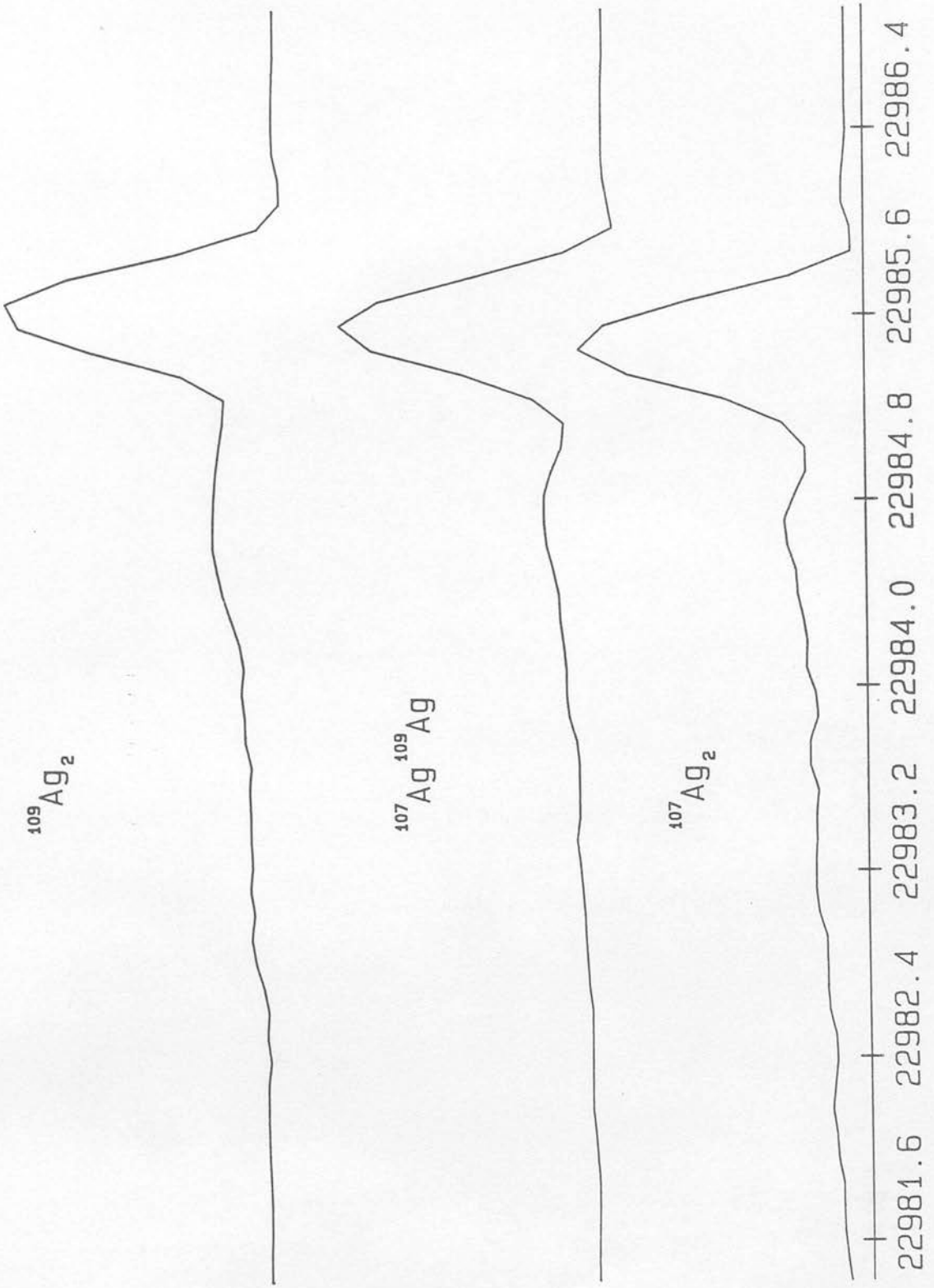

Figure 6.4 Low resolution R2PI spectra of the
$A \leftarrow X$ (1 - 0) band of Ag_2

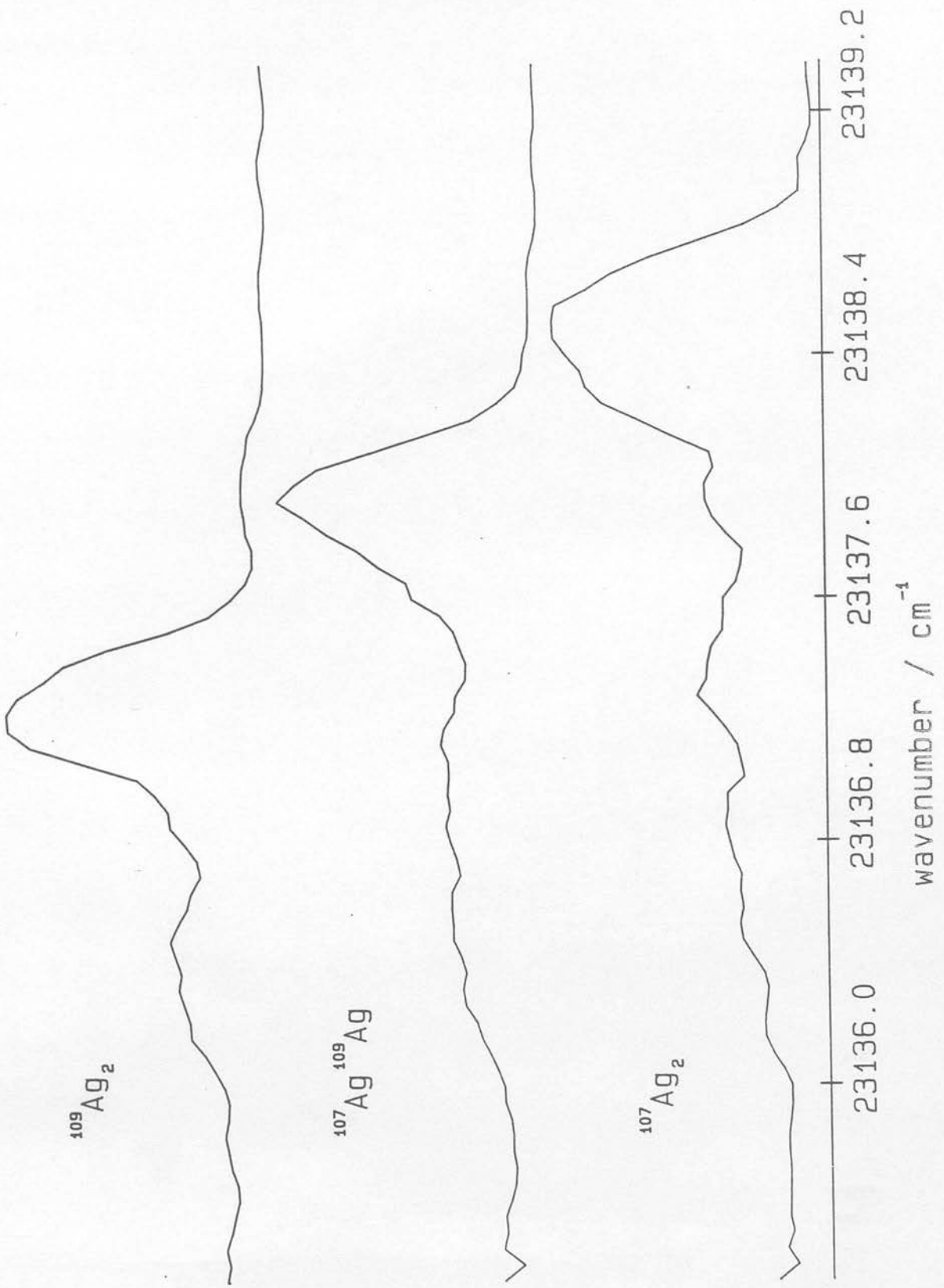

High resolution R2PI spectra of the (0 - 0) and (1 - 0) bands were recorded with the use of an intra - cavity etalon in the 3002EC to narrow the bandwidth to 0.04 cm^{-1} (see section 2.5.3). The line narrowed output obtained with this etalon allowed the (0 - 0) and (1 - 0) bands to be recorded at rotational resolution. The high resolution spectra recorded for these bands are shown in figures 6.5(a) - 6.8(a) for both the homonuclear $^{107}Ag_2$ and heteronuclear $^{107}Ag^{109}Ag$ species. The $^{109}Ag_2$ spectra are not shown as they were identical in appearence to those of $^{107}Ag_2$. Concurrent recording of the interference fringes generated by directing part of the dye laser output through a confocal monitor etalon (Lambda Physik FL54, FSR = 0.1 cm^{-1}, finesse = 25) provided an accurate relative wavelength calibration. No absolute energy calibration was carried out as the rotational constants were determined from the relative positions of the lines in the spectra.

6.3 Rotational analysis of the high resolution spectra of Ag_2 A ← X

The analysis of the high resolution spectra was carried out using programs written in C and FORTRAN on an IBM PC - AT and the EMAS mainframe (NAS VL60) at Edinburgh. The ODIN program described in chapter 3 was used on the PC - AT to smooth the data and interpolate the position of the rotational lines and etalon fringes. ODIN was also used to determine the coefficients of a polynomial fit of the etalon fringe spacing, in bin numbers [3], to the known free spectral range (0.1 cm^{-1}).

---

[3] A bin corresponds to one step of the laser

Figure 6.5 High resolution R2PI spectrum of the $A \leftarrow X$ (0 - 0) band of $^{107}Ag_2$

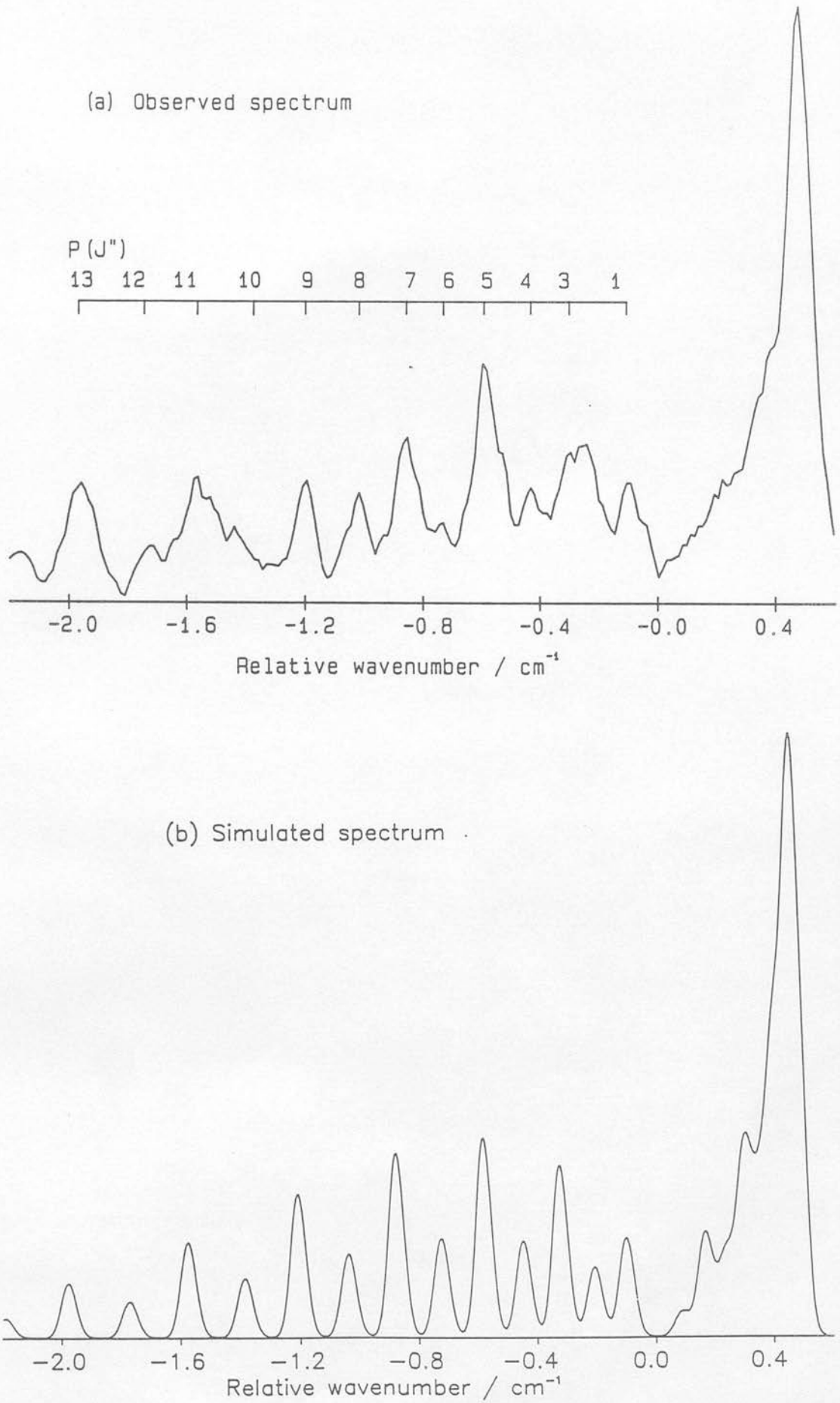

Figure 6.6 High resolution R2PI spectrum of the A ← X (0 - 0) band of $^{107}Ag^{109}Ag$

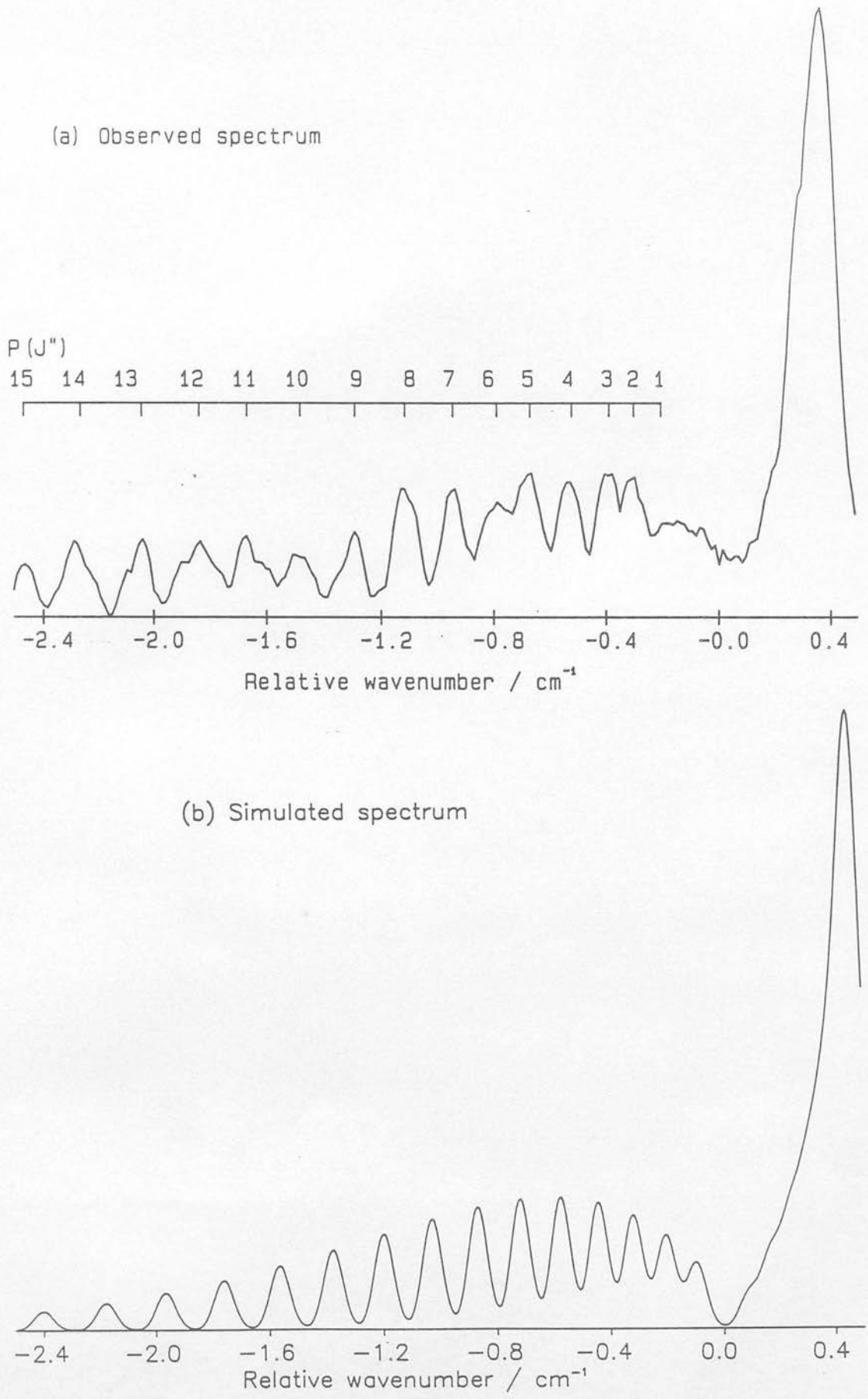

Figure 6.7 High resolution R2PI spectrum of the $A \leftarrow X$ (1 - 0) band of $^{107}Ag_2$

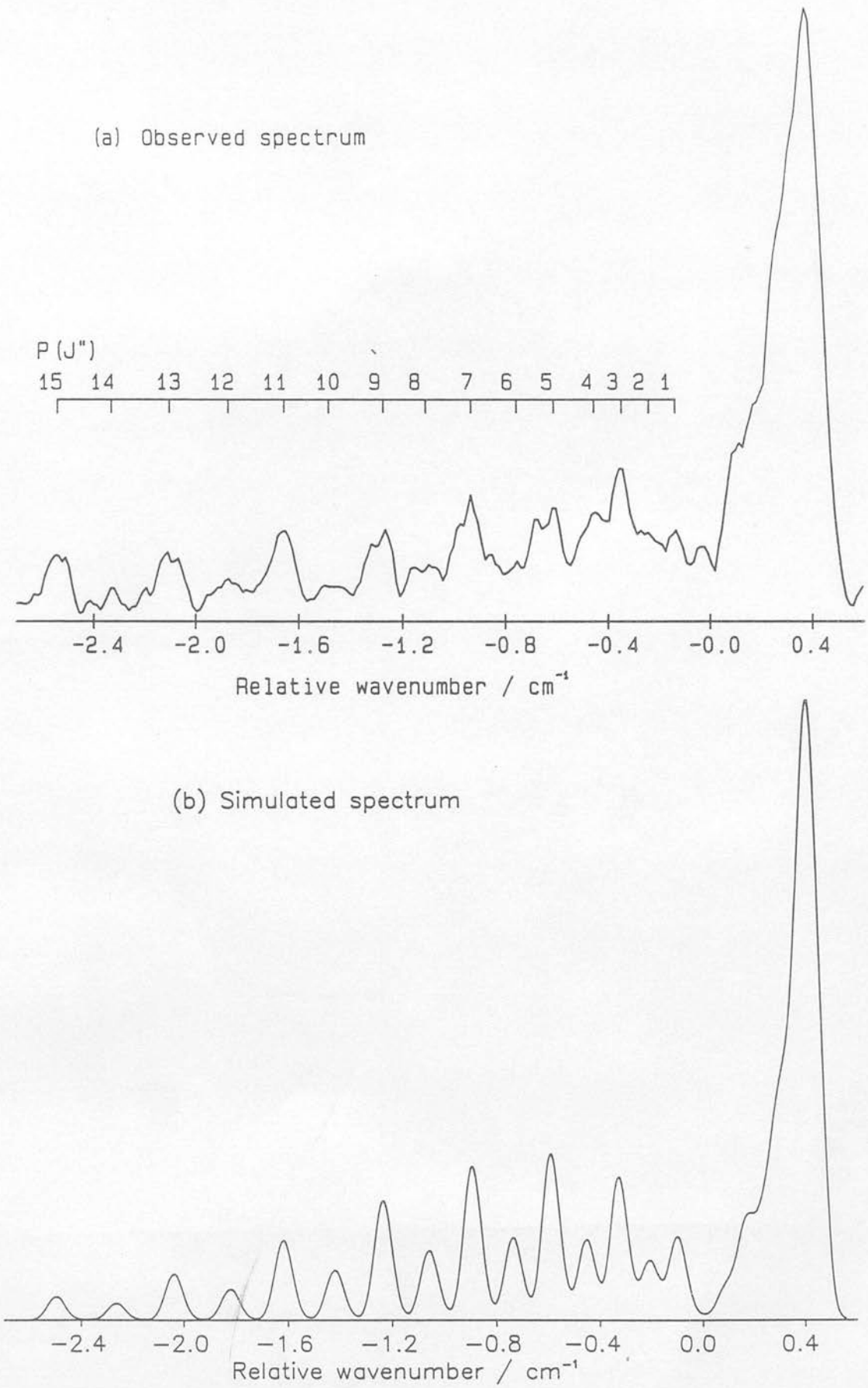

Figure 6.8 High resolution R2PI spectrum of the $A \leftarrow X$ (1 - 0) band of $^{107}Ag^{109}Ag$

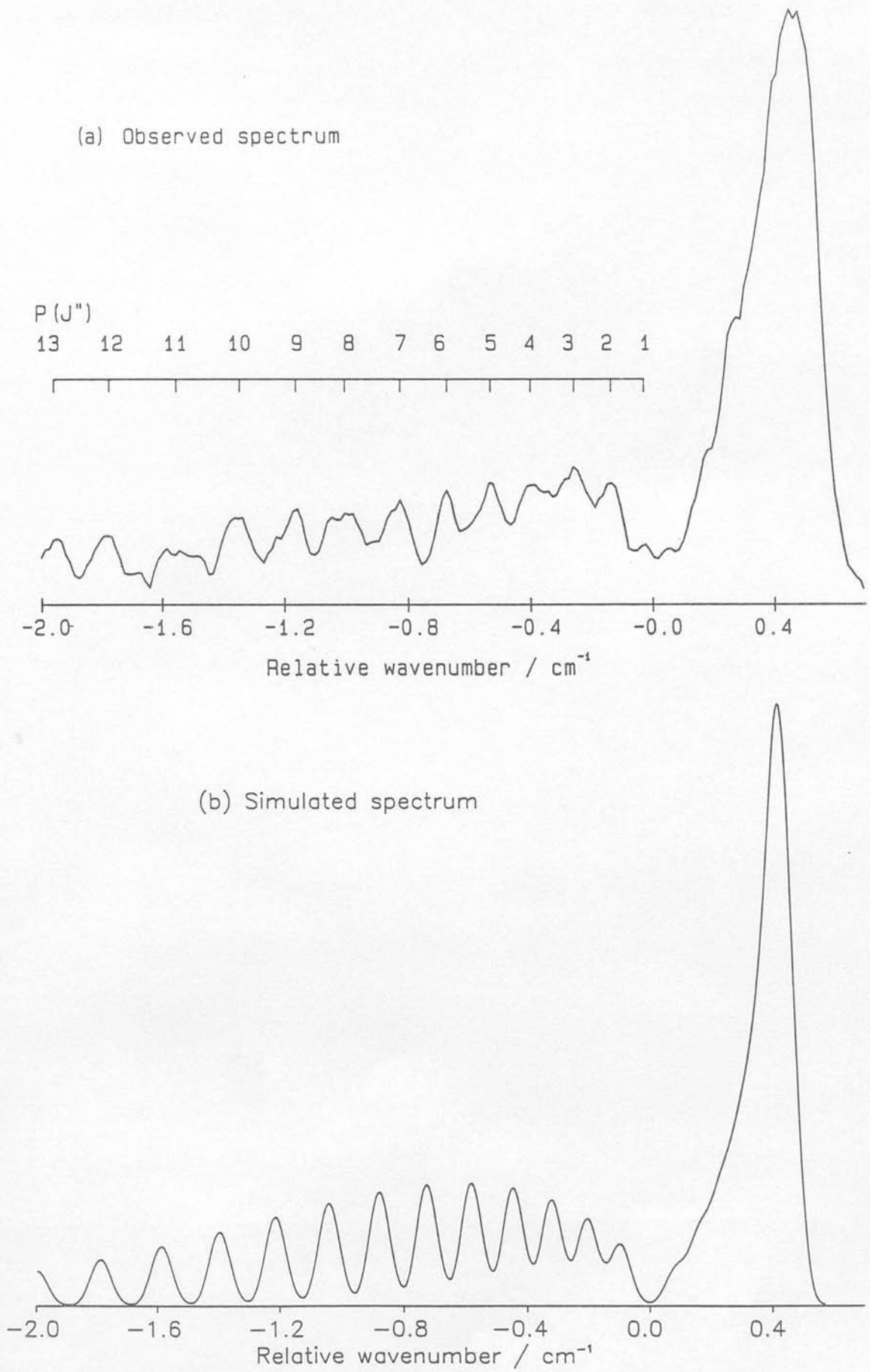

Smoothing and peak finding was carried out using the method of Savitzky and Golay [35] (see chapter 3). The line positions were determined relative to an arbritary zero, usually the first point in a scan. The distance from this zero in bin numbers was converted to wavenumbers using the conversion factors obtained from the least mean squares fit to the etalon fringes. The interpolated peak positions and the coefficients of the polynomial were output to character files and transferred to the mainframe. The errors quoted throughout the following discussion are derived from twice the statistical standard deviation found from a fit of the unweighted line positions.

The rotational line positions for each isotopomer within a given vibronic band were fitted to the functions:

$$E_P = B_v'J''(J''-1)-D_v'(J''(J''-1))^2+\ldots\ldots - B_v''J''(J''+1)+D_v''(J''(J''+1))^2-\ldots\ldots \quad (6.2)$$

$$E_R = B_v'(J''+1)(J''+2)-D_v'((J''+1)(J''+2))^2+\ldots\ldots - B_v''J''(J''+1)+D_v''(J''(J''+1))^2-\ldots\ldots \quad (6.3)$$

where:

$E_{P/R}$ = relative line position in cm^{-1}.

J' / J" = upper / lower state rotational level.

Due to the lack of any readily assignable structure in the R branch of the spectra initial constants were obtained by fitting the P branch lines alone.

Table 6.2
Observed and calculated line positions and rotational constants for the A ← X (0 - 0) band of $^{107}Ag_2$

Branch	J"	Obs. / cm^{-1}	Calc. /cm^{-1}	Resid. / cm^{-1}
P	13	-1.973	-1.978	0.005
P	11	-1.574	-1.574	0.000
P	9	-1.215	-1.207	-0.008
P	8	-1.036	-1.037	0.001
P	7	-0.874	-0.876	0.002
P	5	-0.605	-0.580	-0.025
P	4	-0.448	-0.446	-0.002
P	3	-0.271	-0.321	0.050
P	1	-0.120	-0.098	-0.022
R	7	0.458	0.459	-0.001

Reduced $\chi^2 = 0.0005$

Floating both upper and lower state constants ⇒

$B_0'' = 0.0490(15)\ cm^{-1}$

$B_0' = 0.0444(17)\ cm^{-1}$

With ground state $B_0 = 0.0490\ cm^{-1}$ (gives calculated positions and residuals above):

$A_0 = 2.3540(207)\ cm^{-1}$

$B_0' = 0.0445(3)\ cm^{-1}$

$R_0 = 2.655(9)Å$

Table 6.3
Observed and calculated line positions and rotational constants for the A ← X (0 - 0) band of $^{107}Ag^{109}Ag$

Branch	J"	Obs. / cm^{-1}	Calc. /cm^{-1}	Resid. / cm^{-1}
P	15	-2.375	-2.402	0.027
P	14	-2.195	-2.179	-0.016
P	13	-1.957	-1.965	0.008
P	12	-1.750	-1.760	0.010
P	11	-1.587	-1.564	-0.023
P	10	-1.400	-1.377	-0.023
P	9	-1.207	-1.198	-0.009
P	8	-1.030	-1.029	-0.001
P	7	-0.859	-0.869	0.010
P	6	-0.698	-0.718	0.020
P	5	-0.595	-0.576	-0.019
P	4	-0.449	-0.443	-0.006
P	3	-0.307	-0.318	0.011
P	1	-0.077	-0.097	0.020
R	7	0.445	0.454	-0.009

Reduced $\chi^2 = 0.0003$

Floating both upper and lower state constants ⇒

$B_0'' = 0.0485(11)\ cm^{-1}$

$B_0' = 0.0440(13)\ cm^{-1}$

With ground state $B_0 = 0.0486\ cm^{-1}$ (gives calculated positions and residuals above):

$A_0 = 2.4439(142)\ cm^{-1}$

$B_0' = 0.0441(1)\ cm^{-1}$

$R_0 = 2.654(3)Å$

Table 6.4
Observed and calculated line positions and rotational constants for the A ← X (0 - 0) band of $^{109}Ag_2$

Branch	J"	Obs. / cm^{-1}	Calc. /cm^{-1}	Resid. / cm^{-1}
P	15	-2.393	-2.379	-0.014
P	13	-1.921	-1.946	0.025
P	12	-1.737	-1.743	0.006
P	11	-1.559	-1.549	-0.010
P	9	-1.190	-1.187	-0.003
P	5	-0.593	-0.571	-0.022
P	3	-0.291	-0.319	0.028
P	1	-0.102	-0.096	-0.006

Reduced $\chi^2 = 0.0004$

Floating both upper and lower state constants ⇒

$B_0'' = 0.0483(64)\ cm^{-1}$

$B_0' = 0.0439(73)\ cm^{-1}$

With ground state $B_0 = 0.0482\ cm^{-1}$ (gives calculated positions and residuals above):

$A_0 = 2.5170(208)\ cm^{-1}$

$B_0' = 0.0438(2)\ cm^{-1}$

$R_0 = 2.615(6)Å$

Table 6.5
Observed and calculated line positions and rotational constants for the A ← X (1 - 0) band of $^{107}Ag_2$

Branch	J"	Obs. / cm^{-1}	Calc. /cm^{-1}	Resid. / cm^{-1}
P	15	-2.481	-2.498	0.017
P	14	-2.280	-2.263	-0.017
P	13	-2.046	-2.037	-0.009
P	12	-1.819	-1.822	0.003
P	11	-1.611	-1.616	0.005
P	9	-1.235	-1.234	-0.001
P	7	-0.899	-0.892	-0.007
P	5	-0.580	-0.588	0.008
P	3	-0.317	-0.323	0.006
P	1	-0.104	-0.098	-0.006

Reduced $\chi^2 = 0.0001$

Floating both upper and lower state constants ⇒

$B_0'' = 0.0491(32)\ cm^{-1}$

$B_1' = 0.0442(36)\ cm^{-1}$

With ground state $B_0 = 0.0490\ cm^{-1}$ (gives calculated positions and residuals above):

$A_0 = 3.3827(108)\ cm^{-1}$

$B_1' = 0.0441(1)\ cm^{-1}$

$R_1 = 2.667(3)Å$

Table 6.6
Observed and calculated line positions and rotational constants for the A ← X (1 - 0) band of $^{107}Ag^{109}Ag$

Branch	J"	Obs. / cm^{-1}	Calc. /cm^{-1}	Resid. / cm^{-1}
P	15	-2.442	-2.452	0.010
P	14	-2.229	-2.223	-0.006
P	13	-1.989	-2.002	0.013
P	11	-1.613	-1.590	-0.023
P	10	-1.400	-1.398	-0.002
P	9	-1.208	-1.216	0.008
P	8	-1.060	-1.043	-0.017
P	7	-0.882	-0.879	-0.003
P	6	-0.722	-0.725	0.003
P	5	-0.582	-0.581	-0.001
P	4	-0.443	-0.446	0.003
P	3	-0.311	-0.320	0.009
P	2	-0.196	-0.204	0.008
R	6	0.412	0.415	-0.003

Reduced $\chi^2 = 0.0001$

Floating both upper and lower state constants ⇒

$B_0'' = 0.0486(8)\ cm^{-1}$

$B_1' = 0.0439(9)\ cm^{-1}$

With ground state $B_0 = 0.0486\ cm^{-1}$ (gives calculated positions and residuals above):

$A_0 = 2.7459(88)\ cm^{-1}$

$B_1' = 0.0439(1)\ cm^{-1}$

$R_1 = 2.660(3)Å$

Table 6.7
Observed and calculated line positions and rotational constants for the A ← X (1 - 0) band of $^{109}Ag_2$

Branch	J"	Obs. / cm^{-1}	Calc. /cm^{-1}	Resid. / cm^{-1}
P	13	-1.979	-1.972	-0.007
P	12	-1.782	-1.765	-0.017
P	11	-1.551	-1.567	0.016
P	9	-1.205	-1.199	-0.006
P	8	-1.009	-1.029	0.020
P	7	-0.846	-0.868	0.022
P	6	-0.710	-0.717	0.007
P	5	-0.575	-0.574	-0.001
P	4	-0.463	-0.441	-0.022
P	3	-0.324	-0.317	-0.007
P	1	-0.101	-0.096	-0.005
R	6	0.416	0.417	-0.001

Reduced $\chi^2 = 0.0002$

Floating both upper and lower state constants ⇒

$B_0'' = 0.0480(11)\ cm^{-1}$

$B_1' = 0.0433(13)\ cm^{-1}$

With ground state $B_0 = 0.0482\ cm^{-1}$ (gives calculated positions and residuals above):

$A_0 = 2.1194(131)\ cm^{-1}$

$B_1' = 0.0436(2)\ cm^{-1}$

$R_1 = 2.657(6)$Å

The correct assignment of the spectra of the homonuclear ($^{107}Ag_2$ and $^{109}Ag_2$) species was aided by the intensity alternation between transitions originating from the odd and even rotational levels of the ground state. This alternation was due to nuclear spin statistics ($I_{Ag} = 0.5$), giving a ratio of $(I+1)/I$ (= 3:1) between the odd and even numbered J'' levels imposed on the intensity distribution derived from the Boltzmann populations of individual levels. The spectra for the heteronuclear species $^{107}Ag^{109}Ag$ (figures 6.6 and 6.8) do not show this intensity alternation as it has no centre of symmetry.

The program given in appendix C was used to fit the observed line positions to equations (6.2) and (6.3) by a least mean squares method [27]. This gave B_v values for both the upper and lower states which are listed in tables 6.2 - 6.7 together with the measured line positions. The least mean squares fit calculated an offset (A_0) for the origin of the band from the arbritary zero chosen initially. This offset has been subtracted from the observed and calculated line positions to give them as offsets from the band origin. The difference between the A_0 terms for the different isotopomers is the combined vibrational and electronic isotope shift.

In the absence of any accurately known rotational constants for either the A or X states the constants for both were floated during the least squares fit. A number of the observed lines had to be excluded due to large errors between their calculated and observed positions. The reasons for this were mainly because the shape of the peak and therefore the position of the its maximum were distorted in some manner. This arose from changes in the integrated intensity of the ion signals recorded caused by fluctuations in the temporal

overlap of the two laser pulses, leading to glitches in the recorded spectrum.

Where possible the peak of the R branch was assigned to a rotational transition using the method of combination differences to determine the ground state rotational level from the following functions:

$$B' = (E_{R,J"} - E_{P,J"}) / 2$$
$$B" = (E_{R,J"} - E_{P,J"+2}) / 2 \qquad (6.4)$$

Where $E_{P/R}$ is the position of the relevant rotational line given by the second subscript.

The values of B' and $B"$ determined by equations (6.4) were compared with those obtained by the least mean squares fit of the P - branch lines alone to determine whether the R - branch head coincided with a rotational transition.

The value of $B_0"$ for each of the isotopes was determined from the average of the lower state rotational constants calculated for the (0 - 0) and (1 - 0) bands. These values were then used to refit the (0 - 0) and (1 - 0) bands with a common ground state constant, with only the upper state constant being floated. The measured line positions, along with the calculated line positions, residuals and constants determined by this fit are given for all three isotopomers in tables 6.2 - 6.7. The values determined for B_0' and B_1' for the A state were used to calculate α_e' and B_e' by substitution into the standard expression:

$$B_v = B_e - \alpha_e(v+0.5) \qquad (6.5)$$

The constants obtained for the different isotopes were compared using the formulae for the rotational isotope shift effect [36]:

$$B_{e(i)} = \rho_i^2 B_e, \quad \alpha_{e(i)} = \rho_i^3 \alpha_e \qquad (6.6)$$

where $\rho = (\mu / \mu_i)^{1/2}$,

and μ_i is the reduced mass of the heavier isotopomer

The three isotopomers of silver dimer have reduced mass ratios of 0.9908 and 0.9816 for the $^{107}Ag_2$ / $^{107}Ag^{109}Ag$ and $^{107}Ag_2$ / $^{109}Ag_2$ pairs respectively. All the ratios of the different rotational constants determined fell within experimental error of the expected values. The ratios of the B values are only exact for the equilibrium value as the B_v values must include the α_e term which ratios as ρ^3 and not ρ^2. The ratio of the calculated B_e' values for the $^{107}Ag^{109}Ag$ / $^{107}Ag_2$ and $^{109}Ag_2$ / $^{107}Ag_2$ pairs were 0.9888(20) and 0.9821(80) respectively.

The average bond lengths of the different vibrational levels and the equilibrium bond length were calculated by substituting the appropriate rotational constants into equation (6.1). The values obtained are given in tables 6.2 - 6.7 and show a small increase for the A state over that for the ground state. The calculated spectroscopic constants, bond lengths, and isotope shifts are summarised in table 6.8.

Table 6.8
Constants derived from analysis of the (0 - 0) and (1 - 0) bands of the A ← X system of Ag_2

	$^{107}Ag_2$	$^{107}Ag^{109}Ag$	$^{109}Ag_2$
B_e' / cm^{-1}	0.0447(3)	0.0442(1)	0.0439(2)
α_e' / cm^{-1}	0.0004(2)	0.0002(1)	0.0002(1)
R_e' / Å	2.649(9)	2.651(3)	2.648(6)
B_0'' / cm^{-1}	0.0490(18)	0.0486(7)	0.0482(32)
R_0'' / Å	2.530(46)	2.529(18)	2.527(84)

All uncertainties are 2σ, based on the statistical errors calculated from the fit of the unweighted rotational lines.

Isotope shifts for the (0 - 0) and (1 - 0) bands of the A ← X system of Ag_2
(in sense of to go from the origin of the lighter isotopomer to that of the heavier one add the following values)

All values are in cm^{-1}

	(0 - 0)	(1 - 0)
$^{107}Ag^{109}Ag$ - $^{107}Ag_2$	0.090(14)	-0.637(25)
$^{109}Ag_2$ - $^{107}Ag_2$	0.163(17)	-1.263(29)

Calculated isotope shifts from the vibrational constants of Kleman and Lindkvist [16]:

$^{107}Ag^{109}Ag$ - $^{107}Ag_2$	0.085	-0.628
$^{109}Ag_2$ - $^{107}Ag_2$	0.171	-1.252

All uncertainties are 2σ.

6.3.1 Simulated Spectra

Simulations of the experimental spectra were carried out using the rotational constants determined in this work (table 6.8). The intensities of the rotational lines were calculated using the Honl - London formulae for a $\Delta\Lambda = 0$ transition [36]. The population distribution over the ground state rotational levels was assumed to follow Boltzman statistics. The rotational temperature was estimated at 5 K, subsequent simulations at different temperatures confirmed this initial estimate as correct. The widths of the rotational lines were determined by convolution of the calculated line position with a Gaussian function describing the finite bandwidth of the laser (0.04 cm^{-1}), the Doppler width of the lines was ignored as it was $\sim$ $1/20^{th}$ of the laser bandwidth. The results of these simulations are shown in figures 6.5(b) - 6.8(b). The line positions obtained agree with the observed spectra, confirming the assignment and calculated constants.

6.4 Lifetime of the A state

During the course of the work on the A $\leftarrow$ X system of Ag_2 an attempt was made to measure the lifetime of the A state. This was carried out by holding the dye laser tuned to the R - branch head of the (0 - 0) transition of the $^{107}Ag_2$ species, and scanning the time delay between the trigger pulses for this laser and the excimer laser used to accomplish ionisation (see section 3.2.4). The integrated intensity of the $^{107}Ag_2$ photoion signal versus the time delay between the laser triggers is shown in figure 6.9.

Figure 6.9
Integrated intensity of the $^{107}Ag_2$ photoion signal vs delay time between excitation and ionisation lasers, for $A \leftarrow X$, (0 - 0) R branch head (time in microseconds)

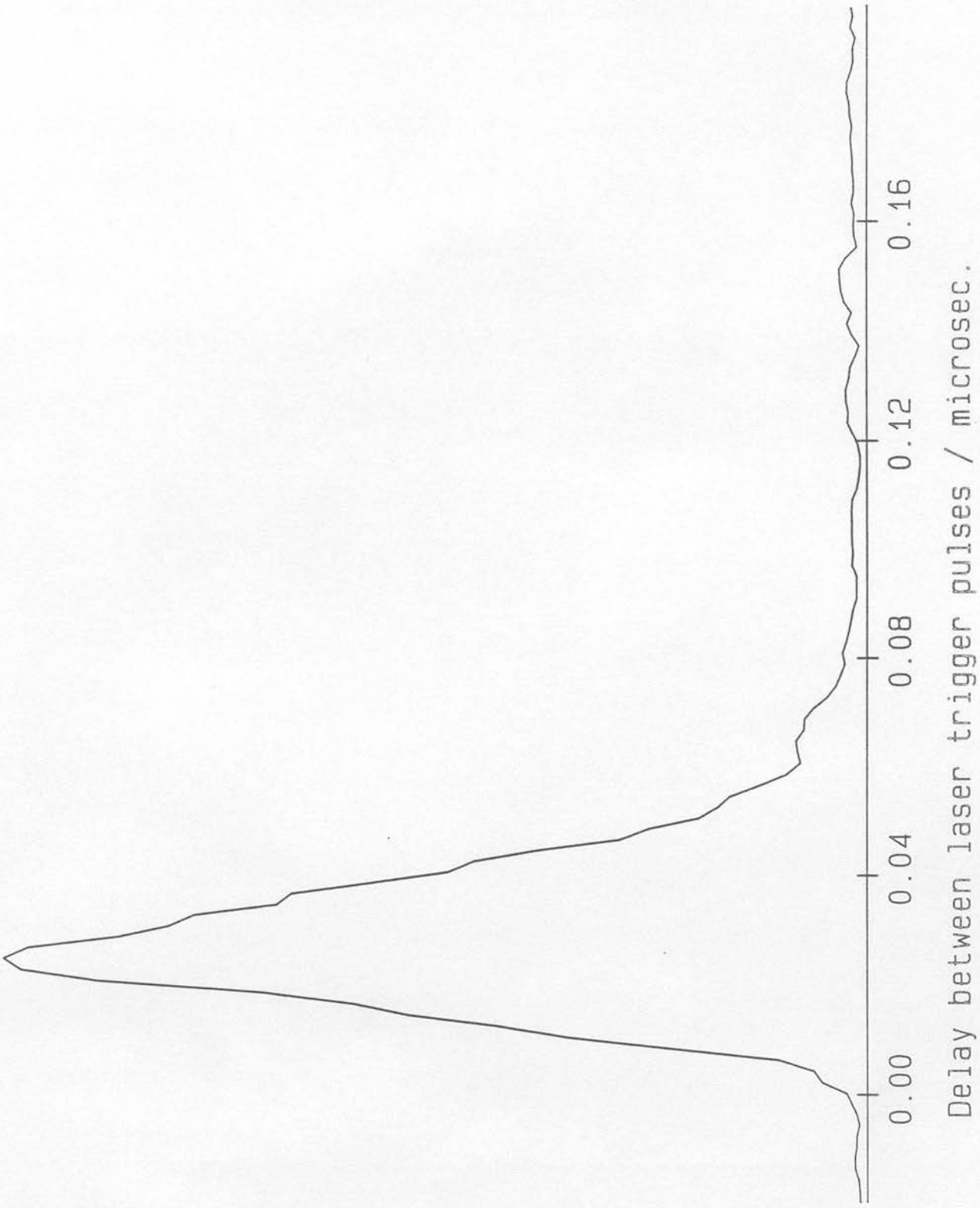

This shows a nearly symmetrical peak which is due to the convolution of the two laser pulses and would require either deconvolution of the laser pulse profiles or shorter pulse durations to accurately determine the lifetime. From figure 6.9 an estimate for the lifetime of $<\simeq$ 40 ns was made. This short lifetime shows the importance of maintaining the temporal overlap of the lasers during a wavelength scan, as even the smallest change in the time between pumping the A state and ionisation will result in a large change in the recorded photoion intensity as either a significant fraction of the available population will have decayed, or the ionisation laser pulse will arrive before that of the excitation laser used to populate the excited state. Excursions of tens of nanoseconds in the delay between the two lasers were not uncommon during the experiments, and were a major source of experimental difficulty.

Such a short lifetime points to either predissociation of the upper state or a very strongly allowed transition which rapidly decays back to the ground state. No direct evidence in the form of an increase in the atomic ion signal was observed to support the theory of rapid predissociation. The implications of this short lifetime with respect to the probable excited state electronic configuration are discussed in section 6.5.

6.5 Assignment of the A state electronic configuration

When attempting to assign the A state to a particular electronic configuration cognisance had to be taken of the experimentally observed facts. These are the term value, the vibrational constants, the rotational constant, the change in bond

length, the symmetry, and the lifetime. Silver is the simplest of the second row transition metals, with the ground atomic state configuration [Kr] $4d^{10}$ $5s^{1}$ it is analogous to copper in the first row. The absence of any spin - orbit components gives rise to only one possible electronic configuration for the ground state of the dimer, namely $^{1}\Sigma_{g}^{+}$:-

$$[Kr][Kr]\ 4d\sigma_g^2\ 4d\pi_u^4\ 4d\delta_g^4\ 4d\delta_u^4\ 4d\pi_g^4\ 4d\sigma_u^2\ 5s\sigma_g^2$$

The above description of the ground state symmetry assumes the coupling of the spin and orbital angular momentum components to the internuclear axis can be adequately described by Hunds' case (a). In such a heavy species as Ag_2 it is more likely that the coupling of the angular momentum follows Hunds' case (c). In this case Λ and Σ are no longer good quantum numbers and it is only their resultant, Ω in the direction of the internuclear axis that is meaningful. In this case the ground state is described as 0_g^+, restricting the upper state to having the symmetry 0_u^+. This is due to the $+ \leftrightarrow +$ and $g \leftrightarrow u$ selection rules for diatomic molecules [36]. The $A \leftarrow X$ transition has been previously assigned by Mitchell et. al. [24] to the $5s\sigma_g \rightarrow 5s\sigma_u$ promotion, and in view of the large calculated separation of the 5s, 5p, and 4d molecular orbitals [23] this would appear to be the least energetic transition. This compares with the situation in copper dimer where the 3d and 4s molecular orbitals lie close in energy with the lowest energy transition being the $3d\pi_g \rightarrow 4s\sigma_u$ promotion.

The $5s\sigma_g \rightarrow 5s\sigma_u$ promotion will formally give rise to an ion pair state in Hunds' case (a) coupling, derived from the ion pair limit at 63883 cm^{-1}. However in case (c) coupling this state will undergo avoided crossings with other

0_u^+ states correlating with the lower lying neutral atom asymptotes. This explains the similarities between this state and the B state of copper dimer which has been assigned to the corresponding $4s\sigma_g \rightarrow 4s\sigma_u$ excitation [14]. Both states have short lifetimes (< 40 ns) and exhibit a small increase (~ 0.1 Å) in bond length over that in the ground state. This is as expected due to the strongly allowed nature of the transition (it breaks no selection rules and does not involve a change in quantum number) and the ion pair character of the upper state respectively. The difference between the two dimers is in the assumed dissociation limits of the states. In copper the B state must dissociate to the $^2D + {}^2S$ limit as the $^2P + {}^2S$ limit is too high in energy. This results in one of the atoms undergoing a formally forbidden $\Delta L = 2$ ($^2D \leftarrow {}^2S$) transition.

The ^2P and ^2D atomic levels in silver, however, lie much closer together (see table 6.9 [37]), with the different spin - orbit components overlapping. This means that the A state of silver dimer may dissociate to $^2P + {}^2S$ atoms, resulting in an allowed transition in one of the atoms. This will make the molecular transition more strongly allowed than the corresponding $B \leftarrow X$ transition in Cu_2. The difference in strength between the Ag_2 $A \leftarrow X$ and Cu_2 $B \leftarrow X$ transitions is not expected to be obvious in the low vibrational levels accessed in the present work and that of Cartwright [38], due to the strong ion pair character exhibited at the bottom of the potentials. As the bond length increases towards dissociation marked differences in the lifetimes should be observed as the transition back to the ground state will become essentially localised on one of the atoms. Thus the B state of Cu_2 should show an increase in the lifetime due to the forbidden nature of the $^2D \rightarrow {}^2S$ transition back to the ground state.

Table 6.9
Lowest ^{2}P and ^{2}D atomic limits for silver

Config.	Term	J	Energy / cm^{-1}
$4d^{10}\ 5s$	^2S	1/2	0.00
$4d^{10}\ 5p$	^2P	1/2	29552.05
		3/2	30472.71
$4d^9\ 5s^2$	^2D	5/2	30242.26
		3/2	34714.16

These values are taken from reference [37].

In contrast the allowed nature of the $^2P \rightarrow {}^2S$ transition in silver dimer should result in little change in the lifetime at higher vibrational levels. If however there is little difference between the excited state lifetimes of the two dimers in higher vibrational levels, and both become much longer lived, then the postulate for the silver dimer A state dissociation limit would have to be changed to one of the $^2D + {}^2S$ limits.

The $^2P + {}^2S$ and $^2D + {}^2S$ atomic limits give rise to a total of 4 0_u^+ states (see table 5.8), any of which may be the A state. However the most likely candidate would appear to be the one derived from the $^2P_{1/2} + {}^2S_{1/2}$ limit at $D_e(X) + 29552\ cm^{-1}$ as correlation with any of the higher limits would lead to an avoided crossing with the 0_u^+ state derived from this atomic asymptote.

6.6 Comparison of the results with theoretical predictions

Theoretical studies of silver dimer have been limited in all but two cases to states correlating with the $^2S + {}^2S$ ground state asymptote. The ground state equilibrium bond lengths derived from these calculations are summarised in table 6.10. The distribution of the results is displaced somewhat to the high side of the experimentally derived value, more so when it is considered that these are predictions of R_e which will be shorter than the experimentally determined value which is for R_0. Those in closest agreement by Ziegler [4] and Martin [10] both take account of relativistic effects indicating their importance in heavy systems such as Ag_2.

Table 6.10
Summary of theoretical predictions for the equilibrium bond length in the ground state of $^{107}Ag_2$

Method	Rel. / Non.-Rel.	R_e / Å	Reference
Hartree - Fock / CI	(NR)	2.75	[5]
Hartree - Fock / CI	(NR)	2.67	[4]
Hartree - Fock / CI	(R)	2.52	[4]
ECP	(R)	2.68	[12]
MCSCF	(NR)	2.56	[7]
extrapolation from Cu_2 and Au_2		2.48	[20], [18]
RECP	(R)	2.52	[10]
ECP	(R)	2.58	[2]
Pseudo Potl. SCF	(NR)	2.55	[8]
ECP	(R)	2.62	[3]
'model potential'	(NR)	2.55	[1]
SCF / MCSCF / CASSCF	(NR)	2.65 - 2.77	[6]
SCF-Xα-SW	(NR)	2.84	[23]

There appear to have been only two attempts to perform calculations on excited states of silver dimer. Ozin et. al. [23] used the SCF-Xα-SW method to calculate a transition energy of 25700 cm^{-1} for the $5s\sigma_g \rightarrow 5s\sigma_u$ excitation, at a fixed bond length of 2.47 Å. Basch [12] has used an effective core potential (ECP) method, where the 4d electrons were not included in the core potential, to calculate the transition energy and the equilibrium bond length of the $^1\Sigma_u^+$ state derived from the $^2S + {}^2P$ limit. This gave R_e = 2.997 Å, ω_e = 165 cm^{-1}, and T_e = 20888 cm^{-1}. Both of these calculations show significant deviations from experiment and further *ab initio* calculations are awaited.

6.7 Conclusion

The A ← X system of silver dimer has been rotationally analysed and shown to be a $\Delta\Omega = 0$ type transition. It is proposed that the A - state is the 0_u^+ state correlating with the $^2S + {}^2P$ atomic asymptote at $D_e(X)$ + 29552 cm^{-1}.

Subsequent to the completion of the work described here one of my co - workers, Mr. Andrew M. James has carried out further work on the A ← X system of silver dimer at the National Research Council of Canada in Ottawa [39]. In this work a ring dye laser of substantially higher resolution than the dye laser used in the current work was employed to probe silver dimer contained in a free jet similar to the one described here. Fluorescence excitation spectra for the dimer were recorded, and the following rotational constants were obtained for the $^{107}Ag^{109}Ag$ isotopomer; B_0'' = 0.048682(19) cm^{-1} and B_0' = 0.044224(18) cm^{-1}, in good agreement with those presented in table 6.8. The analysis of the fluorescence spectra to obtain these results used the constants derived from the

rotational analysis presented in this chapter, to assign the lines to the correct isotopomer. A total of 154 lines from the P and R branches of the (0 - 0) band were included in the least mean squares fit.

References

[1] Andzelm J., Radzio E., Salahub D.R., J. Chem. Phys., **83**, p 4573, (1985)
[2] Walch S.P., Bauschlicher C.W., Langhoff S.R., J. Chem. Phys., **85**, p 5900, (1986)
[3] Hay P.J., Martin R.L., J. Chem. Phys., **83**, p 5174, (1985)
[4] Ziegler T., Snijders J.G., Barends E.J., J. Chem. Phys., **74**, p 1271, (1981)
[5] Shim I., Gingerich K.A., J. Chem. Phys., **79**, p 2903, (1983)
[6] Ermler W.C., Ross R.B., Pitzer R,B,, *unpublished results*, (1989),
[7] McLean A.D., J. Chem. Phys., **79**, p 3392, (1983)
[8] Stoll H., Fuentealba P., Schwendtfeger P., Flad J., Szentpoly L.V., Preuss H., J. Chem. Phys., **81**, p 2732, (1984)
[9] Stoll H., Fuentealba P., Schwendtfeger P., Flad J., Szentpoly L.V., Preuss H., J. Chem. Phys., **79**, p 5532, (1983)
[10] Martin R.L., J. Chem. Phys., **86**, p 5027, (1987)
[11] Walch S.P., Bauschlicher C.W., *Theoretical Studies of Transition Metal Dimers*, Comparison of *ab initio* Quantum Chemistry with Experiment for Small Molecules; Ed R.J. Bartlett, D. Reidel Publ. Co., Holland (Dordrecht), 1985.
[12] Basch H., J. Am. Chem. Soc., **103**, p 4657, (1981)
[13] Baetzold R.C., J. Chem. Phys., **55**, p 4355, (1975)
[14] Morse M.D., Chem. Rev., **86**, (1986)
[15] Ruamps J., Comptes Rendus, **238**, p 1489, (1954)
[16] Kleman B., Lindkvist S., Arkiv fur Fysik, **9**, p 385, (1955)
[17] Gingerich K.A., Faraday Symp., **14**, p 109, (1980)
[18] Brown C.M., Ginter M.L., J.Mol. Spec., **69**, p 25, (1978)
[19] Maheshwari R.C., Ind. J. Phys., **27**, p 368, (1962)
[20] Sradnov V.I., Pesic D.S., J. Mol. Spec., **90**, p 27, (1981)
[21] Shin-Piaw C., Loong-Seng W., Yoke-Seng L., Nature, **209**, p 1300, (1966)
[22] Mitchell S.A., Ozin G.A., J. Phys. Chem., **88**, p 1425, (1984)
[23] Ozin G.A., Huber H., McIntosh D., Mitchell S.A., Norman J.G., Noodlemann L., J. Am. Chem. Soc., **101**, p 3504, (1979)
[24] Mitchell S.A., Kenny-Wallace G.A., Ozin G.A., J. Am. Chem. Soc., **103**, p 6030, (1981)
[25] Desclaux J.P., Atomic Data and Nuclear Data Tables, **12**, p 311, (1973)
[26] Hopkins J.B., Langridge-Smith P.R.R., Morse M.D., Smalley R.E., *unpublished results*,
[27] Bevington P.R., *Data Reduction and Error Analysis for the Physical Sciences*, McGraw - Hill, New York, 1969.
[28] Ames L.L., Barrow R.F., Trans. Faraday Society, **63**, p 39, (1967)
[29] Basch H., Faraday Symp., **14**, p 149, (1980)
[30] Baetzold R.C., Mack R.E., J. Chem. Phys., **62**, p 1513, (1975)
[31] Hamilton J.F., J. Vac. Sci. Technol., **13**, p 319, (1976)
[32] Hollas J.M., *High Resolution Spectroscopy*, Butterworth, London, 1982.
[33] Anderson J.F., *Structure of Metallic Catalysts*, Academic Press, London, 1975.
[34] Gole J.L., *Metal Clusters, ed. Moskovits M.*, Wiley Interscience, Toronto, 1985.
[35] Savitzky A., Golay M.J.E., Anal. Chem., **36**, p 1627, (1964)

[36] Herzberg G., *Spectra of Diatomic Molecules*, Van Nostrand Reinhold, New York, 1950.
[37] Moore C.E., *Atomic Energy Levels, Vol. III*, U.S. Department of Commerce, National Bureau of Standards, Washington, 1952.
[38] Cartwright P.C., *PhD Thesis*, Edinburgh University, 1989.
[39] Simard B., James A.M., *unpublished results*,

Appendix A
Program Archive and How to Restore it

The entire code for the THOR program is archived on the EMAS-A mainframe at Edinburgh University. The archived code is stored in a partitioned file called THOR89 on process EDCG01. The file is permitted for reading from any EMAS process. The file THOR contains further partitioned files with the assembler and 'C' code along with a catalogue (produced by the Microsoft LIB utility) and the header files.

The filenames are relatively self explanatory, e.g. TCAMAC and TPLOT contain the CAMAC and plotting functions respectively. The 'C' files all have a 'T' at the beginning of the filename.

The THOR89 file should be accessed with the VIEW command on EMAS, it may need to be RESTOREd from the archive first. The first *view* menu will display the main divisions; C, ASM, BAT, H, CAT, and README. Select the C, ASM, or H section to see the 'C' code, assembler code, or the 'C' header files.

The TMAIN file contains the *main* function. To find a particular function first go to the *selector* or *keyhandler* function. These contain the calls to all the functions available from the menus. The location of a function (or global variable) can then be looked up in the CAT file. This will give the name of the file in which the function can be found. All the function declarations are at the bottom of the header file called THOR. These declarations show the types of the variables passed to and returned by all the functions.

To create an executable file from the archived code it needs to be

downloaded to a PC with a hard disk. All the C files need the extension '.C' appended, e.g. TCAMAC becomes TCAMAC.C. The assembler files need '.ASM' appended, e.g. MTTIOC becomes MTTIOC.ASM. The header files need '.H' appended, e.g. THOR becomes THOR.H. The two files in the BAT section, THOR and MAKE need to be renamed THOR.LNK and THOR (no extension). The files should all be placed in a directory called ABZ.

Ensure that the PC has a C compiler, assembler, LIB utility, LINK utility, and MAKE utility installed. The linker should be renamed 'C5L'. The versions of the above used currently are:

Microsoft C compiler V 5.0

IBM MACRO assembler V 2.0

Microsoft LIB V 3.08

Microsoft Overlay Linker V 3.61

Microsoft MAKE V 4.06

To create the .EXE file type 'MAKE THOR' at the DOS prompt. This will create a library of the compiled assembler functions and an executable version of the code called THOR.EXE.

The program requires at least an 80286 processor and coprocessor to run. The display must be an EGA screen with 256 Kb RAM, and at least 640 Kb of RAM on the system board.

To run the program type THOR at the DOS prompt. Ignore the message about THOR.CON not being found and hit any key to start the program. Once a configuration has been set up it can be saved as THOR.CON by the program.

This configuration will be automatically reset each time the program is run.

The archived version is set to operate with the PC004 interface card / 6002 crate controller from DSP. The header file TCAMAC contains 3 defines at the top. Either TRANSIAC or HYTEC should be set to 1. TRANSIAC refers to the DSP crate controller, HYTEC refers to the 1304 crate controller and interface card from Hytec. Only one of these should be set to 1 at a time, the other should be set to 0. The TIMING flag can be set to 1 if the timing functions are to be implemented. The timing functions are not required in normal use. They are accessed from the *<t>* option in the main menu. The program requires all the CAMAC units described in chapter 3 to be in place in the crate. The slots the program expects them in are shown in *DEFINE* statements in the header file THOR. After any changes are made to any of the source or header files the program must be recompiled by typing 'MAKE THOR', at the DOS prompt before it is used again. Failure to do this will result in none of the changes being incorporated in the executable code.

The source code for the ODIN program is stored in an identical manner in the file ODIN89. The files should be placed in a directory called *ODIN* on the PC. The *help* files included in the EMAS partitioned file must be put in a directory called *HELP* on the PC with the file extension *.hlp* added to them. The files *odinplin* and *odinppc* should be renamed *odinp_.hlp* and *odinp%.hlp* respectively after transfer to the PC.

Appendix B
Data Storage Format

THOR used two different formats for storing the data for the time and frequency scan modes. This was done to maximise speed in the case of the time scans and storage capacity in the case of the frequency scans. Both modes stored the data for the selected ion signals separately in blocks of 256 points. A 40 Kb buffer was set aside in the RAM of the PC - AT for storing this data prior to transfer to disk.

B.1 Time scans

The data stored for each ion signal during time scans consisted of the sum of the integrated ion intensity, the sum of the square of the integrated intensity and the number of shots acquired at each delay time (i.e. the number of scans). These values were stored in a structure data type with the following form:

```
struct parmscan
{
float sum;
float sumsqr;
unsigned count;
};
```

This structure occupied 10 bytes of memory per ion signal for each delay time. The maximum number of steps in a time delay scan was set at 256, requiring 2560 bytes per channel. The data structures were stored consecutively

for each ion signal as follows:

Sig.1 (P_T 0 → P_T 255)

Sig.2 (P_T 0 → P_T 255)

.

.

.

.

Sig.n (P_T 0 → P_T 255)

A maximum of 10 signals were allowed for any one scan, all of which had to be ion signals. The input recorded with the ADC module could not be monitored during a time scan.

B.2 Frequency Scans

For frequency scans the same area of memory as for time scans was used but the storage method was altered so that maximum usage was made of the available memory . Only the average signal was stored, as a four byte floating point number. The signals were stored in blocks of 256 points. This meant that each block of 256 points required 1 Kb of RAM for every signal that was defined and in use. The arrangement of these 256 point blocks was as follows:

Sig.1 (P_f 0 → P_f 255), Sig.2 (P_f 0 → P_f 255)....Sig.n (P_f 0 → P_f 255)

Sig.1 (P_f 256 → P_f 511), Sig.2 (P_f 256 → P_f 511)...Sig.n(P_f 256 → P_f 511)

.

.

.

.

The maximum number of signals allowed was 10, in which case only 1024 points were able to be collected and stored. If there were fewer signals defined then more data points could be collected (i.e. a longer frequency range was covered) in blocks of 256, up to a limit of 2560 points per signal.

Appendix C
Rotational Line Fitting Program

```
C The following program accepts measured rotational line positions
C either in the form of bin numbers or wavenumbers. If the line
C positions are given in bin numbers then the constants obtained
C from a polynomial fit of concurrently recorded etalon fringes
C must be supplied. The program then uses this information to
C convert the line positions in bin numbers to offsets in
C wavenumbers from an arbritary zero which must be supplied as a
C bin number (it need not be an integer value).
C  Once converted to wavenumbers the line positions are fitted by
C a least mean squares method in subroutine REGRES to the functions:
C
C   E(P) = [B'(J"-1)J"+D'(J"-1)**2*J"**2...] -
C          [B"J"(J"+1)+D"J"**2(J"+1)**2...]
C   E(R) = [B'(J"+1)(J"+2)+D'(J"+1)**2(J"+2)**2...] -
C          [B"J"(J"+1)+D"(J"+1)**2(J"+2)**2...]
C
C where E(P/R) refers to the line position in wavenumbers & J"
C refers to the lower state rotational level. NOTE that the D" &
C D' values will be calculated with the opposite sign to that
C normally used, & similarly when inputting D values the sign
C must be reversed.

C  The program can cope with lines of unequal weighting, the type
C of weighting is selected by the third variable (IW) read in
C from the file containing the rotational line data. Three types
C of weighting are possible signified by 0 (no weighting), 1
C (instrumental weighting, 1/[sigma**2]), & -1 (statistical
C weighting, 1/Y[i]). For instrumental weighting the value of
C sigma must follow each data point. The first two values in the
C data file must be the masses of the two atoms in a.m.u.

C The format of the data file is as follows:
C
C       mass1
C       mass2
C       type_of_weighting
C       'x' J" data [sigma]
C        .
C        .
C        .
C
C  The x must be replaced by the branch to which the line
C belongs, if it is left as x then the program ignores that data
C point in the fitting of the data. Combination differences
C between the P, Q, & R branches can be calculated as well.

      PROGRAM fit
C>>>>> NR is max number of records that can be processed
```

```
C>>>>> NC is max number of constants that can be calculated
C>>>>> ACC is the precision which is used when truncating the
C>>>>> line position in bin numbers, number = 1/(power of ten)
C>>>>> used in rounding
      PARAMETER(NR=300, NC=20, ACC=1000)
      IMPLICIT DOUBLE PRECISION (A-H,O-Z)
      DOUBLE PRECISION SPCT(NR,3),J(NR,NC),C(NC),SIGMAE(NR),R(NC),
     *SIGMAC(NC),EFIT(NR),E(NR),ETCON(NC),KUSC(NC),KLSC(NC)
      DIMENSION M(NR)
      CHARACTER*31 FILNAM1,FILNAM2
      CHARACTER*1 PQR(NR)
      DATA M,SIGMAE/NR*1,NR*1.0/
      CALL EMAS3PROMPT('Name of file containing rotational line
     *data: ')
      READ(*,'(A31)')FILNAM1
      CALL EMAS3('COPY',FILNAM1//',T£PBRA',IFLAG)
      OPEN(UNIT=23,FILE='T£PBRA')
      READ(23,*)ZMASS1
      READ(23,*)ZMASS2
C>>>>> IW needs to be 1 for 1/Y(i), 0 for 1, & -1 for
C>>>>> SIGMAE(i) weighting
      READ(23,*)IW
      U=ZMASS1*ZMASS2/(ZMASS1+ZMASS2)
      CON=1.676E-19/U
C>>>>> Get data format & read etalon constants if necessary.
C>>>>> Etalon file format if the same as the order used to read
C>>>>> from the terminal.
      CALL EMAS3PROMPT('Data format (1=energy, 0=rec.£):')
        READ*,IFORM
        IF(IFORM.EQ.0)THEN
        CALL EMAS3PROMPT('Is etalon data in a file(0), or not(1):')
          READ*,IWE
          IF(IWE.EQ.1)THEN
          CALL EMAS3PROMPT('Input £ of etalon constants:')
          READ*,NETCONS
        CALL EMAS3PROMPT('Input etalon constant:')
          DO 7 NET=1,NETCONS
    7   READ*,ETCON(NET)
          CALL EMAS3PROMPT('Input reference rec.£:')
          READ*,REFCHAN
          CALL EMAS3PROMPT('Input energy ref. (Cm-1):')
          READ*,REFENERGY
          CALL EMAS3PROMPT('Scan dirn.(1=blue, 0=red):')
          READ*,ISCAN
        CALL EMAS3PROMPT('Save this in a file(0=NO, 1=YES)')
          READ*,ISV
          IF(ISV.EQ.1)THEN
          CALL EMAS3PROMPT('What do you want to call the file:')
          READ(*,'(A31)')FILNAM2
          OPEN(UNIT=25,FILE=FILNAM2,FILETYPE='CHARACTER')
          WRITE(25,*)NETCONS
          DO 11 NET=1,NETCONS
   11   WRITE(25,*)ETCON(NET)
```

```
          WRITE(25,*)REFCHAN
          WRITE(25,*)REFENERGY
          WRITE(25,*)ISCAN
          CLOSE(25)
          ENDIF
        ELSE
C>>>>>> Save etalon constants for reloading in future.
          CALL EMAS3PROMPT('What is the file called:')
         READ(*,'(A31)')FILNAM2
        CALL EMAS3('COPY',FILNAM2//',T£PBRACON',IFLAG)
          OPEN(UNIT=25,FILE='T£PBRACON')
          READ(25,*)NETCONS
          DO 10 NET=1,NETCONS
   10   READ(25,*)ETCON(NET)
          READ(25,*)REFCHAN
          READ(25,*)REFENERGY
          READ(25,*)ISCAN
          ENDIF
          IF(ISCAN.EQ.0)ISCAN=-1
        ENDIF
C>>>>> Read in data depending whether sigma is included or not.
      IF(IW.GT.0)THEN
      READ(23,*,END=3)(PQR(I),(SPCT(I,K),K=1,2),SIGMAE(I),I=1,NR)
      ELSE
      READ(23,*,END=3)(PQR(I),(SPCT(I,K),K=1,2),I=1,NR)
      ENDIF
    3 CONTINUE
      I=I-1
      IT=I
C>>>>> If data is bin numbers the round to required No.
C>>>>> decimal places.
      IF(IFORM.EQ.0)THEN
      DO 1234 IJKL=1,I
      SPCT(IJKL,2)=FLOAT(INT((SPCT(IJKL,2)*ACC)+0.5))/ACC
 1234 SPCT(IJKL,3)=SPCT(IJKL,2)
      ENDIF
C>>>>> Get any known constants & number to be calculated
      CALL EMAS3PROMPT('How many upper state constants are known? ')
      READ*,KNUSC
      IF(KNUSC.NE.0)THEN
      CALL EMAS3PROMPT('Enter constant: ')
      DO 12 IJKL=1,KNUSC
  12  READ *,KUSC(IJKL)
      ENDIF
      CALL EMAS3PROMPT( '& how many to be calculated? ')
      READ *,NUSC
      CALL EMAS3PROMPT('How many lower state constants are known? ')
      READ *,KNLSC
      IF(KNLSC.NE.0)THEN
        CALL EMAS3PROMPT('Enter constant: ')
      DO 13 IJKL=1,KNLSC
   13 READ*,KLSC(IJKL)
      ENDIF
```

```
      CALL EMAS3PROMPT('& how many to be calculated? ')
      READ*,NLSC
       N=NUSC+NLSC
      CALL EMAS3PROMPT('Calculate combination differences?
     *(0=NO, 1=YES)')
      READ*,ICOM
C>>>>> convert bin numbers to offset in wavenumbers
       IF(IFORM.EQ.0)THEN
          DO 8 NPK=1,I
         OFST=0.
          DIF=FLOAT(INT(((SPCT(NPK,2)-REFCHAN)*ACC)+0.5))/ACC
      IF(DIF.NE.0)THEN
          DO 9 NAPY=1,NETCONS
    9 OFST=OFST+ETCON(NAPY)*DIF**(NAPY-1)
      SPCT(NPK,2)=REFENERGY+FLOAT(ISCAN)*OFST
      ELSE
      SPCT(NPK,2)=0.0D0
      ENDIF
    8 CONTINUE
       ENDIF
C>>>>> remove known constants from data
      KJ=0
      DO 6 KL=1,I
      IF(PQR(KL).NE.'X'.AND.PQR(KL).NE.'x')THEN
      KJ=KJ+1
      E(KJ)=SPCT(KL,2)
      IF(KNUSC.NE.0)THEN
      DO 14 IJKL=1,KNUSC
      IF(PQR(KL).EQ.'P'.OR.PQR(KL).EQ.'p')E(KJ)=E(KJ)-KUSC(IJKL)
     £*SPCT(KL,1)**IJKL*(SPCT(KL,1)-1)**IJKL
      IF(PQR(KL).EQ.'Q'.OR.PQR(KL).EQ.'q')E(KJ)=E(KJ)-KUSC(IJKL)
     £*SPCT(KL,1)**IJKL*(SPCT(KL,1)+1)**IJKL
      IF(PQR(KL).EQ.'R'.OR.PQR(KL).EQ.'r')E(KJ)=E(KJ)-KUSC(IJKL)
     £*(SPCT(KL,1)+1)**IJKL*(SPCT(KL,1)+2)**IJKL
   14 CONTINUE
      ENDIF
      IF(KNLSC.NE.0)THEN
      DO 15 IJKL=1,KNLSC
   15 E(KJ)=E(KJ)+KLSC(IJKL)*SPCT(KL,1)**IJKL*(SPCT(KL,1)+1)**IJKL
      ENDIF
      ENDIF
    6 CONTINUE
C>>>>> setup the array in J" as a substitute for the FCTN in REGRES
      CALL SETUP(PQR,SPCT,J,I,NR,NC,NUSC,NLSC,KNUSC,KNLSC)
C>>>>> Do least squares fit, note total size of arrays must be
C>>>>> passed as well (NR & NC)
      CALL REGRES(J,E,NC,NR,SIGMAE,I,N,M,IW,EFIT,C0,C,SIGMA0,
     !SIGMAC,R,RMUL,CHISQR,FTEST)
C>>>>> Adjust calculated (EFIT) & measured (E) line positions
C>>>>> with known constants.
      IF(KNUSC.NE.0.OR.KNLSC.NE.0)THEN
      KJ=0
      DO 16 KL=1,IT
```

```
      IF(PQR(KL).NE.'X'.AND.PQR(KL).NE.'x')THEN
      KJ=KJ+1
      IF(KNUSC.NE.0)THEN
      DO 17 IJKL=1,KNUSC
      IF(PQR(KL).EQ.'P'.OR.PQR(KL).EQ.'p')EFIT(KJ)=EFIT(KJ)+
     £KUSC(IJKL)*SPCT(KL,1)**IJKL*(SPCT(KL,1)-1)**IJKL
      IF(PQR(KL).EQ.'Q'.OR.PQR(KL).EQ.'q')EFIT(KJ)=EFIT(KJ)+
     £KUSC(IJKL)*SPCT(KL,1)**IJKL*(SPCT(KL,1)+1)**IJKL
      IF(PQR(KL).EQ.'R'.OR.PQR(KL).EQ.'r')EFIT(KJ)=EFIT(KJ)+
     £KUSC(IJKL)*(SPCT(KL,1)+1)**IJKL*(SPCT(KL,1)+2)**IJKL
      IF(PQR(KL).EQ.'P'.OR.PQR(KL).EQ.'p')E(KJ)=E(KJ)+KUSC(IJKL)
     £*SPCT(KL,1)**IJKL*(SPCT(KL,1)-1)**IJKL
      IF(PQR(KL).EQ.'Q'.OR.PQR(KL).EQ.'q')E(KJ)=E(KJ)+KUSC(IJKL)
     £*SPCT(KL,1)**IJKL*(SPCT(KL,1)+1)**IJKL
      IF(PQR(KL).EQ.'R'.OR.PQR(KL).EQ.'r')E(KJ)=E(KJ)+KUSC(IJKL)
     £*(SPCT(KL,1)+1)**IJKL*(SPCT(KL,1)+2)**IJKL
   17 CONTINUE
      ENDIF
      IF(KNLSC.NE.0)THEN
      DO 18 IJKL=1,KNLSC
      E(KJ)=E(KJ)-KLSC(IJKL)*SPCT(KL,1)**IJKL*(SPCT(KL,1)+1)**IJKL
   18 EFIT(KJ)=EFIT(KJ)-KLSC(IJKL)*SPCT(KL,1)**IJKL*(SPCT(KL,1)
     £+1)**IJKL
      ENDIF
      ENDIF
   16 CONTINUE
      ENDIF
C>>>>> Calcualte bond lengths from B values & masses from data file
      IF(KNUSC.NE.0)THEN
      REU=SQRT(CON/ABS(KUSC(1)))*1.0D10
      ELSE
      REU=SQRT(CON/ABS(C(1)))*1e10
      ENDIF
      IF(KNLSC.NE.0)THEN
      REL=SQRT(CON/ABS(KLSC(1)))*1.0D10
      ELSE
      REL=SQRT(CON/ABS(C(NUSC+1)))*1e10
      ENDIF
C>>>>> Write everything to a file (T£) files are temporary on EMAS
      OPEN(UNIT=24,FILE='t£cal',filetype='character')
      PRINT*,'Data in file T£CAL (will be lost at logoff)'
      WRITE(24,99)FILNAM1
      IF(IFORM.EQ.0)WRITE(24,199)FILNAM2
      WRITE(24,100)C0,SIGMA0
      WRITE(24,101)
      IF(KNUSC.NE.0)THEN
      WRITE(24,108)
      WRITE(24,110)(KUSC(K),K=1,KNUSC)
      ENDIF
      IF(NUSC.NE.0)THEN
      WRITE(24,109)
      WRITE(24,102)(C(K),SIGMAC(K),K=1,NUSC)
      ENDIF
```

```
      WRITE(24,107)REU
      WRITE(24,103)
      IF(KNLSC.NE.0)THEN
      WRITE(24,108)
      WRITE(24,110)(KLSC(K),K=1,KNLSC)
      ENDIF
      IF(NLSC.NE.0)THEN
      WRITE(24,109)
      WRITE(24,102)(C(K+NUSC),SIGMAC(K+NUSC),K=1,NLSC)
      ENDIF
      WRITE(24,107)REL
      IF(IFORM.EQ.0)THEN
      WRITE(24,114)
      ELSE
      WRITE(24,104)
      ENDIF
      KJ=0
      SD=0
      DO 98 K=1,IT
      IF(IFORM.EQ.1)THEN
      IF(PQR(K).NE.'X'.AND.PQR(K).NE.'x')THEN
      KJ=KJ+1
      WRITE(24,125)PQR(K),INT(SPCT(K,1)),SPCT(K,2),SIGMAE(K),
     £EFIT(KJ),SPCT(K,2)-EFIT(KJ)
      ELSE
      WRITE(24,135)PQR(K),INT(SPCT(K,1)),SPCT(K,2),SIGMAE(K)
      ENDIF
      ELSE
      IF(K.NE.1)SD=SPCT(K,3)-SPCT(K-1,3)
      IF(PQR(K).NE.'X'.AND.PQR(K).NE.'x')THEN
      KJ=KJ+1
      WRITE(24,105)PQR(K),INT(SPCT(K,1)),SPCT(K,3),SD,SPCT(K,2),
     !SIGMAE(K),EFIT(KJ),SPCT(K,2)-EFIT(KJ)
      ELSE
      WRITE(24,115)PQR(K),INT(SPCT(K,1)),SPCT(K,3),SD,SPCT(K,2),
     !SIGMAE(K)
      ENDIF
      ENDIF
   98 CONTINUE
      WRITE(24,106)CHISQR,I-NUSC-NLSC-1,FTEST
C>>>>> Calculate combination differences & write to file as well
      IF(ICOM.EQ.0)STOP
      WRITE(24,'(1X,''Combination difference values:-'')')
      KL=0
      DO 80 K=1,IT-1
      IF(PQR(K).NE.'X'.AND.PQR(K).NE.'x')THEN
      KL=KL+1
      IF(PQR(K).EQ.'P'.OR.PQR(K).EQ.'p')THEN
      KM=KL
      DO 81 KJ=K+1,IT
      IF(PQR(KJ).NE.'X'.AND.PQR(KJ).NE.'x')KM=KM+1
      IF((PQR(KJ).EQ.'R'.OR.PQR(KJ).EQ.'r').AND.SPCT(K,1).EQ.
     £SPCT(KJ,1))THEN
```

```
      JL=SPCT(K,1)-1
      BUF=(EFIT(KM)-EFIT(KL))/((JL+2)*(JL+3)-JL*(JL+1))
      BUR=(E(KM)-E(KL))/((JL+2)*(JL+3)-JL*(JL+1))
      WRITE(24,121)JL+1,JL+1,BUR,BUF
      ELSEIF((PQR(KJ).EQ.'R'.OR.PQR(KJ).EQ.'r').AND.SPCT(K,1).EQ.
     !SPCT(KJ,1)+2)THEN
      JL=SPCT(K,1)
      BLF=(EFIT(KM)-EFIT(KL))/(JL*(JL+1)-(JL-2)*(JL-1))
      BLR=(E(KM)-E(KL))/(JL*(JL+1)-(JL-2)*(JL-1))
      WRITE(24,120)JL,JL-2,BLR,BLF
      ENDIF
   81 CONTINUE
      ELSEIF(PQR(K).EQ.'R'.OR.PQR(K).EQ.'r')THEN
      KM=KL
      DO 82 KJ=K+1,IT
      IF(PQR(KJ).NE.'X'.AND.PQR(KJ).NE.'x')KM=KM+1
      IF((PQR(KJ).EQ.'P'.OR.PQR(KJ).EQ.'p').AND.SPCT(K,1).EQ.
     £SPCT(KJ,1))THEN
      JL=SPCT(K,1)+1
      BUF=(EFIT(KL)-EFIT(KM))/(JL*(JL+1)-(JL-2)*(JL-1))
      BUR=(E(KL)-E(KM))/(JL*(JL+1)-(JL-2)*(JL-1))
      WRITE(24,121)JL-1,JL-1,BUR,BUF
      ELSEIF((PQR(KJ).EQ.'P'.OR.PQR(KJ).EQ.'p').AND.SPCT(K,1)
     £.EQ.SPCT(KJ,1)-2)THEN
      JL=SPCT(K,1)+1
      BLF=(EFIT(KL)-EFIT(KM))/((JL+1)*(JL+2)-JL*(JL-1))
      BLR=(E(KL)-E(KM))/((JL+1)*(JL+2)-JL*(JL-1))
      WRITE(24,120)JL+1,JL-1,BLR,BLF
      ENDIF
   82 CONTINUE
      ENDIF
      ENDIF
   80 CONTINUE
   99 FORMAT(1X,'Data for file 'A31)
  199 FORMAT(1X,'Etalon Constants from ',A31)
  100 FORMAT(1X,'Constant= ',F12.5,',  Sigma= ',E20.15)
  101 FORMAT(1X,'Upper State Constants')
  107 FORMAT(1X,'re= ',F5.3,'A')
  102 FORMAT(1X,2(2X,E18.11))
  103 FORMAT(1X,'Lower State contsants')
  104 FORMAT(1X,'PQR J        E(J)    Sigma',TR7,'Efit(J)',TR2,
     £'E(J)-Efit(J)')
  114 FORMAT(1X,'PQR J   Rec.£      N-(N-1)         E(J)    Sigma'
     £,TR7,'Efit(J)',TR2,'E(J)-Efit(J)')
  105 FORMAT(1X,A1,TR2,I2,TR2,F9.3,TR2,F9.3,TR2,F12.5,TR2,F5.3,TR2,
     !F12.5,TR2,E12.5)
  115 FORMAT(1X,A1,TR2,I2,TR2,F9.3,TR2,F9.3,TR2,F12.5,TR2,F5.3)
  125 FORMAT(1X,A1,TR2,I2,TR2,F12.5,TR2,F5.3,TR2,F12.5,TR2,E12.5)
  135 FORMAT(1X,A1,TR2,I2,TR2,F12.5,TR2,F5.3)
  111 FORMAT(1X,'delta=  ',F9.3)
  106 FORMAT(1X,'Reduced Chisq= ',E20.5,', £ DoF= ',I3,', Ftest= '
     £,E20.5)
  108 FORMAT(1X,'Known constants')
```

```
  109 FORMAT(1X,'Calculated constants',TR5,'Error')
  110 FORMAT(1X,'Constant= ',E18.11)
  120 FORMAT(1X,'P=',I2,', R=',I2,', B"=',F12.8,' (raw),  ',
     £F12.8,' (fitted)')
  121 FORMAT(1X,'P=',I2,', R=',I2,', B''=',F12.8,' (raw),  ',
     £F12.8,' (fitted)')
      STOP
      END



      SUBROUTINE SETUP(PQR,SPCT,J,N,NR,NC,NUSC,NLSC,KNUSC,KNLSC)
C>>>>> This sets up array in J" for least mean squares fitting
      IMPLICIT DOUBLE PRECISION (A-H,O-Z)
      DOUBLE PRECISION SPCT(NR,3),J(NR,NC)
      CHARACTER*1 PQR(NR)
      NT=0
      DO 1 K=1,N
      IF(PQR(K).NE.'X'.AND.PQR(K).NE.'x')THEN
      NT=NT+1
      IF(NUSC.EQ.0)GOTO 3
      DO 2 L=KNUSC+1,NUSC+KNUSC
      IF(PQR(K).EQ.'P'.OR.PQR(K).EQ.'p')THEN
      J(NT,L-KNUSC)=SPCT(K,1)**L*(SPCT(K,1)-1)**L
      ELSEIF(PQR(K).EQ.'Q'.OR.PQR(K).EQ.'q')THEN
      J(NT,L-KNUSC)=SPCT(K,1)**L*(SPCT(K,1)+1)**L
      ELSE
      J(NT,L-KNUSC)=(SPCT(K,1)+1)**L*(SPCT(K,1)+2)**L
      ENDIF
    2 CONTINUE
    3 IF(NLSC.EQ.0)GOTO 1
      DO 4 L=KNLSC+1,NLSC+KNLSC
    4 J(NT,L+NUSC-KNLSC)=(SPCT(K,1)**L*(SPCT(K,1)+1)**L)*(-1)
      ENDIF
    1 CONTINUE
      N=NT
      RETURN
      END


      SUBROUTINE REGRES(ARJ,Y,NC,NR,SIGMAY,NPTS,NTERMS,M,MODE,
     £YFIT,A0,A,SIGMA0,SIGMAA,R,RMUL,CHISQR,FTEST)
C>>>>> This is the REGRES routine from :
C>>>>> 'Data Reduction & Error Analysis for the Physical Sciences
C>>>>> P.R Bevington, McGraw-Hill, New York (1969)'
      IMPLICIT DOUBLE PRECISION(A-H,O-Z)
      DOUBLE PRECISION Y(NR),SIGMAY(NR),YFIT(NR),A(NC),
     *SIGMAA(NC),WEIGHT(1000),XMEAN(1000),SIGMAX(1000),
     *ARRAY(100,100),R(NC),ARJ(NR,NC)
      DIMENSION M(NR)
   11 SUM=0.
      YMEAN=0.
```

```
      CHISQ=0.
      SIGMA=0.
      RMUL=0.
      DO 17 I=1,NPTS
   17 YFIT(I)=0.
   21 DO 28 I=1,NTERMS
      XMEAN(I)=0.
      SIGMAX(I)=0.
      R(I)=0.
      A(I)=0.
      SIGMAA(I)=0.
      DO 28 K=1,NTERMS
   28 ARRAY(I,K)=0.
   30 DO 50 I=1,NPTS
   31 IF(MODE)32,37,39
   32 IF(Y(I))35,37,33
   33 WEIGHT(I)=1./Y(I)
      GOTO 41
   35 WEIGHT(I)=1./(-Y(I))
      GOTO 41
   37 WEIGHT(I)=1.
      GOTO 41
   39 WEIGHT(I)=1./SIGMAY(I)**2
   41 SUM=SUM+WEIGHT(I)
      YMEAN=YMEAN+WEIGHT(I)*Y(I)
      DO 44 J=1,NTERMS
   44 XMEAN(J)=XMEAN(J)+WEIGHT(I)*ARJ(I,J)*M(I)
   50 CONTINUE
   51 YMEAN=YMEAN/SUM
      DO 53 J=1,NTERMS
   53 XMEAN(J)=XMEAN(J)/SUM
      FNPTS=NPTS
      WMEAN=SUM/FNPTS
      DO 57 I=1,NPTS
   57 WEIGHT(I)=WEIGHT(I)/WMEAN
   61 DO 67 I=1,NPTS
      SIGMA=SIGMA+WEIGHT(I)*(Y(I)-YMEAN)**2
      DO 67 J=1,NTERMS
      SIGMAX(J)=SIGMAX(J)+WEIGHT(I)*(ARJ(I,J)*M(I)-XMEAN(J))**2
      R(J)=R(J)+WEIGHT(I)*(ARJ(I,J)*M(I)-XMEAN(J))*(Y(I)-YMEAN)
      DO 67 K=1,J
   67 ARRAY(J,K)=ARRAY(J,K)+WEIGHT(I)*(ARJ(I,J)*M(I)-XMEAN(J))*
     !(ARJ(I,K)*M(I)-XMEAN(K))
   71 FREE1=NPTS-1
   72 SIGMA=SQRT(SIGMA/FREE1)
      DO 78 J=1,NTERMS
   74 SIGMAX(J)=SQRT(SIGMAX(J)/FREE1)
      R(J)=R(J)/(FREE1*SIGMAX(J)*SIGMA)
      DO 78 K=1,J
      ARRAY(J,K)=ARRAY(J,K)/(FREE1*SIGMAX(J)*SIGMAX(K))
   78 ARRAY(K,J)=ARRAY(J,K)
   81 CALL MIVGJ(ARRAY,100,NTERMS)
      A0=YMEAN
```

```
  102 DO 108 J=1,NTERMS
      DO 104 K=1,NTERMS
  104 A(J)=A(J)+R(K)*ARRAY(J,K)
  105 A(J)=A(J)*SIGMA/SIGMAX(J)
  106 A0=A0-A(J)*XMEAN(J)
  107 DO 108 I=1,NPTS
  108 YFIT(I)=YFIT(I)+A(J)*ARJ(I,J)*M(I)
  111 DO 113 I=1,NPTS
      YFIT(I)=YFIT(I)+A0
  113 CHISQ=CHISQ+WEIGHT(I)*(Y(I)-YFIT(I))**2
      FREEN=NPTS-NTERMS-1
  115 CHISQR=CHISQ*WMEAN/FREEN
  121 IF(MODE)122,124,122
  122 VARNCE=1./WMEAN
      GOTO 131
  124 VARNCE=CHISQR
  131 DO 133 J=1,NTERMS
  132 SIGMAA(J)=ARRAY(J,J)*VARNCE/(FREE1*SIGMAX(J)**2)
      SIGMAA(J)=SQRT(abs(SIGMAA(J)))
  133 RMUL=RMUL+A(J)*R(J)*SIGMAX(J)/SIGMA
      FREEJ=NTERMS
  135 FTEST=(RMUL/FREEJ)/((1.-RMUL)/FREEN)
  136 RMUL=SQRT(RMUL)
  141 SIGMA0=VARNCE/FNPTS
      DO 145 J=1,NTERMS
      DO 145 K=1,NTERMS
  145 SIGMA0=SIGMA0+VARNCE*XMEAN(J)*XMEAN(K)*ARRAY(J,K)/(FREE1*
     !SIGMAX(J)*SIGMAX(K))
  146 SIGMA0=SQRT(ABS(SIGMA0))
  150 RETURN
      END



      SUBROUTINE MIVGJ(A,NP,N)
C>>>>> This routine performs a Matrix inversion by the Gauss Jordan
C>>>>> elimination method on a square matrix.
      IMPLICIT DOUBLE PRECISION (A-H,O-Z)
      DOUBLE PRECISION A(NP,NP)
      DIMENSION IPIV(1000),INDXR(1000),INDXC(1000)
      DO 11 J=1,N
   11 IPIV(J)=0
      DO 21 I=1,N
      BIG=0.0
      DO 13 J=1,N
      IF(IPIV(J).NE.1)THEN
      DO 12 K=1,N
      IF(IPIV(K).EQ.0)THEN
      IF(ABS(A(J,K)).GE.BIG)THEN
      BIG=ABS(A(J,K))
      IROW=J
      ICOL=K
```

```
      ENDIF
      ELSE IF(IPIV(K).GT.1)THEN
      STOP 'SINGULAR MATRIX'
      ENDIF
   12 CONTINUE
      ENDIF
   13 CONTINUE
      IPIV(ICOL)=IPIV(ICOL)+1
      IF(IROW.NE.ICOL)THEN
      DO 14 L=1,N
      DUM=A(IROW,L)
      A(IROW,L)=A(ICOL,L)
   14 A(ICOL,L)=DUM
      ENDIF
      INDXR(I)=IROW
      INDXC(I)=ICOL
      IF(A(ICOL,ICOL).EQ.0.0)STOP 'SINGULAR MATRIX'
      PIVINV=1.0/A(ICOL,ICOL)
      A(ICOL,ICOL)=1.0
      DO 16 L=1,N
   16 A(ICOL,L)=A(ICOL,L)*PIVINV
      DO 21 LL=1,N
      IF(LL.NE.ICOL)THEN
      DUM=A(LL,ICOL)
      A(LL,ICOL)=0.0
      DO 18 L=1,N
   18 A(LL,L)=A(LL,L)-A(ICOL,L)*DUM
      ENDIF
   21 CONTINUE
      DO 24 L=N,1,-1
      IF(INDXR(L).NE.INDXC(L))THEN
      DO 23 K=1,N
      DUM=A(K,INDXR(L))
      A(K,INDXR(L))=A(K,INDXC(L))
   23 A(K,INDXC(L))=DUM
      ENDIF
   24 CONTINUE
      RETURN
      END
```

Appendix D
Courses and Conferences Attended

In accordance with the regulations of the Department of Chemistry, University of Edinburgh I have attended the following courses during my period of study:

1. Scientific German
2. Molecular Electronics
3. Laser Physics
4. Mass Spectroscopy
5. RKR Method
6. Least Squares Methods
7. Micro Computing
8. Fortran 77
9. Theoretical Chemistry
10. Signal Processing

In addition I have attended the Laser Chemistry research group meetings, departmental seminars, joint Edinburgh - Heriot-Watt laser chemistry group meetings, and the following conferences:

1. Faraday Division, High Resolution Spectroscopy Group, Reading, 1984
2. Faraday Division, High Resolution Spectroscopy Group, York, 1985
3. Scottish Quantum Chemistry Group, Dundee, 1985
4. Scottish Quantum Chemistry Group, Strathclyde, 1986
5. XIth International Symposium on Molecular Beams, Edinburgh, 1987